Partial Chemicalization of Nanoscale Metals: An Intra-Material Transformative Approach for the Synthesis of Functional Colloidal Metal-Semiconductor Nanoheterostructures

Suman Bera, Puspanjali Sahu, Anirban Dutta, Concetta Nobile, Narayan Pradhan, and P. Davide Cozzoli**

Heterostructuring colloidal nanocrystals into multicomponent modular constructs, where domains of distinct metal and semiconductor phases are interconnected through bonding interfaces, is a consolidated approach to advanced breeds of solution-processable hybrid nanomaterials capable of expressing richly tunable and even entirely novel physical-chemical properties and functionalities. To meet the challenges posed by the wet-chemical synthesis of metal-semiconductor nanoheterostructures and to overcome some intrinsic limitations of available protocols, innovative transformative routes, based on the paradigm of partial chemicalization, have recently been devised within the framework of the standard seeded-growth scheme. These techniques involve regiospecific replacement reactions on preformed nanocrystal substrates, thus holding great synthetic potential for programmable configurational diversification. This review article illustrates achievements so far made in the elaboration of metal-semiconductor nanoheterostructures with tailored arrangements of their component modules by means of conversion pathways that leverage on spatially controlled partial chemicalization of mono- and bi-metallic seeds. The advantages and limitations of these approaches are discussed within the context of the most plausible mechanisms underlying the evolution of the nanoheterostructures in liquid media. Representative physical-chemical properties and applications of chemicalization-derived metal-semiconductor nanoheterostructures are emphasized. Finally, prospects for developments in the field are outlined.

1. Introduction

The size and shape dependence of the physical–chemical properties of condensed matter at the nanoscale offers a playground for the study and manipulation of unconventional phenomena and functionalities exploitable in a wide range of applications.[1] Of extreme relevance as models for the assessment of quantum confinement and the structural evolution of solids down to their ultimate size limit are colloidal nanocrystals (NCs), tiny crystalline particles of inorganic materials, which can be entirely synthesized and stabilized in the liquid phase, then easily transferred to different environments, processed and integrated into disparate technologies.[1a,c,2]

NCs of semiconductor materials demonstrate distinctive structural properties and distribution of electronic states that are tunable upon control of their composition (i.e., stoichiometry, dopant type, and concentration), crystal phase (in the case of polymorphic compounds) and geometry (size and shape).[1–3] Thus, semiconductor NCs can be precisely engineered to exhibit programmable optical

---

S. Bera, P. Sahu, A. Dutta, N. Pradhan
School of Materials Sciences
Indian Association for the Cultivation of Sciences (IACS)
Kolkata 700032, India
E-mail: psahu.chem@gmail.com

The ORCID identification number(s) for the author(s) of this article can be found under https://doi.org/10.1002/adma.202305985

DOI: 10.1002/adma.202305985

C. Nobile
CNR NANOTEC – Institute of Nanotechnology
UOS di Lecce
Lecce 73100, Italy

P. D. Cozzoli
Department of Mathematics and Physics “Ennio De Giorgi”
University of Salento
Lecce 73100, Italy
E-mail: davide.cozzoli@unisalento.it

P. D. Cozzoli
UdR INSTM di Lecce
c/o Università del Salento, Lecce 73100, Italy

absorption/emission capabilities, red-ox response, and electrical and magnetic behavior, which are exploitable to consolidate existing applications or develop new ones in several fields across the breadth of optoelectronics, photovoltaics, and (photo)catalysis.[2a,b,d–h,3,4] On the other side, NCs of metallic materials can be constructed not only to serve as heterogeneous platforms with enhanced and/or unusual catalytic activity (on suitable activating supports), but also to be utilized as light-manipulation tools under excitation of their localized surface plasmons (as in the case of gold-, silver- and copper-based alloys, and of heavily doped plasmonic semiconductors).[2d–g,4a,e,5]

1.1. Motivations for Growing Colloidal Metal–Semiconductor Nanoheterostructures

Unfortunately, as of today, ample expression of the ultimate technological potential of semiconductor NCs still remains depressed by severe constraints. Primarily, the use of NCs to construct the active layer of optoelectronic devices often conflicts with the difficulty of guaranteeing electrical conduction across neighboring NCs to the relevant electrodes and/or to other components.[6] Transfer of excess charge carriers in excited NCs to target molecules or other (nano)materials is typically a slow or inefficient process that may also have to compete with degradative pathways, such as photocorrosion of the NCs themselves. These drawbacks hinder the full exploitation of NCs-based photo- and electro-catalytic reactions across the interface region between the NC surface and surrounding environment for energy-conversion purposes.[7] In the case of metal NCs, close interaction with another solid material (e.g., a supporting solid substrate, an embedding matrix) is most frequently required to trigger and/or boost their catalytic activity, to modify or systematically tune their optical (e.g., plasmonic) or magnetic properties, and/or to stabilize the latter against surface oxidation or leaching, depending on the specific scopes.[5c,f,8]

A widely acknowledged paradigm shift, which has recently been devised toward alleviating (or even solving) the inherent limitations of single-material NCs and broadening their applicative horizons, leverages on the realization of heterostructured NCs, rationally designed multicomponent NC-based constructs, in which domains with distinct compositions and crystal phases are interconnected together into elaborated spatial arrangements through site-specific, chemically bonded (frequently epitaxial) heterojunctions.[6,9] Conceptually, heterostructuring embodies a general approach to advanced breeds of modular nanoarchitectures that may not only integrate the nonhomologous properties and functionalities of different nanoscale materials, but also exhibit new or unexpected behavior stemming from exchange-coupling interactions between the interfaced constituents.[4c,6,9d–f,10]

Motivated by the fundamental and practical relevance of semiconductors and metals, and by the additional opportunities offered by their associations across the whole breadth of nanoscience and nanotechnology, a rich selection of colloidal metal-semiconductor nanocrystal heterostructures (MSHs) has rapidly been developed over the past decade, standing out over traditional classes of corresponding hybrid nanomaterials (e.g., based on mere physical mixtures or structurally elusive nanocomposites). MSH prototypes illustrate the essence of the heterostructuring paradigm in many respects, exemplifying how the promise of enhanced functionality may actually be realized. For example, in a suitably configured MSH, the metal components can allow the establishment of ohmic contacts that promote shuttling of photogenerated electrons across the semiconductor/metal junctions outwards and the destination of holes to remote sites over the nanoheterostructure. Such a mechanism of charge-carrier relocation enables reducing the probability of electron-hole recombination and increasing the efficiency of photocatalytic processes.[11] Highly chemically reactive or organic-functionalized metal domains are also exploitable as anchor points by which MSHs can be driven to self-assemble over areas in devices where they are actually needed.[12] Purposely engineered MHSs, where the inherent characters of nanoscale semiconductor and metal materials are substantially preserved, may exhibit anomalous physical-chemical behavior arising from proximity or direct electronic communication effects (e.g., related to charge polarization, enhanced local electric field, misfit strain) across the bonding heterointerfaces between the relevant modules. In MHSs, heterostructuring has indeed been proven to lead to synergistic enhancement of the ultimate optical, electric, magnetic, and photocatalytic responses of either or both constituent modules, an opportunity otherwise prohibited to the isolated materials.[6,9e,10c,l,m,t,13]

1.2. Synthesis of Heterostructures: State-of-the-Art and Challenges

To date, sophisticated exemplars of multicomponent MSHs featuring an impressive level of configurational and compositional accuracy have become available. The engineering of these prototypes has required refining and expanding the synthetic capabilities of the already consolidated wet-chemical routes to single-material NCs. Ordinarily, NC syntheses involve elaborated techniques based on programmed heating of suitable precursors in a dedicated liquid mixture of coordinating agents. In such an environment, protected by a shell of dynamically surface-bound capping ligands/surfactants, NCs nucleate and grow, then steadily evolving in size and shape upon reaction and condensation of their atomic or molecular constituents (referred to as the “monomers”) provided by active species liberated into the solution.

The general approach to synthesize MSHs, utilizable for the fabrication of colloidal nanoheterostructures of any combinations of materials, relies on a sequential construction scheme, whereby dissimilar NC modules are induced to evolve, transform, and/or interconnect together in consecutive steps to eventually form an all-inorganic platform with a spatially controlled distribution of its composition and/or lattice structure.[6,9e,10a,b,d,j,n,p,r,13a,14] In the most successfully exploited procedure, commonly termed “seeded growth”, preformed NCs of one of the materials of which the targeted MSH is intended to be composed, or a partially constructed MSH, serve as primary substrates (*seeds*), onto which new domains of one or more different materials are allowed to nucleate and grow heterogeneously from the respective molecular precursors onto the accessible facets, edges and/or corners in a liquid solution

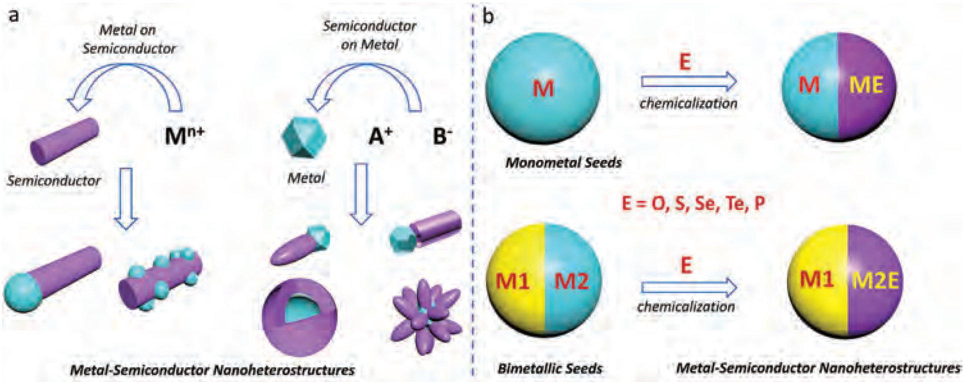

Figure 1. Conventional versus Chemicalization-based Seeded-Growth Routes to Colloidal MSHs. a) Reaction scheme of the standard seeded route to MSHs based on the mechanism of heterogeneous nucleation and growth: (left) monometallic or alloyed domains can be deposited via reduction of appropriate metal-ion (M^{n+}) precursors on the surface of preformed semiconductor seed NCs; (right) semiconductor sections can be driven to evolve out of preformed metal NCs upon reaction with single- (A-B) or distinct-source (A^+, B^-) molecular precursors. b) Schematics of a generic partial-chemicalization mechanism for the conversion of monometal (M) and bimetallic (M1-M2) alloy or heterostructured seed NCs with at least one accessible metal domain to MSHs with distinct metal and semiconductor phases (M-ME or M1-M2E): the seeds undergo replacement of a portion of their lattice to accommodate one or more domains of the desired semiconductor (ME or M2E) upon red-ox reactions with suitable reagents that provide the necessary precursor species (E).

containing suitable ligands and/or surfactants. **Figure 1** exemplifies possible reaction trajectories in the seeded-growth synthesis of MSHs. Most commonly, the crystal phase, stoichiometry, and geometry of the seeds remain unaltered during the secondary deposition process, which facilitates capturing of the details of heterostructure formation, understanding of the underlying mechanisms, and assessment of the product quality features (Figure 1a). However, depending on the synthesis conditions and the nature of the materials targeted, the seeds may also undergo changes in geometric parameters, crystal structure, and composition under specific transformative pathways (e.g., by ion exchange or red-ox replacement reactions, induced phase segregation, etching, and others), thus playing themselves additional delicate side roles in the configurational evolution of the heterostructure (Figure 1b).

A rational spatial organization of their component semiconductor and metal sections in an MHS is a prerequisite to realizing and regulating the envisaged properties and functionalities. Thus, a major goal in the synthesis of MSHs with a predesigned architecture is achieving regio-specific installation of the desired material components over the selected seed NC substrates via control over the site-dependent reactivity of the latter. Yet, the success of the seeded-growth approach to MSHs depends on many critical factors, which are challenging to accommodate all at once. First, although heterogeneous nucleation is theoretically predicted to be kinetically favored over competitive homogeneous nucleation, it remains practically difficult to totally inhibit the formation of separate mono-component NCs of the secondary material(s).[9d,e,14f,15] Nevertheless, reaction conditions can be adjusted so as to guarantee that, on a statistically significant basis, selective deposition events over the target seeds are preferred over parasitic monomer condensation pathways across the bulk solution. In this respect, judicious regulation of the solution supersaturation and of temperature to moderate levels, compared to those set in the synthesis of the individual materials, represents an obvious strategy to enhance the relative probability of triggering heterogeneous nucleation, thus maximizing the yield of MSHs over other products.

The reaction and assembly of active monomers on the surface of a foreign pre-existing substrate, which is at the basis of the formation of MHSs within the seeded-growth context, is a complex process, governed by a set of thermodynamic and kinetic parameters, including surface energy and cohesive energy, on one side, and the rates of atomic deposition and surface diffusion, on the other side.[9b–e,14f]

Seeded growth under thermodynamic equilibrium may be achieved at relatively high temperatures and under moderate fluxes of impinging monomers. Under these conditions, deposition is relatively slow, and efficient surface diffusion allows the atoms to rearrange into favorable positions that contribute to minimize the overall free surface/interface energy of the system. Under thermodynamic control, the inherent surface structural features of the semiconductor and metal components and the degree of lattice congruence intervening at the relevant heterojunctions govern the surface-tension equilibrium that dictates the "wetting" mode of the secondary material(s) at each exposed seed surface. Eventually, the configuration according to which the new domains and the original seed section are spatially distributed in the resulting MHSs, will depend on the "wetting" conditions allowed by the specific surface- and interface-energy landscapes of the concerned materials.

If the energy cost for interface formation is modest (which occurs when the two materials have matching lattice parameters and/or experience strong bonding interactions) at all exposed seed sites, and/or the specific surface energy of the seed is ubiquitously higher than that of the depositing material, then atoms of secondary component will prefer to assemble layer-by-layer all over the seed, resulting in shape-conformal coating. This deposition mode leads to the formation of MSHs with core–shell type arrangements.[9b–e,10a,c,g–i,k,p,t,14a,e,16]

On the other hand, if the complete-wetting conditions highlighted above are selectively met only at some seed facets, or if partial wetting is achieved over all surfaces due to excessive interfacial mismatch between the lattice structures of the two materials for the accessible configurations, then deposition of the secondary component will overall proceed discontinuously over the seed. In such circumstances, the resulting MSHs will adopt hetero-dimer/hetero-oligomer-like configurations, where two or more distinct domains of the secondary material are connected to the underlying seed substrate via small-area bonding heterojunctions.[9b–d,10a,c,g–i,k,p,t,14a,e,16]

Although thermodynamic arguments explain which configuration would be the most favored under close-to-equilibrium growth conditions, it is clear from the large number of documented experimental results that the preference for a given architectural pattern is decided, to a significant extent, by kinetically controlled reaction regimes.[14f,15] This occurs when surface diffusion of adatoms over the seed is inhibited by large energy barriers, and/or when deposition of incoming monomers proceeds at relatively high rates. In such cases, the probability of atom incorporation to high-surface-energy locations (such as high-index facets, edges, corners, and, in general, sites exposing many unsaturated bonds), which are thermodynamically disfavored, but more chemically reactive, increases remarkably. The presence of crystal defects (twins, stacking faults, dislocations), adds further complexity to the surface-energy landscape of the seed. Differences in heterogeneous nucleation rates at distinct locations over the seed surface can be either accentuated, leveled off, or even reversed in response to changes in reaction temperature, reactant, and ligand concentrations.[9d,14f,15] Under kinetic control, seeded growth may not be necessarily accompanied by minimization of the total surface energy of the system; therefore, heterostructures with more asymmetric configurations that significantly deviate from the thermodynamically expected ones can be formed.

A large body of evidence illustrates how the structural and geometric features of the NCs that are used as seeds indeed play critical roles in the kinetically controlled synthesis of nanoheterostructures in general, and of MSHs in particular. Under circumstances in which interfacial strain does not emerge prohibitively high, smaller seeds with almost regular polyhedral shapes may ubiquitously react faster, compared to larger or bulkier seeds, owing to their higher average chemical potential. However, NC seeds trapped in low-symmetric crystal phases and/or tailored in asymmetric morphologies are likely to expose crystallographically nonequivalent sets of facets or morphologically uneven surfaces, thus offering an anisotropic distribution of the chemical potential for their surface atoms. This fact has profound implications for the configurational manipulation ultimately achievable by seeded growth.[14f,17] Heterogeneous nucleation on such anisotropic-shaped NCs acting as seeds initiates on those facets that are less stable due to their inherent atomic arrangement and/or weaker degree of dangling-bond passivation by organic ligands/surfactants. For example, NCs of many transition-metal chalcogenides and oxides with rod-like or polypod-like shapes typically have the longitudinal sidewalls of their rod sections enclosed by relatively flat and inert facets, whereas their apexes (tips) are terminated by high surface-energy facets. The latter demonstrated to be far more chemically reactive, predisposing the seeds to accommodate selective nucleation and growth of secondary materials on the tips under appropriate conditions.[10l,18] In the case of larger seed NCs with more intricate shapes, the complex spatial variation of the surface energy offers an ample structural basis for regioselective or regiospecific deposition of additional material components, which holds synthetic potential for significant topological diversification.

Unfortunately, as the local chemical composition and structure (e.g., defects), density of coverage, and bonding strength of ligands, surfactants, or any other coordinated agents on the exposed surfaces of a NC seed are generally unknown, it remains hard to predict which sites will act as preferential for heterogeneous nucleation. In addition to seed-related factors, other experimental parameters, such as the seed, reactant, and ligand/surfactant concentrations, their ratios, the type of solvents, the presence of impurities, and temperature jointly affect the kinetics of MSH formation through microscopic mass-transport and chemical-reaction mechanisms that are difficult to disentangle and/or to manipulate individually. Finally, it should be pointed out that, in realistic circumstances, not only reactant concentration and temperature may change during the seeded-growth processes, but also the surface-energy landscapes of the seeds and of the newly installed domains may evolve significantly over time (for example, due to emergence of interfacial strain or phase instability, expression of new facets and/or formation of defects, etc.). As a consequence, the formation of NC heterostructures normally takes place at the crossover of thermodynamically and kinetically controlled regimes, whereby facile transitions between distinct, nonequivalent configurations are possible.

To summarize, the complexity of reaction trajectories underlying seeded growth still hinders a full understanding of the formation mechanisms of the diverse heterostructured nanoarchitectures, including MSHs, which are accessed. As a matter of fact, synthesis protocols developed so far are affected by modest robustness and limited reproducibility.[6,10t,14a,b] Hence, the preparation of MSHs with desired features and properties in a rational and controllable fashion remains a challenging task.

1.3. Partial Chemicalization as an Alternative Seeded-Growth Route to Nanocrystal Heterostructures

To overcome the synthetic limitations highlighted above, a set of innovative routes, based on the paradigm of the so-called partial chemicalization, has recently been elaborated as an alternative to the standard version of the seeded-growth approach to colloidal MHSs. The technique relies on performing spatially controlled replacement reactions on preformed (metal or semiconductor) NC seeds, a lattice portion of which is sacrificially converted to one or more domains of a different material (semiconductor or metal, respectively): this mechanism may lead to formation of MSHs, in which clearly distinguishable semiconductor and metal domains share bonding interfaces and/or are separated by an intervening void.[19] Depending on the composition and structure of the starting seeds, partial solid-state transformations may be conducted by manipulating galvanic, ion-exchange, and/or phase-segregation reactions, either individually or in combination, under judicious control of the seed-to-reactant ratios.

Leveraging on prior mechanistic knowledge, the chemicalization scheme can enable programmed construction of MSHs upon selection of seed NCs with crystal structure and composition suitable to undergo chemical and structural conversions that

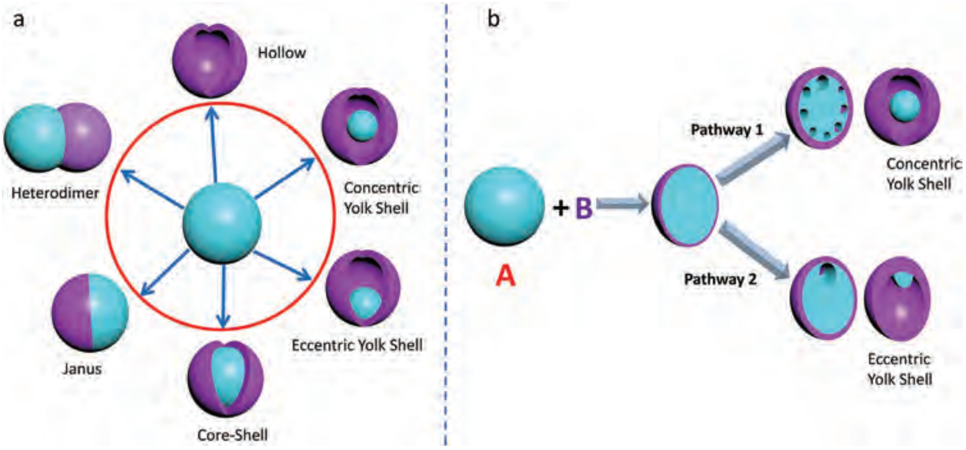

Figure 2. Possible chemicalization trajectories for the conversion of monometal NCs to MSHs. a) Overview of the diverse configurations in which MSHs may be obtained by chemicalization of monometal NCs. b) Schematic representation of the possible pathways of structural-compositional evolution that can be driven by Kirkendall diffusion processes when metal NCs (A) are reacted with an appropriate chemicalization agent (B). Hollow-solid MSHs with rich architectural diversity can be generated. If the rate of creation of vacancies is higher than their rate of migration, the process results in core-shell type MSHs (pathway 1). As opposed, if the rate of formation of vacancies is slower than their rate of migration, yolk-shell type MSHs are formed (pathway 2). Note that, for the sake of simplicity, the seeds are sketched as spherical; however, the highlighted trajectories may apply to seeds with other shapes.

would result in the desired distribution of semiconductor and metal components. Such an approach can capitalize on the broad library of colloidal metal, metal-alloy, and semiconductor NCs that can currently be synthesized with controlled parameters, and on a rich toolbox of transformation pathways based on diverse chemical triggers. Chemicalization shifts the driving mechanism for the formation of colloidal nanoheterostructures from conventional heterogeneous nucleation in a liquid solution to heterogeneous nucleation within a solid phase at the expense of the latter, realized through a combination of chemical and structural transformations that ultimately result in crystal-phase segregation of new domain(s). Thus, some of the synthetic issues associated with the classical seeded-growth scheme can be alleviated. For example, parasitic homogeneous nucleation of the secondary material is naturally avoided, since some atomic precursors remain confined within the seed of NCs. In addition, the possible occurrence of spatially disordered nucleation, which may lead to nanoheterostructures with irreproducible or undesired configurations, can largely be circumvented upon applying an appropriate site-selective chemical reaction to convert the sacrificial seeds. Finally, under the kinetically controlled growth regimes that most frequently established in colloidal syntheses, replacement mechanisms may pave the way to a broader selection of thermodynamically disfavored phases.

A chemicalization approach with great synthetic potential towards MSHs relies on the use of either monometal, bimetallic alloy, or bimetallic heterostructured NCs with at least one accessible metal component, as the starting seeds. In this case, localized atomic substitution over the seeds may be carried out by exploiting selective red-ox reactions, in association with thermally or chemically triggered (de)alloying processes. With adjusted synthesis parameters, a calibrated fraction of the original zerovalent metal atoms in the seeds may eventually be oxidized to combine with suitable precursor species to build the target semiconductor material(s) (Figure 1b). Such a strategy allows the construction of a broad spectrum of MSHs with adjustable composition and architecture, hardly achievable by the conventional seeded-growth technique or by reverse chemicalization schemes based on the partial transformation of semiconductor seeds.

This review article is focused chiefly on illustrating the conversion pathways by which metal-based seed NCs can be transformed to MSHs or other nanostructure types through chemicalization based on red-ox replacement reactions and understanding the morphological-structural changes that accompany the evolution. The underlying chemistry is discussed on the basis of current knowledge and most credited mechanistic hypotheses. In addition, some key properties and specific applications of MSHs derived from chemicalization routes are emphasized. Finally, possible prospects for developments in the field are discussed.

2. From Monometal Seeds to Metal–Semiconductor Nanoheterostructures

2.1. Structural Diversity and Solid-State Diffusion Dynamics via the Kirkendall Mechanism

Chemicalization of single-component metallic nanostructures can lead to the evolution of MHSs with various morphologies, across exotic pathways that are now understood and can thus be manipulated by adjusting several experimental parameters. Possible chemicalization trajectories for the conversion of monometal NCs to MSHs are outlined in **Figure 2**. A spherical metallic NC can be converted to a hollow nanostructure, or to MSHs with concentric or eccentric yolk-shell, core-shell, heterodimer, and Janus-type configurations, as sketched in Figure 2a. An overview of the structure-variable MSHs that have so far been obtained upon the chemicalization of monometallic NCs is provided in **Table 1**.

A pioneering report by Yin et al. showed that the reaction of easy-to-oxidize transition-metal NCs with air or elemental chalcogens can result in unique MSHs as metastable reaction

Table 1. Summary of structure-variable MSHs obtained upon chemicalization of different monometal NC seeds.

Metal used as seed	Chemicalization Agent	Structure of as-derived MSHs or modified NCs	Reference
Ni	O_2	Ni@NiO yolk-shell; hollow Ni	[21d]
Co	O_2	Co@Co_3O_4 yolk-shell; hollow Co_3O_4	[21g]
Fe	O_2	Fe@γ-Fe_2O_3 yolk-shell; hollow γ-Fe_2O_3	[22]
Cu	O_2	Cu@Cu_2O core-shell; hollow Cu_2O	[23]
Ni	O_2	asymmetric Ni@NiO yolk-shell; hollow NiO	[24]
Sn	O_2	Sn@SnO_2 yolk-shell	[25]
Sn	O_2	Sn@SnO_2 core-shell	[26]
Si, Ge	O_2	hollow SiO_2 and GeO_2	[27]
Cu, Al, Pb	O_2	hollow Cu_2O and Al_2O_3; all-solid PbO	[28]
Bi	O_2	Bi@Bi_2O_3 yolk-shell; hollow Bi_2O_3	[29]
Ag	O_2	Ag@Ag_2O yolk-shell	[30]
Ni	O_2	NiO nanotubes with inner Ni segments	[31]
Cu	O_2	Cu_2O nanotubes with Cu segments	[32]
Co	O_2	Co@CoO core-shell; hollow CoO	[33]
Zn	O_2	hollow ZnO	[34]
Fe	O_2	Fe@Fe_xO_y core-shell; Fe@Fe_xO_y yolk-shell	[35]
Ni	O_2	all-solid NiO; symmetric and asymmetric hollow NiO	[36]
Co	O_2	Co@CoO yolk-shell; all-solid and hollow CoO	[37]
Co (single-crystalline) Co (polycrystalline)	O_2	hollow CoO; Co@CoO core-shell	[38]
Ag	O_2	Ag@Ag_2O yolk-shell	[39]
Cu	O_2	hollow Cu_2O	[40]
Co	Molecular S	hollow Co_3S_4 and Co_9S_8	[20]
Co	Molecular S	hollow Co_3S_4 and Co_9S_8	[21a]
Cd	Molecular S	asymmetric Cd@CdS yolk-shell	[41]
Cd	Molecular S	hollow CdS; all-solid CdS	[42]
Cd	Molecular S or TOP-S complex	Cd@CdS yolk-shell; hollow CdS	[43]
Ag (prism-shaped)	Na_2S	Ag@Ag_2S core-shell with flower-like shape	[44]
Ag (prism-shaped)	Na_2S and S powder	Ag@Ag_2S nanoprisms (with Ag_2S at the corners)	[45]
Cu	S in dodecanethiol	Cu-Cu_2S heterodimer	[46]
Co	Se in o-dichlrobenzene	hollow CoSe	[20]
Co	Se in dichlorobenzene	hollow $CoSe_2$	[47]
Ag	Se suspension	hollow Ag_2Se (from single-crystalline Ag); all-solid Ag_2Se (from polycrystalline Ag)	[48]
Pd	Se powder in hexadecylamine and trioctylphenyloxide	Pd-$Pd_{17}Se_{15}$ Janus-type	[49]
Cd	TOP-Se complex	hollow CdSe	[43]
Cd	TOP-Te complex	hollow CdTe	[43]
Cu	TOP	all-solid Cu_3P; Cu-Cu_3P Janus-type	[50]

intermediates, which can eventually evolve into hollow nanostructures as the final product.[20] NCs of cobalt sulfides (Co_9S_8 and Co_3S_4) with a clearly defined hollow interior were rapidly formed after injection of elemental S dissolved in hot 1,2-dichlorobenzene (DCB) into a hot solution of Co NCs. The reaction between the Co NCs and a suspension of fine Se powder in DCB also yielded hollow cobalt selenide NCs. However, the selenization reaction was slow enough to permit the withdrawal of NCs from the crude reaction bath and their examination at various stages of the hollowing process. During the transformation, the Co seeds were first covered with a Co_xSe_y shell. As the reaction proceeded, voids were observed to form at the Co side proximal to the Co/Se interface. Over time, the voids increased in volume and coalesced, ultimately leaving Co "bridges" behind that interconnected an inner continuous Co core and the Co_xSe_y shell. The authors argued that the difference in the diffusion rate of Co and Se across the lattice promoted the evolution of such bridging structures, according to a mechanism analogous to the so-called "Kirkendall effect", well known in metallurgy (vide infra).[19a,20] After the formation of a thin shell of Se over Co, the Co atoms tend to diffuse outward through the Co_xSe_y shell until they reach the outer surface of the nanoparticle. Simultaneously, the Se atoms diffuse inward through the shell until they reach the Co core. Due to the faster outward diffusion flux of Co atoms, compared to the slower inward flux of Se atoms, vacancies are created and injected at the Co (core)/Co_xSe_y (shell) interface. The migration and agglomeration of vacancies result in the initial formation of voids at the interface and their subsequent merging and expansion deeper across the Co core. These dynamics lead to yolk-shell and bridged-type MSHs. In general, the hollowing phenomenon within a solid host arises from differences in the diffusivity of distinct atomic elements. Before Kirkendall's studies, atomic diffusion in metals and alloys was believed to take place at an equal rate for all metal species, i.e., the diffusion coefficients of different metal atoms were assumed to be identical. In 1942, Kirkendall for the first time revealed differences in atomic diffusion rates in two-component AB alloys.[19a,20] Upon heating two stacked metals, A and B, at a temperature high enough to activate the diffusion of atoms, atomic migration occurs at the interface from metal A to metal B and vice versa, which leads to the formation of an A/B alloy layer located between the opposite sides of the interface. The position of the initial interface can change during the annealing process since the atomic diffusion coefficients of atom A in metal B and of atom B in metal A are different ($D_A \neq D_B$). If the diffusion of A through B is faster than the diffusion of B through A, then the flux of atoms migrating from A to B will be much higher than the opposite process of migration of B through A. As a consequence, the A/B alloying region will be more extended into metal B and vacancies will be created on the A side. The coalescence of vacancies results in the formation of small voids distributed all along the A-AB interface. With time, more vacancies are generated, allowing the enlargement of voids.

Only almost five decades after Kirkendall's studies, migration of atoms with different rates, analogous to that identified in bulk metals, was recognized to occur also in nanostructured solids. Interestingly, the Kirkendall process exhibits unique features when it operates in NCs. Unlike the cases of bulk alloys, where the Kirkendall mechanism is associated with the diffusion of metal species only, on the nanoscale it can involve the diffusion of both metal and non-metal elements. This explains why, soon after the first demonstration in colloidal NCs,[20] the nanoscale Kirkendall mechanism has been systematically exploited to develop general synthetic procedures to prepare hollow NCs of a variety of materials.[19,21]

Progress made so far in the understanding of the influence of the Kirkendall effect on nanostructure evolution has shown that, in most cases, treatment of metal NCs (A) with suitable chemicalization agent (B) may lead to either hollow NCs or yolk-shell type constructs, as sketched in Figure 2b. The structural conversion is initiated by the formation of a very thin shell of a reactive material of mixed composition (AB) over the seed. Once the interface is formed, atoms of A and B simultaneously start to diffuse outward and inward, respectively, yet at different migration rates. This mechanism lays a basis for achieving unprecedented nanoheterostructures with adjustable structural diversity. If the outward diffusion flux of A is much faster compared to the inward flux of B, vacancies are generated at the A(core)/AB(shell) interface. The coalescence of vacancies results in the formation of voids that are initially located at the interface region (Figure 2b). The voids serve as the sinks for the subsequent inward flux of vacancies and thus grow in volume. Over time, the voids coalesce into larger ones, leading to the formation of metallic bridges between the A core and the mixed AB shell sections that are separated by larger alternating voids intervening in between (Figure 2b). The bridges allow decreased diffusion flux of A atoms through the bulk lattice, but simultaneously they provide fast transport paths for the remaining A material along the surfaces of the connecting sections. Indeed, surface mass transport of A atoms through bridges is a much faster process owing to its lower activation energy and the higher diffusion coefficient, compared to intra-bulk diffusion. As a consequence, the A material can quickly redistribute itself at the open surface of the AB layer. However, within the AB shell, the atomic exchange keeps on proceeding via the same mechanism, i.e., via intra-bulk diffusion. Therefore, vacancies are continuously generated and flow inward. On completion, the diffusion process leaves cavities. In the final hollow NCs and in the yolk-shell type nanoheterostructure (Figure 2b), the void and the metal core are placed centrosymmetrically (relative to the shell section). Intriguingly, a partial diffusion process leads to the formation of yolk-shell-type architectures with an inner floating yolk domain.

Systematic synthetic elaboration on the Kirkendall-based mechanism has clearly illustrated that a wide variety of MSH configurations can be accessed upon the chemicalization of monometal NC seeds. These outcomes are summarized in **Figure 3**. Recent reports have documented the formation of yolk-shell type heterostructures, in which the partially dissolved metal core seed is located eccentrically at one side of the inner core part. Cabot et al. have shown that during the sulfidation of Cd NCs with elemental S in 1,2-dichlorobenzene, the hollowing process occurred through the formation of Cd-CdS intermediates (Figure 3a,b).[41] In the intermediates, the unreacted Cd core and the voids were found to be located in different caps enclosed by the CdS shell. In another work, Cabot et al. used a tri-*n*-octylphosphine telluride (TOP-Te) complex to perform partial conversion of Cd@CdSe core-shell NC seeds to hollow CdSe nanostructures, not otherwise accessible using the less reactive tri-*n*-octylphosphine selenide (TOP-Se) complex (Figure 3c,d).[42] From this outcome, they deduced that the self-diffusion of Cd from the core through the CdSe shell was not the limiting factor during the growth of the CdSe shell on Cd seeds that were combined with TOP-Se. Similar types of products were also observed for the Ni-NiO system by Nakamura et al. These authors reported the formation of Ni-NiO yolk-shell MHSs, in which a large void was placed at one side of the interface between the inner Ni and outer NiO layer.[24] A more systematic study by Railsback et al. was performed on the Ni-NiO system that followed an analogous reaction pattern (Figure 3e).[21d] The investigations clarified that, after the formation of a thin shell of NiO over the starting Ni NCs, nucleation of voids initiated at one side of the Ni-NiO interface. As the oxidation of the Ni core progressed, the deposition of NiO took place at the side opposite to the location of the void. After completion of the oxidation, the NiO shell was found to be the thinnest on the side where the void had developed and the thickest on the side opposite to the region with the void (Figure 3e,f).

Thermodynamically, the formation of a single void would be preferred over a collection of multiple voids as the surface energy of one large void would be far lower than the sum of the surface energies of multiple small voids. So, once vacancies have been created, they can migrate and merge to form a single void instead

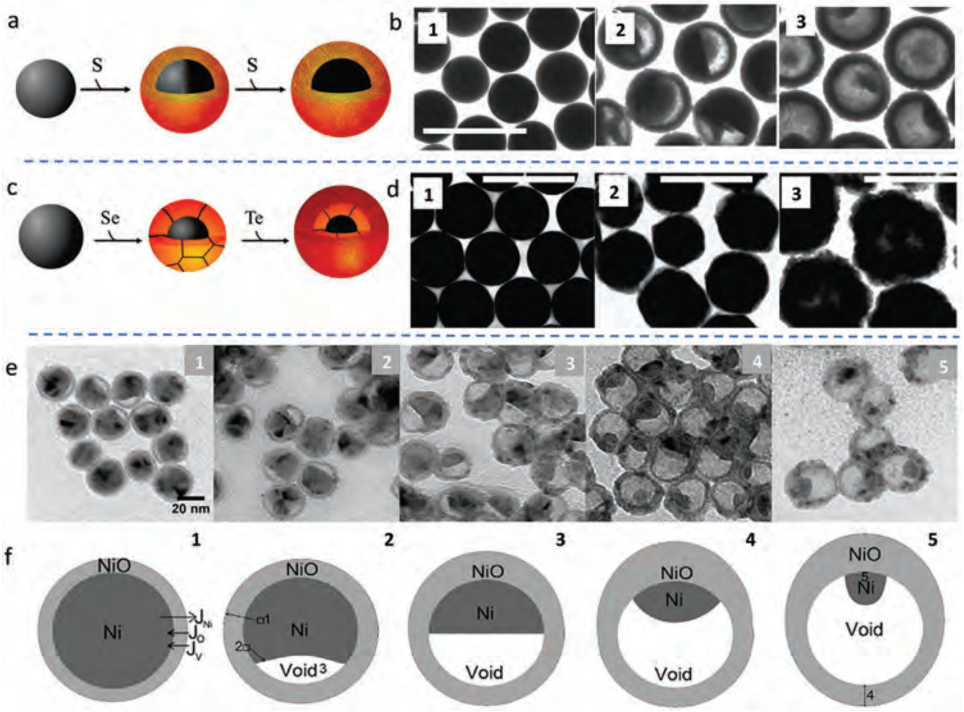

Figure 3. Examples of MSHs derived upon chemicalization of monometal seeds. a) Reaction scheme and b) TEM images demonstrating the hollowing process of Cd seeds upon sulfurization. The scale bar corresponds to 500 nm. Reproduced with permission.[41] Copyright 2008, American Chemical Society. c) Reaction scheme and d) TEM images of: 1) the initial Cd nanoparticle seeds; 2) Cd@CdSe core-shell MSHs derived from the former; 3) final nanostructures after reaction with TOP-Te complex. Reproduced with permission.[42] Copyright 2009, American Chemical Society. e) TEM images of Ni NCs subjected to oxidation in air at 300°C for 90, 120, 150, 180, and 210 min, respectively. The images demonstrate the development of a NiO shell along with asymmetric hollowing of the Ni core (the sequence corresponds to the progression from stage 1 to stage 5, as highlighted in panel f). f) Sketch of the hollowing process of Ni NCs during their oxidation in air. Reproduced with permission.[21d] Copyright 2010, American Chemical Society.

of multiple voids, as previously recalled for the case of symmetric nanostructures (Figure 2b). Whether a metal seed may accommodate a symmetric or asymmetrically distributed void space will depend on the dynamics of void formation. If the formation rate of the vacancies is higher than their rate of migration, the small voids formed initially will not have sufficient time to diffuse before coalescing with other vacancies (Figure 2b, pathway 1). This evolution has been detected for most metal systems, including the case studies of selenization of Co NCs and oxidation of Cd NCs, illustrated earlier. However, if the migration rate of vacancies is faster than their generation, they move to one side of the interface where they can coalesce to form more energetically favorable larger holes (Figure 2b, pathway 2). This occurrence has actually been verified for the Ni/NiO and Cd/CdS systems (note that, in the latter case, the Cd diffusivity through the shell is approximately 4 orders of magnitude slower than the self-diffusivity of Cd).

Further, Cho et al. have exploited the Kirkendall diffusion process to obtain hollow SnO_2 nanospheres in kilogram-scale amounts.[25] High-temperature oxidation of Sn NCs embedded in carbon matrix led to the formation of hollow SnO_2 NCs. The hollowing process was regarded to take place as a consequence of the outward diffusion of Sn cations being faster than the inward diffusion of oxygen ions. Under different circumstances, Sn NCs obtained by injection of $LiN(SiMe_3)_2$ into a hot oleylamine solution containing $SnCl_2$ or $Sn[N(SiMe_3)_2]_2$, followed by reduction with diisobutylaluminium hydride (DIBAH), converted to Sn@SnO_2 core/amorphous-shell NCs upon exposure to air.[26] No hollowing was observed in the latter case.

Gao et al. reported a hollowing experiment, where nanowires of magnetically connected Co NCs underwent selenization, resulting in the formation of corresponding nanowires made of hollow CoSe nanoparticles.[47] Peng et al. showed that the formation of hollow Fe_3O_4 NCs from amorphous Fe nanoparticles proceeded via the formation of Fe@Fe_3O_4 yolk-shell-type MSHs, i.e., NC intermediates with a core(Fe)/void-shell/shell(Fe_3O_4) configuration.[51] In a similar work, Cabot et al. illustrated the time- and temperature-dependent vacancy coalescence that produces Fe@γ-Fe_2O_3 yolk-shell-type MSH intermediates during the evolution of hollow γ-Fe_2O_3 NCs upon controlled oxidation of Fe nanoparticles.[22] A systematic investigation by Son et al. provided a deeper insight into the nanoscale Kirkendall effect.[27] Si nanowires (NWs) were transformed into hollow Si nanotubes (NTs) via the formation of surface SiO_2 layers. Si atoms diffused via SiO_2 leading to the formation of oxygen-deficient SiO_x ($0 < x < 2$). The mechanism of the Kirkendall effect was studied via quantum molecular dynamics simulations and transmission electron microscopy (TEM) analyses. Annealing promoted the outward diffusion of both Si and O atoms. However, the much slower diffusion of Si atoms compared to O atoms led to the formation of inner pores at the interface. Although O and Si

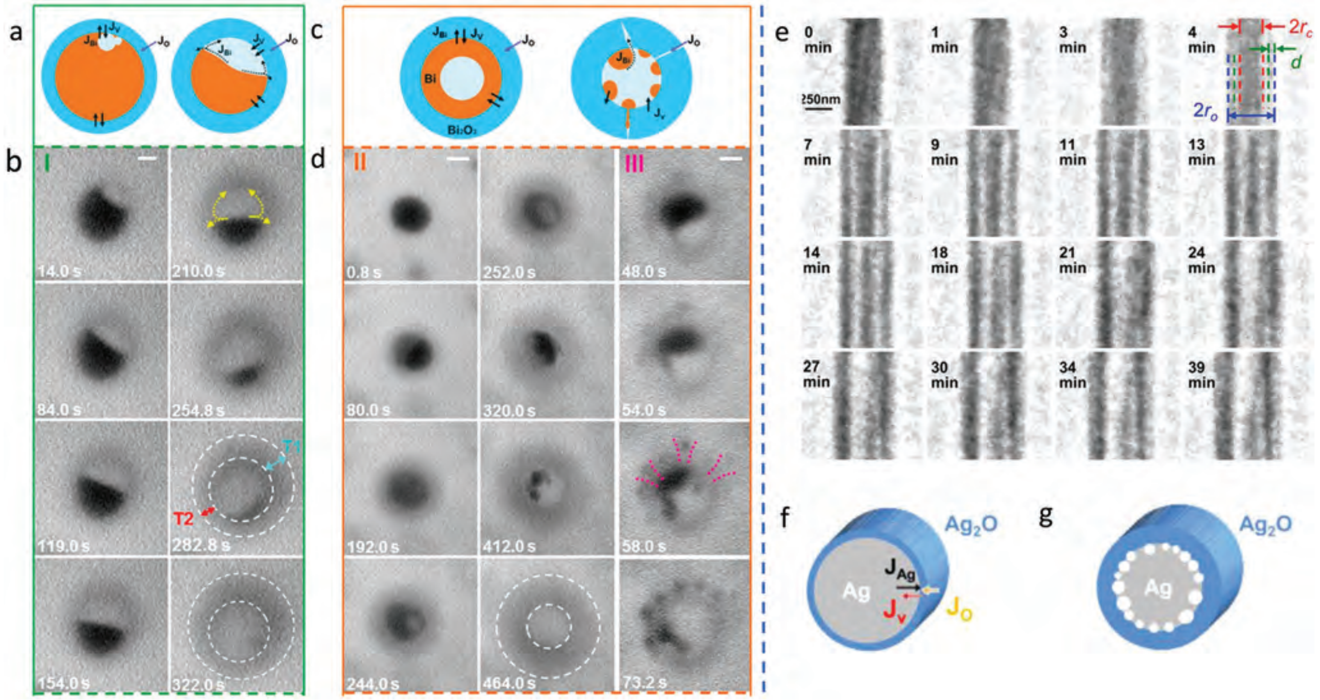

Figure 4. Case studies on the mechanisms of formation of MSHs upon chemicalization of monometal seeds. a) A schematic of the oxidation process of solid Bi NCs, dominated by non-uniform diffusion of Bi species through void surfaces. b) TEM image series demonstrating the formation of hollow NCs (scale bar is 20 nm). c) Schematic of the oxidation of Bi NCs, dominated by diffusion of Bi species through the shell. d) TEM images of the evolution of different-type hollow Bi NCs (stage II and stage III) (scale bars are 50 nm). Reproduced with permission.[29] Copyright 2013, American Chemical Society. e) TXM images demonstrating the oxidation process of Ag nanowires and f,g) illustration of the hollowing process via the Kirkendall effect, where the black, orange, and red arrows represent the diffusion flux of silver, oxygen, and vacancies, respectively. Reproduced with permission.[30] Copyright 2016, American Chemical Society.

inter-diffused, Si was found to be substantially more abundant in the oxide layer due to the slower diffusivity of O, associated with the higher formation energy of the oxide shell. All elements were eventually displaced outward, thus accounting for the formation of hollow nanostructures.

The rate at which the hollowing process develops and the extent to which it may progress are strictly dependent on the specific reaction conditions set in the synthesis. Proper control over the reaction parameters can, in fact, prevent the hollowing process from taking place completely, leading to core-shell-type structures without voids. The susceptibility of given NC seeds towards accommodating Kirkendall diffusion is governed by the size of the seeds, the reaction temperature, and the relative diffusivities of the relevant atomic species. As an example, oxidation of relatively large-size Al (>8 nm) and Zn (>20 nm) NCs at mild temperatures was reported to result in core-shell MSHs with a continuous lattice.[28] On the other side, when the diffusion rate of the incoming reactive species (i.e., oxidizing agents) into the metal core exceeds the diffusion rate of metal ions into the shell material, only all-solid NCs made of the oxidized material with no cavities can be expected to eventually form. This was demonstrated, for example, by the outcome of prolonged exposure of spherical Cd and Pb NCs to O_2.[43] In such a case, all-solid PbO and CdO NCs were obtained as a consequence of the diffusion of oxygen into Cd and Pb cores being faster than the diffusion of Cd and Pb into the CdO and PbO shells, respectively. Monodisperse Fe@γ-Fe_2O_3 yolk-shell nanostructures and hollow γ-Fe_2O_3 NCs with controlled particle size and shell thickness have been engineered by Cabot et al.[22] Finally, in some cases, the oxidizing species were found to be unable to react at the NC seed surface in a spatially uniform way, rather they preferred to attack predominantly or exclusively a particular facet of the starting seed, leading to highly directional chemicalization of the lattice. No Kirkendall effect was observed in such circumstances, and asymmetric Janus-type heterostructures were eventually formed instead.[9b,c,49,50]

2.2. In Situ Investigations on the Effect of the Kirkendall Process on the Structural Evolution of the Nanoheterostructures

Recent advances in TEM-based investigative techniques have allowed deeper insights into the chemical transformation mechanism by direct in situ imaging. The results of relevant case studies are illustrated in **Figure 4**. Niu et al. have demonstrated different pathways for the oxidation process of Bi NCs with the help of TEM (Figure 4a-d).[29] They observed that the oxidation process initiated the formation of a thin layer of bismuth oxide on the outer surface of the Bi NCs. In some cases, the oxidation process was followed by the formation of an off-centered, single void at the Bi/BiO interface. Over time the metallic Bi core disappeared layer-by-layer, leading to a non-uniform oxide shell with a larger thickness close to a void (Figure 4a,b). This was an indication that diffusion of Bi into the oxide shell had occurred in a spatially non-uniform way, with faster diffusion taking place through the shell adjacent to the void.

A different behavior was observed for Bi NCs during the same oxidation process. In some seeds (Figure 4c,d), after the formation of the oxide shell on the surface, subtle diffraction-contrast changes in the relevant TEM images across the bismuth core indicated outward diffusion of Bi core upon oxidization. The contrast changes became pronounced with time, indicating the condensation of randomly distributed smaller voids into larger ones inside the core. As the Bi core deteriorated, the small amount of Bi left was increasingly destabilized and exhibited a liquid-like behavior, rapidly splitting into several nanodroplets and then disappearing. The frequent change in the Bi configuration observed during oxidation was attributed to the elevated local temperature, which was expected to be higher than the melting point of the residual Bi core. The melting temperature of metal NCs is known to decrease with size at the nanoscale (for example, Bi NCs melt at 180 °C, whereas bulk Bi melts at 271 °C). Thus, the conversion process resulted in a uniform shell thickness (Figure 4d, panel II). The authors further observed the formation of clusters on the outer surface of the starting Bi seeds (Figure 4d, panel III). It was presumed that the defects in the shell, such as grain boundaries, served as diffusion paths, facilitating the outward migration of the Bi species and their condensation into clusters before being oxidized. Due to the existence of the various diffusion channels, the rate of shell growth could be enhanced. It should also be noted that the diffusivity of Bi through the bismuth oxide shell in the NCs is $\approx 3-4$ times higher than its diffusivity in the bulk material. Overall, this study illustrated that there could be multiple paths for atomic diffusion within the context of the Kirkendall process, such as surface-mediated diffusion, uniform diffusion through the shell, and others.

Albinsson et al. have investigated the oxidation behavior of 30 nm Cu NCs with the aid of in situ plasmonic spectroscopy and finite-difference time-domain (FDTD) simulation.[52] Their study revealed that, in the initial phase of oxidation, hindered by a low activation energy, small grains within disordered structure were formed at the interface of metal-oxide layer. The size of the grains near the metal–oxide interface increased as oxidation progressed; as a result, the effective activation energy for diffusion jumps increased because low energy diffusion sites at grain boundaries had become less abundant. This fact could also help to understand the pathways of partial oxidation in NC systems that may evolve to MSHs.

Yu et al. have studied the oxidation process of Ag nanowires using transmission X-ray microscopy (TXM) (Figure 4e–g).[30] During the initial stage of the reaction, a thin oxidation layer was formed on the surface following the adsorption of atomic oxygen on the surface. Later, a bright void could be seen. At the interface between the oxide layer and the Ag core, vacancies were created as a result of the slower inward diffusion of O compared to the outward diffusion of Ag. These vacancies accumulated, reached supersaturation, and then produced Kirkendall-driven voids at the junction (Figure 4f,g). The core shrunk and oxide shell enlarged as the diffusion and oxidation continued. After longer times, the inner core started to shift toward the right side, indicating that the core had lost its mechanical support by the linkages to the shell. Eventually, the Kirkendall-derived voids expanded by further vacancy flux at the core-shell interface, introducing a volume space that completely separated the core and the shell regions.

Though there are many reports evidencing the relevance of Kirkendall effect in the formation of MSHs, more investigations are needed to understand what thermodynamic factors and/or kinetic pathways could be dominant under specified conditions. This knowledge could aid designing nanoarchitectures with the desired degree of (a)symmetry.

2.3. Factors Affecting the Kirkendall Process and the Subsequent Architectural Evolution of the Nanoheterostructures

Several factors, including chemical–physical parameters, structural features, and reactivity patterns of the involved reactants, can affect the atomic diffusion process, hence the Kirkendall process, at the nanoscale. Their individual effects and interplay can eventually lead to MSHs with different architectures.

2.3.1. Effect of Temperature

Temperature can significantly influence the Kirkendall diffusion by affecting the diffusion rate, activation energy, and stability of the voids. Several studies have been devoted to understand the role of temperature in the Kirkendall reaction, as illustrated by the representative case studies reported in **Figure 5**. In most syntheses carried out at relatively lower temperatures, chemicalization was observed to stop after the formation of the initial thin shell on the seeds, while the Kirkendall mechanism appeared to be operative at higher temperatures. For example, Yoon et al. performed oxidation of elemental Fe nanoparticles at room temperature. The authors documented that the oxidation arrested at core–shell level of transformation (no hollow structure was formed) even if exposure of Fe to the oxidizing agent was prolonged exceedingly (up to 5 months).[21b] Such an outcome of low-temperature oxidation was rationalized with the help of the Cabrera–Mott theory,[53] developed to explain the diffusion of metal ions and oxygen during the oxidation of bulk materials.[19b] According to this theory, when an oxygen molecule gets dissociated, and adsorbed onto the surface of the NCs, surface energy states are created below the Fermi level of the metal, facilitating electron transfer from the metal to the oxide. This produces an electric field within the oxide layer, which lowers the activation energy required for diffusion of metal ions through the oxide, thus accelerating their migration there across. Yet, the diffusion of metal ions, promoted by the electric field, becomes depressed as the thickness of oxide layer increases because the electric field intensity scales inversely with the thickness of oxide shell. Thus, once the oxide shell has approached a limiting thickness, further oxidation remains inhibited, unless sufficient thermal energy is supplied upon heating. Thus, lower temperatures favour the formation of core-shell architecture without inner voids.

Void formation or the Kirkendall effect were observed in reactions conducted at higher temperature.[19b] While $Bi@Bi_2O_3$ core-shell type MSHs were formed during oxidation of Bi NCs at low temperature (20 °C; Figure 5a), hollow Bi_2O_3 nanostructures were obtained at much higher temperatures (192 °C; Figure 5b).[29] A similar evolution was also observed during oxidation of Ni nanowires (Figure 5c).[31] Heating of Ni

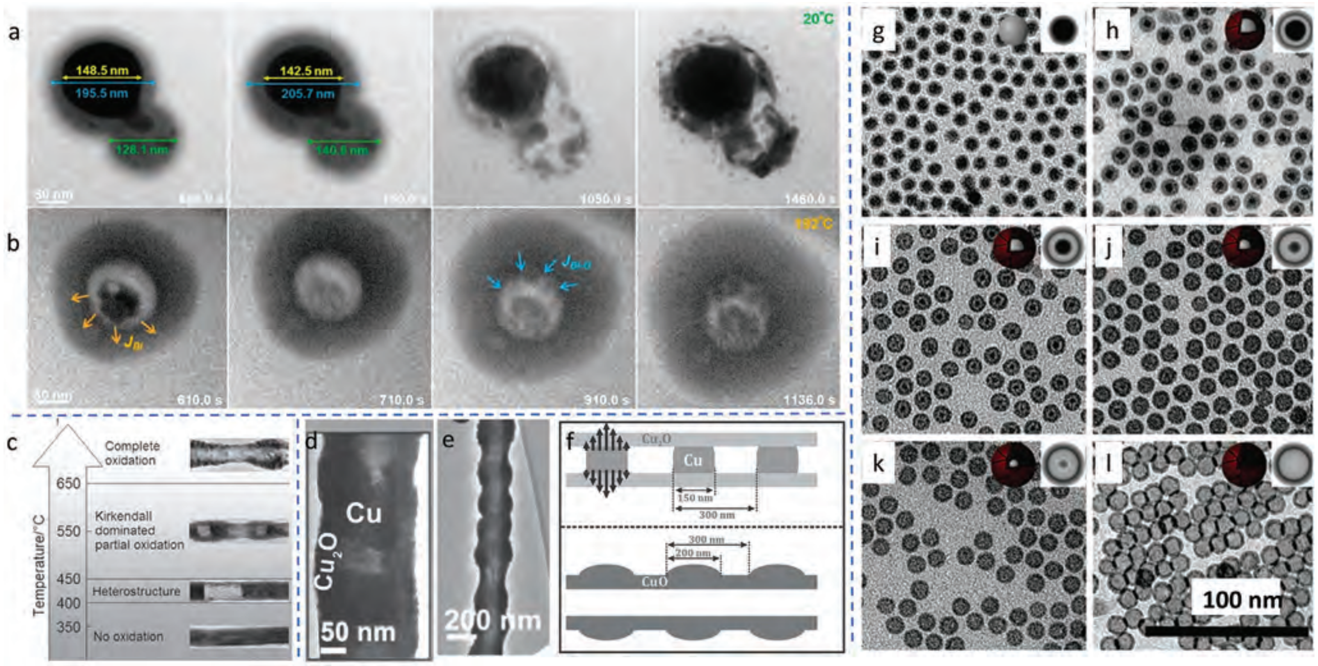

Figure 5. Case studies on the effect of reaction temperature on the formation of MSHs upon chemicalization of mono-metal seeds. a) Example of Kirkendall effect taking place in Bi NCs and leading to formation of Bi/Bi_2O_3 MSHs at 20 °C. b) A Bi_2O_3 hollow NC formed at 192°C and its collapse by inward mass diffusion. Reproduced with permission.[29] Copyright 2013, American Chemical Society. c) Schematic of different heterostructure products and TEM images of Ni nanowires oxidized at different temperatures. Reproduced with permission.[31] Copyright 2010, American Chemical Society. d) HRTEM image of a CuO nanotube having periodically arranged Cu nanoparticles. e) HRTEM images of Cu_2O-Cu MSHs and bamboo-like CuO nanostructures. f) Representation of a Cu_2O nanotube containing a periodic distribution of Cu domains (top) and of a bamboo-like CuO nanotube (bottom); the black arrows indicate the direction and the magnitude of copper atom diffusion occurring during the thermal oxidation process. Reproduced with permission.[32] Copyright 2016, Wiley-VCH. TEM images of Fe@γ-Fe_2O_3 MSHs obtained on oxidation of amorphous Fe nanoparticles with dry 20% oxygen for different periods: g) <1 min at 25°C; h) 1 h at 80°C; i) 12 h at 80°C; j) 5 min at 150°C; k) 1 h at 150°C; l) 1 h at 350°C. The simulated evolution of the nanoparticle size, core diameter, and shell thickness are presented as insets along with two-dimensional projections of the cross sections for electron scattering in core-shell, yolk-shell, and hollow nano(hetero)structures. Reproduced with permission.[22] Copyright 2007, American Chemical Society.

nanowires at lower temperature (<300 °C) could not initiate any oxidation. This fact indicated that a minimum reaction temperature was required to trigger the chemicalization process. Oxidation could indeed be induced within the temperature range of 400–450 °C. When the temperature was further increased to 550 °C, a Kirkendall-dominated partial oxidation of the Ni nanowire occurred, as demonstrated by the void formation in the Ni nanowires. Further increase in temperature to 650 °C led to the complete oxidation of Ni nanowires to NiO.

El Mei et al. have shown that the oxidation-induced nanoscale Kirkendall effect can be exploited to create copper-oxide-based nanotubes with unique morphologies and elemental distribution by applying a calibrated annealing treatment to preformed Cu nanowire precursors.[32] Cu@Cu_2O MSHs, composed of a nanotube section embedding a periodic arrangement of Cu domains within its interior, were obtained by a rapid thermal oxidation process (sample was loaded into a preheated oven), while hollow CuO nanostructures with a bamboo-like shape profile were obtained when temperature was ramped up slowly (Figure 5d,e). Unlike in Ni, in Cu the rate of injection of vacancies is higher than their diffusion. When Cu nanowires were placed in a preheated oven, rapid diffusion of Cu ions in the oxide lattice occurred leading to the formation of uniform Cu_2O shell encasing Cu domains. On the other hand, during a slow heating process, diffusion of Cu atoms was initially slow, then it increased with time. After gaps were formed between adjacent Cu domains, Cu atoms were prohibited from diffusing axially, so they started to diffuse radially through the initially formed oxide shell, leading to CuO bamboo-like tubular nanostructures (Figure 5f). This study reveals that not only the temperature selected for the desired chemicalization reaction, but also the rate at which the target temperature is reached, have an impact on the architecture of the resulting conversion nano(hetero) structure products.

In another account, Cabot et al. have further clarified that reaction temperature cannot be increased arbitrarily in order to accelerate the desired chemicalization process. The authors showed that by changing temperature over the 80–250 °C range, hollow γ-Fe_2O_3 NCs and Fe/γ-Fe_2O_3 yolk-shell MSHs with adjustable void thickness could be reproducibly achieved (Figure 5g–l).[22] However, if the temperature was increased beyond the limit of 250 °C, cracks were detrimentally introduced into the γ-Fe_2O_3 shells.

Summing up the results of all the experiments reported so far, the following conclusions can be drawn: i) a critical temperature is needed to trigger the chemicalization process; ii) at relatively lower temperatures chemicalization occurs by field-driven

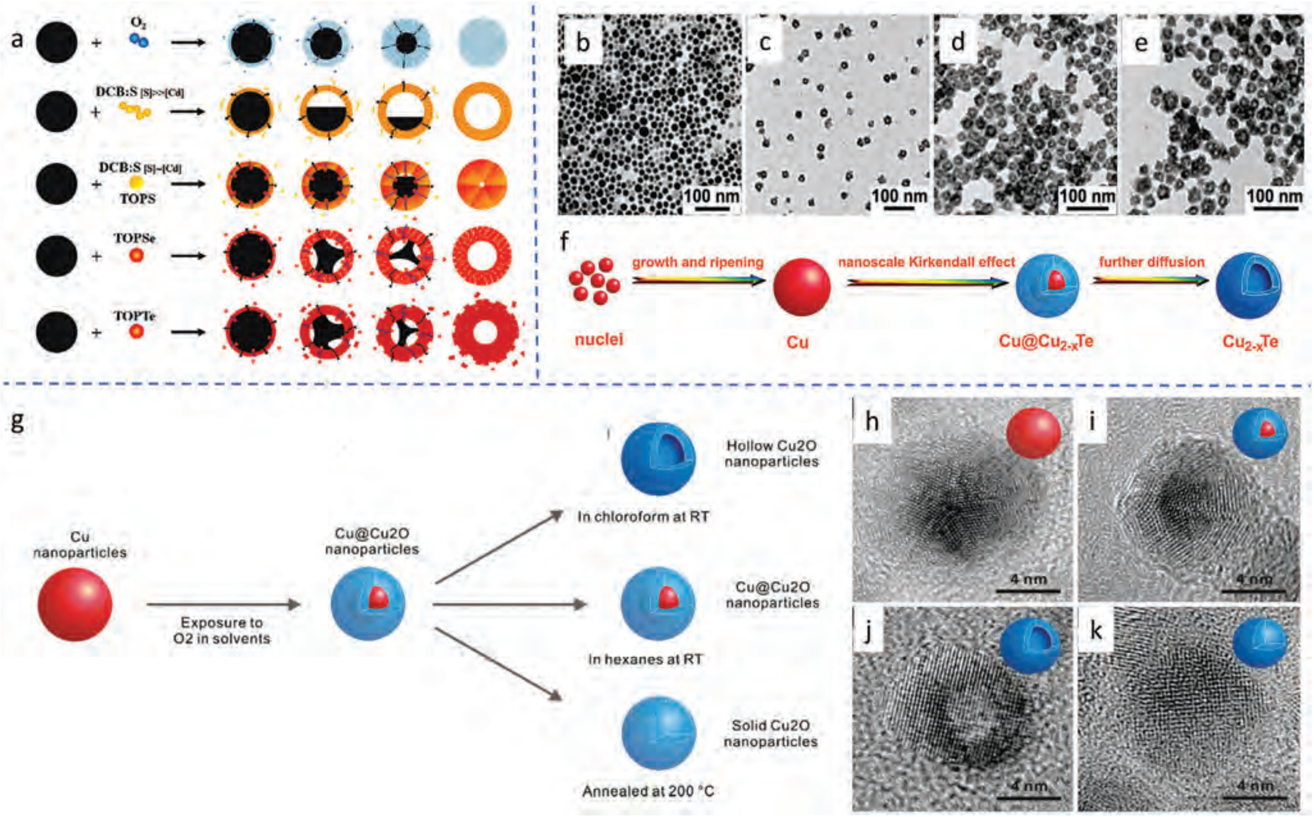

Figure 6. Case studies on the roles of chemicalization agents and capping ligands in the formation of MSHs upon chemicalization of monometal seeds. a) Schematics of the MSHs that can be obtained after the reaction of Cd NCs with O_2, elemental S in a solution, and TOP-S, TOP-Se, and TOP-Te complexes, respectively. Reproduced with permission.[43] Copyright 2011, American Chemical Society. b-e) TEM images of the Cu NCs generated upon reduction of a copper salt at 250°C, and of the as-derived products formed 10 s, 10 min, and 60 min, respectively, after the injection of TOP-Te complex in the starting mixture, along with (f) schematic illustration of the transformation of the Cu seeds to hollow $Cu_{2-x}Te$ NCs through formation of $Cu@Cu_{2-x}Te$ core-shell MSH intermediates. Reproduced with permission.[54] Copyright 2013, Wiley-VCH. g) Schematic of the oxidation process of Cu NCs leading to the formation of different types of nano(hetero)structures, shown in corresponding HRTEM images of individual objects: h) Cu NC; i) $Cu@Cu_2O$ core-shell MHS; j) hollow Cu_2O; k) solid Cu_2O NC. Reproduced with permission.[23] Copyright 2010, Wiley-VCH.

pathways leading to the formation of core-shell structures; iii) Kirkendall diffusion requires comparatively higher temperature to be activated.

2.3.2. Reactivity of Chemicalization Agents

Besides temperature, the reactivity of the chemicalization agents selected for specific synthetic purposes has a significant influence on the architecture of the final (hetero)structure product. This is because the susceptibility of the seeds towards oxidation/reduction and atomic diffusion rates across their lattice are strongly dependent on the nature of the chemicalization agent and its concentration, relative to that of the target seeds (for example, elemental S is more aggressive than dodecanthiol towards metal NCs). The results of representative case studies are illustrated in **Figure 6**a–f.

Most experiments have shown that hollow NCs are achievable at relatively high concentrations of chemicalization agent,[43] while low concentrations favor the formation of core-shell or yolk-shell MHSs.[19a,55] For example, Cabot et al. reported a striking dependence of the S-driven sulfidation of Cd NCs on the concentration of the S reagent only in the low-concentration regime.[41] At higher S concentrations, the shell growth rate was found to be independent of the amount of S added. Indeed, the authors proved that the low probability of an effective reaction of S with Cd dictates the rate of sulfidation of the Cd seeds when the molar concentration ratio is $[S]/[Cd] < 6$. Conversely, at $[S]/[Cd] > 6$, the higher collision frequency facilitates the encounter of every Cd ion reaching the outer surface of the shell, even though the sticking probability stays intrinsically low. The authors further analyzed the correlation between the nature of the S source and the architecture of the resulting CdS nano(hetero)structures. When elemental S dissolved in *o*-dicholorobenzene (DCB) was employed as S source, hollow CdS NCs were formed; differently, the use of tri-*n*-octylphosphine sulfide (TOP-S) complex led to the formation of all-solid CdS NCs at the same reactant molar ratio ($([S]/[Cd] = 8)$). It is known that the TOP-S complex is a more stable sulfur source than molecular S dissolved in DCB and, in addition, it exhibits low diffusivity in solution. Therefore, sulfidation of Cd occurs at a slower rate with TOP-S than with elemental S, resulting in all-solid CdS NCs.

Besides the concentration and the source of the chemicalization agent, the diffusivity of the species acting as chemicalization agents also affects the final architecture of the transformation products. Ibanez et al. have investigated the effect of the diffusion rate of anions in a set of oxidative NC conversions.[43] In their study, Cd NCs were allowed to react with elemental chalcogenides, including O_2, S, Se, and Te to form different nanostructures (Figure 6a). When reacted with O_2, urchin-shaped CdO particles were obtained. Differently, the reaction of Cd NCs with an excess of S dissolved in dichlorobenzene (DCB:S) resulted in hollow CdS NCs. Hollow NCs of CdSe and CdTe were also obtained by reacting the Cd seeds with TOP-Se and TOP-Te complexes, but the as-derived nanostructures featured different inner-to-outer radius ratios (RI/RO). Hollow NCs of CdS were characterized by higher RI/RO, compared to their CdSe and CdTe counterparts. The different synthesis outcomes were explained by considering that anions can diffuse faster than cations in CdTe and CdSe, whereas the diffusion coefficients of anions and cations in CdS are similar.

Similarly, Xiao et al. investigated the formation mechanism of hollow $Cu_{2-x}Te$ NCs and $Cu@Cu_{2-x}Te$ core-shell MSHs in the chalcogenization process of in situ formed Cu NCs.[54] The overall evolution was traced during the synthesis course by TEM (Figure 6b–e), allowing the deciphering of a plausible mechanistic picture (Figure 6f). First, the solid Cu NCs were formed upon reduction of copper (II) acetylacetonate with dodecylamine at 250 °C. Then, injection of TOP-Te solution into the mixture resulted in the formation of $Cu_{2-x}Te$ NCs, in which an inner void developed and slowly increased in volume due to Kirkendall diffusion. Despite the fast diffusivity of Te species, the transition to the hollow NCs was observed to be preceded by the formation of $Cu@Cu_{2-x}Te$ core-shell MSH intermediates, which could eventually be extracted and isolated.

2.3.3. Influence of Capping Ligands

Organic ligands are used to stabilize NCs in solution by binding to coordinatively unsaturated surface atoms. However, the nature of these molecules can affect any chemicalization process significantly. For example, Doan et al. have studied the oxidation of Co NCs stabilized by different types of ligands, namely alkyl amines and carboxylic acids.[33] When stabilized with tridodecylamine, an oxide shell of 0.8 nm thickness was obtained after a specified reaction time (on the order of few minutes). When amines were replaced with carboxylic acids, the thickness of the oxide shell grew up to 1.2 nm after an identical duration of the oxidation treatment. After exposure to atmospheric oxygen for a quite long period (6 months), amine- and acid-stabilized Co NCs were transformed to Co@CoO core-shell MSHs and hollow CoO NCs, respectively. This behavior could be explained with the support of the Cabrera–Mott theory illustrated earlier. When acids are used as ligands, carboxylate anions that are made available in the solution and approach the NC seed surface are expected to enhance the intensity of the electric field across the region between the metal and metal oxide shell. This allows a higher flux of Co(II) toward the CoO shell, which promotes the formation of hollow CoO nanostructures, in agreement with the experimental findings.

The solubility of ligands in different solvents also affects the types of nanostructures that may be obtained through chemicalization.[23] A case study is illustrated in Figure 6g–k. When oxidation of tetradecylphosphonic acid (TDPA)-capped Cu NCs was carried out in hexane, $Cu@Cu_2O$ core-shell MSHs were formed. Upon changing the liquid medium to chloroform, hollow Cu_2O NCs were obtained instead. On the basis of control experiments, TDPA was found to relatively more soluble in chloroform than in hexane. Hence, the Cu NCs dispersed in chloroform could be expected to be more sensitive to oxygen exposure (compared to the same seeds in hexane), a condition that could account for the formation of hollow Cu_2O NCs. Further, annealing at 200 °C led to the formation of solid Cu_2O NCs.

2.3.4. Influence of the Size and Crystal Structure of the Seeds

In NCs, the surface area to volume ratio scales inversely with the NC size. Therefore, when involved in a transformation driven by a reaction with specific chemicalization agents, comparatively smaller NCs are likely to react at a much faster rate, unless the energy cost for heterointerface formation is prohibitively high. Hence, hollowing may be expected to be more pronounced in smaller NCs; on the other hand, larger NCs may be expected to more easily evolve to yolk-shell or core-shell type MSHs. This prediction has been supported by many experimental data. However, the ranges of seed size over which either hollow structures or yolk-shell/core-shell architecture may be preferentially obtained, respectively, vary broadly, depending on the particular metal subjected to chemicalization. For example, when Cu, Zn, and Al NCs were oxidized under similar conditions, hollow NCs were produced via the Kirkendall effect, yet showing dissimilar size dependence of their reactivity.[28,34] When subjected to oxidation, both smaller and larger Cu NCs were converted into hollow Cu_2O particles because of the faster outward migration of Cu ions through the oxide layer compared to the inward migration of oxygen ions. Similarly, when smaller Al and Zn NCs were subjected to oxidation, hollow amorphous oxide nanoparticles were obtained because of the rapid outward migration of metal ions.[28,34] On the contrary, when larger Al or Zn NCs underwent oxidation, growth of the oxide layer stopped after the formation of a thin shell of oxide layer on the NC surface, leading to core-shell type $Al@Al_2O_3$ and Zn@ZnO MSHs. The hollowing of small NCs could again be explained on the basis of the Cabrera-Mott theory.[53] The considerably low mobility of Al and Zn ions across their respective oxide lattices, enabled by a thermally activated vacancy mechanism, compared to cation diffusivity in Cu NCs, explains the fact that the growth of an Al_2O_3 or ZnO layer on larger Al or Zn NCs arrested after a critical thickness was achieved, eventually allowing the formation of core-shell type MSHs.[28,34]

Analogous findings were reported for the oxidation of different-sized Fe nanoparticles. Fe seeds smaller than 8 nm could be oxidized completely and usually contain a single void in the middle.[35] When Fe seeds larger than 10 nm were used, core-shell MSHs were formed, which contained an α-Fe core embedded within a shell consisting of either Fe_3O_4 or γ-Fe_2O_3. Railsback et al. discussed the size-dependent nanoscale Kirkendall effect during the oxidation of Ni NCs in air.[21d] The authors showed that the oxidation of Ni started with the formation of an initial NiO thin shell (with 3 nm thickness). Once the Ni/NiO interface had been created, either a single or multiple voids nucleated

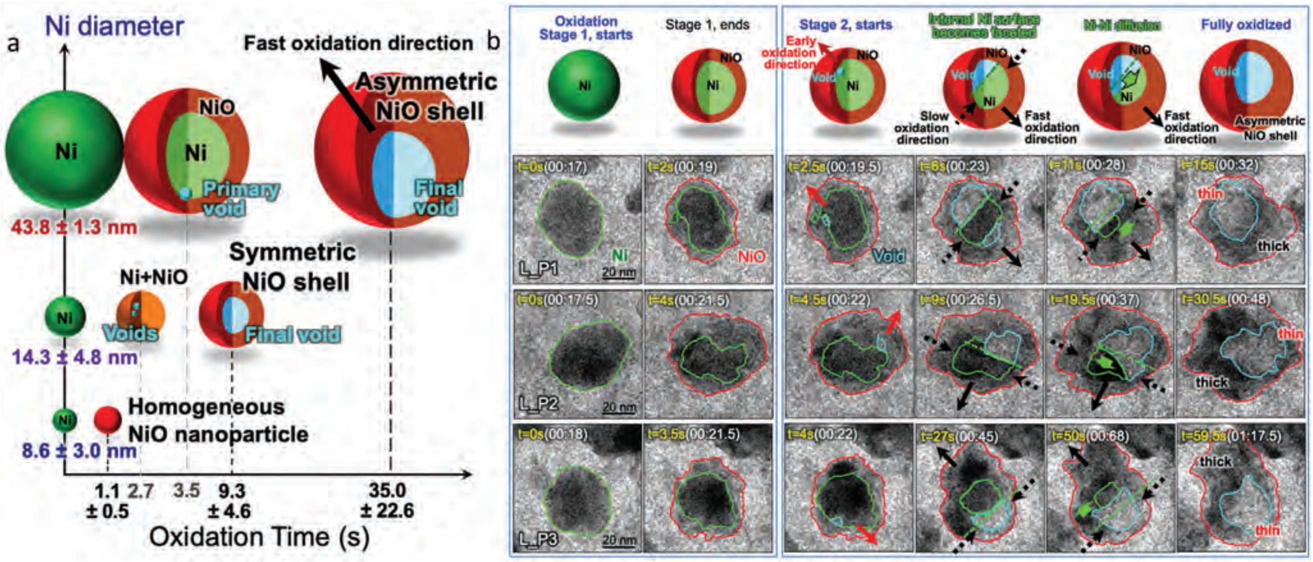

Figure 7. Case studies on the influence of the size of the seeds on the formation of MSHs upon chemicalization of monometal NCs. a) Schematic of oxidative evolution of Ni NCs as a function of reaction time and NC size. b) Schematic of the two-stage oxidation process of large Ni NCs (upper panel) and time-resolved in situ ETEM video snapshots of representative Ni NCs (lower panel) during oxidation at 600°C. Different segments of metal, metal oxide, and voids are marked by green, red, and turquoise outlines, respectively. Early oxidation directions are indicated with red arrows. Solid black arrows denote the fast oxidation directions that underlie NiO thickening, while broken black arrows mark the slow oxidation directions. Dashed green lines indicate the faceted internal Ni surface; thick green arrows point to the diffusion direction of the faceted internal Ni surface. Reproduced with permission.[36] Copyright 2022, American Chemical Society.

at the interface and grew until all the Ni was converted to NiO. Differences in the void formation and growth processes accompanied the size-dependent evolution of the nanostructures. In the case of smaller (9 nm) and larger (26 nm) seeds, a single void formed at the Ni/NiO interface, which grew by moving across the lattice. Conversion to NiO occurred at the side opposite the void location. Eventually, the void-containing Ni/NiO MSHs were characterized by different Ni/NiO volume ratios: the 9 nm seeds accommodated a nearly radially symmetric NiO shell, while the NiO shell formed on the 26 nm seeds exhibited a pronounced asymmetry. By regulating the oxidation temperature and the reaction time, partially oxidized Ni@NiO core-shell MSHs could be synthesized with good control over their geometric features. Finally, in the case of 96 nm seeds, multiple voids formed and grew, thus NiO NCs with the porous structure were eventually obtained.

Figure 7 summarizes the results of a detailed investigation of the size dependence of the chemicalization process. Sainju et al. explored the oxidation kinetics of Ni NCs with different sizes (4-50 nm) by using in situ gas-cell environmental TEM (ETEM).[36] While smaller Ni NCs were entirely oxidized into NiO, larger Ni NCs could be converted only partially, resulting in Ni@NiO core-shell MSHs. With increases in size, the core-shell structure changed from symmetric to asymmetric (Figure 7a). To explain the experimental evidence, the authors proposed a two-stage oxidation process (Figure 7b). Stage I involved surface oxidation and initial thickening of the NiO shell; stage II involved Wagner diffusion-balanced thickening of the NiO shell. In stage I, inward retraction of the original Ni surface was observed, which was regarded to occur at a critical thickness. In the case of Ni NCs having a radius smaller than the critical thickness, oxidation is arrested at stage I, leading to the formation of homogeneous all-solid NiO NCs. The inner surfaces of the Ni cores became faceted in larger NCs as voids grew inside. The final product consisted of asymmetric hollow NiO NCs with thick sections as a result of the NiO shell having developed preferentially (hence, faster) in directions orthogonal to the interior faceted surfaces of the Ni cores underneath. On the contrary, the thickening of the NiO shell took place much more slowly and essentially stayed constant throughout the subsequent oxidation process in the directions parallel to the aforementioned internal Ni facets. Continued expansion of the NiO shell occurred by diffusion of Ni ions through grain boundaries, resulting in the creation of hollow (i.e., with no core inside) NiO shells. The fact that the contact interface between the Ni core and NiO shell remained intact during the oxidation process suggested that the diffusion process of Ni ions was readily counterbalanced by self-diffusion of the Ni atoms in the core.

Not only size but also the crystal habit of the seeds can have a significant influence on the morphology of the final nano(hetero)structure. Representative case studies are illustrated in **Figure 8**. Among the first investigations on this subject, Tang et al. verified the impact of the crystal structure of the starting NC seeds on the type of architectures obtained after chemical transformation (Figure 8a,b).[48] The authors conducted two sets of experiments, in which distinct types of Ag seeds, namely single-crystalline and multiply twinned NCs, were independently exposed to the active Se species generated upon photo-dissociation of CSe_2 on the surface. It was observed that the single-crystalline seeds converted to hollow Ag_2Se NCs through the nanoscale Kirkendall effect. The faster diffusion of Ag atoms, compared to Se atoms, during the reaction led to the formation of vacancies that subsequently condensed into a void. On the contrary,

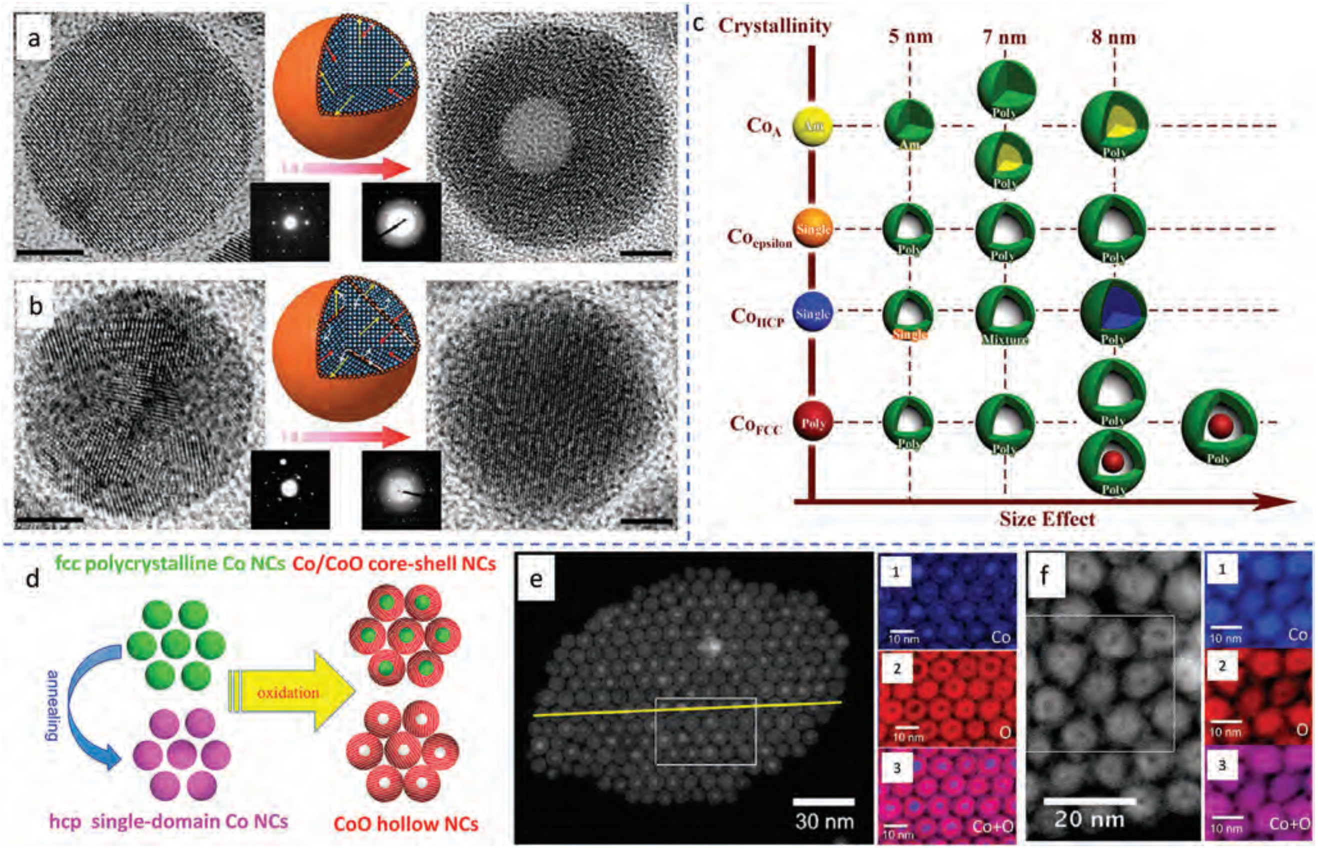

Figure 8. Case studies on the influence of the crystal structure of the seeds on the formation of MSHs upon chemicalization of monometal NCs. a) HRTEM image, single-particle electron diffraction (SPED) (bottom inset) of a single-crystalline Ag NC (left) and of an as-derived single-crystalline hollow Ag_2Se NC (right). Schematic of the possible atomic diffusion paths is shown in the middle. b) HRTEM image, SPED of a multiply twinned Ag NC (left) and of an as-derived all-solid single-crystalline Ag_2Se NCs (right). Schematic of the possible atom diffusion paths is shown in the middle. In the schematics, blue and orange spheres represent Ag and Se atoms, respectively; yellow and red arrows represent outward Ag and inward Se atom fluxes through the lattice, respectively; the dark grey spheres highlight Ag atoms in the twinning boundaries, providing a fast diffusion path for both Ag and Se atoms (white arrows). Scale bar of HRTEM images: 5 nm. Reproduced with permission.[48] Copyright 2007, Springer Nature. c) Schematic of MSHs obtained as the product of oxidation of Co NCs with different sizes and crystal structures. Reproduced with permission.[37] Copyright 2015, Wiley-VCH. d) Schematic illustration of the oxidation behavior of two-dimensional superlattices made of hexagonally ordered Co NCs differing by their crystal structure. e) HAADF-STEM images and corresponding elemental mapping of Co@CoO core-shell MSHs obtained after oxidation of two-dimensionally organized Co NC superlattices. f) HAADF-STEM images and corresponding elemental mapping of hollow CoO NCs obtained after oxidation of two-dimensionally arranged single-domain *hcp*-Co NC superlattices. Reproduced with permission.[38] Copyright 2013, American Chemical Society.

in the multiply twinned seeds, the motion of atoms along the defects allowed inter-diffusion of the Se and Ag species, which ultimately resulted in all-solid homogeneous Ag_2Se NCs. This fact suggested that void formation could be suppressed by native lattice defects present in the starting NC seeds.

Analogous results were documented for Co NCs. Yang et al. performed a detailed study on the roles played by size and crystal phase in the Kirkendall mechanism.[37] The outcomes of systematic experiments, in which Co NCs with different sizes (4-10 nm) and crystal structures, including amorphous, polycrystalline face-centered cubic (*fcc*), single-crystalline hexagonal close-packed (*hcp*), and single-crystalline ϵ-phase were subjected to controlled oxidation, were examined (Figure 8c). The smallest-sized amorphous Co seeds were converted into all-solid CoO NCs; conversely, with increasing seed size, the distribution of oxidation products featured a transition from all-solid CoO NCs to Co@CoO core-shell MSHs. It was expected that, for larger seeds, once an oxide layer of a certain thickness had been formed, diffusion of ions became hindered, thus leading to core-shell type MSHs. As opposed, smaller-size single-domain ϵ-Co seeds transformed into hollow CoO NCs, a fact that could be explained on the basis of the highly crystalline nature of the precursor seeds. In the case of amorphous seeds, atoms move in a disordered manner and hence comparatively slowly, a condition that allows the formation of solid CoO NCs However, in the case of the crystalline ϵ-Co seeds, atoms can diffuse along the lattice, which makes the oxidation easier, thus explaining the evolution of hollow CoO NCs. In the case of the ϵ-Co seeds, NC size did not impact the oxidation outcome to any significant extent. On the other hand, single-domain *hcp*-Co seeds behaved differently: smaller-sized seeds transformed into hollow structures (as in the case of ϵ-Co), but the larger ones evolved to core-shell MSHs. The different outcomes could be rationalized by considering the particular lattice arrangement of the respective seeds. The ε-Co

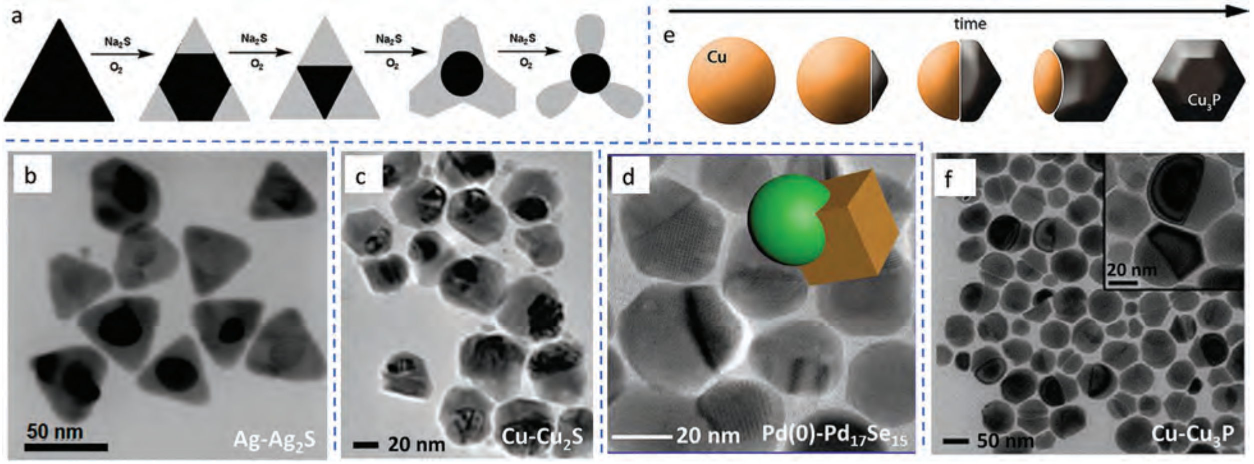

Figure 9. Case studies on the influence of the shape (faceting) of the seeds on the formation of MSHs upon chemicalization of monometal NCs. a) Schematic of the structural evolution achieved via the sulfidation process of Ag nanoprisms. Reproduced with permission.[44] Copyright 2011, Wiley-VCH. b) TEM image of the Ag-Ag$_2$S flower-shaped MSHs. c) TEM image of Cu-Cu$_2$S heterodimer MHSs obtained upon the reaction of a solution of Cu NCs with DDT. Reproduced with permission.[46] Copyright 2010, American Chemical Society. d) TEM image of Pd-Pd$_{17}$Se$_{35}$ Janus-type MSHs. Reproduced with permission.[49] Copyright 2015 American Chemical Society. e) Sketch of a chemicalization-based synthesis approach to Cu$_3$P NCs. In the standard approach, Cu$_3$P NCs evolve upon direct, homogeneous nucleation and continuous growth fed by suitable precursors. In the alternative chemicalization-based approach, disk-shaped Cu NCs are first generated, and then they are progressively phosphorized to Cu-Cu$_3$P Janus-like MSHs, in which the volume fraction of the evolving truncated bipyramidal Cu$_3$P domain increases over time. f) TEM image of Cu-Cu$_3$P Janus-type MSHs. Reproduced with permission.[50] Copyright 2012, American Chemical Society.

NCs have a cubic crystalline structure, which is less compact, compared to the hexagonal *hcp* structure. Hence, the diffusion rate of Co atoms across ϵ-Co can be expected to be higher than across *hcp*-Co, thus facilitating the formation of the observed core-shell type MSHs. In the small-size regime, Co seeds with the dense but polycrystalline structure of *fcc*-Co behaved like their hexagonal close-packed counterparts, whereas populations of larger seeds evolved to mixtures of hollow NCs and yolk-shell MSHs. This evidence indicates that, even when the seeds share the same type of atomic packing, the presence of defects, such as grain boundaries in polycrystalline lattices, could significantly affect their reactivity, thus playing a role in the selection of (hetero)nanostructure types that may eventually be formed upon chemicalization.

Finally, it deserves to be mentioned that oxidation of Co NCs was found to be additionally controlled by their ordering mode in corresponding NC-based superlattices. Yang et al. demonstrated that either Co@CoO core-shell MSHs or hollow CoO NCs could be obtained, depending on the degree of diffusivity of O$_2$ across NC superlattices of two-dimensionally arranged Co NCs.[38] When organized into superlattices and subjected to oxidation, polycrystalline Co NCs transformed to Co@CoO core-shell MSHs, whereas single-crystalline *hcp*-phase Co NCs converted to hollow single-domain CoO NCs due to the favorable outward diffusion of Co ions over the inward diffusion of O anions (Figure 8d–f).

2.3.5. Influence of the Shape of the Seeds: Facet-Selective Chemicalization

Chemicalization of NCs has been shown to be affected by the shape of the seeds as a consequence of the diverse distributions of their enclosing surface facets. Representative cases are discussed on the basis of the data collected in **Figure 9**. Mel et al. have investigated the oxidation behavior of different types of Ag nanostructures.[39] Oxidation of near-spherical Ag NCs initiated with the formation of small Ag$_2$O clusters, distributed randomly on the surface. On completion, the process led to nanoporous Ag$_2$O NCs. However, oxidation of Ag nanowires resulted in rows of aligned Ag$_2$O nanoclusters over the surface. Such preferential growth mode was explained by invoking the presence of step-edges on the {100} facets along the nanowire axis, where the Ag atoms are less tightly bonded to the crystal lattice and, hence, can be oxidized more easily. However, full clarification of the mechanism underlying the observed behavior requires further investigations.

Chemicalization of anisotropic-shaped NCs is a transformative process that, in addition to being obviously affected by the crystal structure of the seeds, may be strictly dependent on the specific reactivity of the crystallographic facets exposed to the chemicalization agents. For example, Liu et al. synthesized Ag nanoprisms capped with polystyrene sulfonate polymer and carried out their sulfidation by treatment with Na$_2$S.[44] The nanoprism seeds were observed to decrease in size with increasing the amount of Na$_2$S added, eventually converting into flower- or trefoil-shaped structures at the highest Na$_2$S concentration set (Figure 9a). The authors rationalized that, at low concentration, Na$_2$S etched the seeds preferentially at their {110} facets rather than over the entire surface, which resulted in epitaxial deposition of Ag$_2$S domains on those locations, followed by inhibition of further reaction over the as-formed Ag-Ag$_2$S MSHs. Sulfidation started at the corners of the nanoprisms because of the weak or poor surface passivation by the capping polymer molecules thereon. With increases in Na$_2$S concentration, mass consumption of the Ag nanoprisms increased accordingly. With an excess Na$_2$S,

Ag_2S was still generated and the resulting Ag-Ag_2S MSHs were flower-shaped (a sketch of the overall evolution is presented in Figure 9a). In a subsequent systematic study, Shahjamali et al. demonstrated the synthesis of Ag@Ag_2S core-shell MSHs upon anisotropic sulfidation of Ag nanoprism seeds (Figure 9b). The MSHs consisted of a Ag polyhedral core covered with a centrosymmetric Ag_2S shell with varying thickness, which conferred a prismatic shape to the global heterostructure. The particular shell habit resulted from the dissimilar rates of sulfidation achieved at the corners and along the major (111) facets of the starting Ag nanoprism seeds, respectively.[45] The authors showed that depending on the reaction conditions, sulfidation occurred on the tips and/or the (111) facets, allowing the evolution of Ag/Ag_2S core-shell type MSHs.

Facet-dependent chemicalization was also assessed by Liu et al., who synthesized Cu-Cu_2S hetero-dimer and Cu-$Cu_{1.81}S$ hetero-oligomer MSHs by inducing Cu NCs to react with dodecanethiol (DDT) in Ar atmosphere either in the presence or in absence of H_2 gas.[46] Though the details of the mechanism underlying the formation of this type of MSH configuration have to be disclosed yet, it was clarified that sulfidation was initiated preferentially at selected facets exposed by Cu NC seeds, and proceeded sacrificially deeper into the seed lattice. Such anisotropic reaction pathways produced Cu-Cu_2S hetero-dimers, a kind of Janus-like nanoheterostructures, where a single Cu_2S domain eventually adhered to the remaining Cu portion of the original Cu seed NC, sharing a limited heterointerface (Figure 9c). The authors also demonstrated that a sufficiently slow supply of the S source was a prerequisite to guaranteeing the formation of these types of Janus MSHs. The use of the elemental S as a chemicalization agent, in place of the less reactive DDT, led to the complete conversion of the Cu seeds to Cu_2S NCs. In addition, it was considered that DDT could bind to the Cu NCs quite strongly, which could be expected to reduce the rate of the sulfidation reaction. Similar observations were reported by Guria et al.[49] These authors showed that the reaction of Pd NCs with a suitable Se source resulted in Pd-$Pd_{17}Se_{11}$ Janus MSHs (Figure 9d) However, when the reactivity of Pd NCs towards Se was enhanced with the aid of Ag^+ ions as promoters, hollow $Pd_{17}Se_{15}$ NCs were formed exclusively.

The necessity of regulating the extent of a chemicalization reaction to produce controlled MSHs was also emphasized by Trizio et al.[50] The authors elaborated on a one-pot synthesis scheme, originally designed for the preparation of Cu_3P NCs starting from CuCl, tri-*n*-octylphosphine (TOP), and tri-*n*-octylphosphine oxide (TOPO) in a hot mixture of alkylamines. In such environment, disk-shaped Cu NCs could initially be generated upon amine-driven reduction of CuCl, and then slowly phosphorized to an adjustable extent to yield either Cu_3P NCs or partially transformed Janus-like Cu-Cu_3P MSHs, the latter consisting of Cu and Cu_3P domains sharing a flat epitaxial interface (Figure 9e,f). TOP was identified as acting as a moderately reactive P source. The TOP concentration should be set to controllably low levels in order to guarantee the formation of Cu-Cu_3P MSHs with Janus architecture. The MSHs evolved through the initial nucleation of a Cu_3P domain on a selected surface site of each Cu seed and its progressive enlargement to a single truncated bipyramidal Cu_3P domain at the expense of the volume of the starting Cu seed. Presumably, the highly anisotropic reactivity or accessibility of the Cu seeds and the comparable solid-state diffusivities of Cu and P species prevented the formation of centrosymmetric Cu@Cu_3P core-shell MSHs and their possible evolution to hollow Cu_3P NCs via the Kirkendall effect. On the other hand, in syntheses carried out at exceedingly high concentrations of TOP, fast homogeneous nucleation of Cu_3P could only take place, followed by growth of the initially formed clusters via diffusion of monomer species provided by Ostwald ripening.

To generalize, two main factors can be regarded as setting the driving force for the formation of Janus-type MSHs over other types of nano(hetero)structures. If the surface of the precursor seeds is evenly covered by capping ligands bound with identical strength, or if it exposes facets with similar reactivity, the chemicalization front may be expected to advance in a centrosymmetric way, leading to the evolution of core-shell type architectures. However, if some seed facets are less stable or more accessible to the external medium compared to others due to weaker passivation by ligands, chemicalization can preferentially initiate at such locations, allowing sacrificial nucleation and growth of a small domain of the secondary semiconductor material on one side or on a reduced surface portion of the original metal seed, at the expense of a volume fraction of the latter. Consequently, Janus-type MSHs would result in. Yet, an open question remains as to why extended chemicalization proceeds steadily on the early nucleation sites, without involving other facets of the seeds at later stages. A plausible explanation could invoke a thermodynamic argument. It could be considered that, if the replacing material front advanced isotropically into the seed and attained a continuous coverage over the remaining (untransformed) seed lattice, then increasingly high misfit strain and/or induced charge polarization should be accommodated by the nanoheterostructure at the evolving interfaces. This would make a core-shell arrangement energetically disfavored over a Janus configuration, which could instead result from partial chemicalization proceeding along those crystallographic directions that allow global minimization of the interfacial energies.

From the outcomes of the experiments illustrated above, it can be concluded that Janus-type MSHs may be preferentially accessed over core-shell/yolk-shell MSHs and hollow NCs by manipulating the chemical reactivity and the thermodynamic stability of the evolving heterostructured system upon proper selection of the metal seeds (size, shape, crystal structure, etc.), the surface ligands, and the chemicalization agent(s) in a suitable liquid medium.

3. From Bimetallic Seeds to Metal–Semiconductor Nanoheterostructures

In comparison to monometallic NCs, bimetallic NC systems are more attractive as chemicalization substrates due to the breadth of potential applications of the MSHs that can be derived. A key issue here is the different reactivities of the two component metals of the seeds toward a given chemicalization agent, on which the final configuration of the as-derived MSH will strongly depend. Ideally, in order to generate MSHs with at least one bimetallic domain, one metal component should be inert, while the other metal should be specifically reactive towards the chemicalization agent. However, in most practical circumstance, both

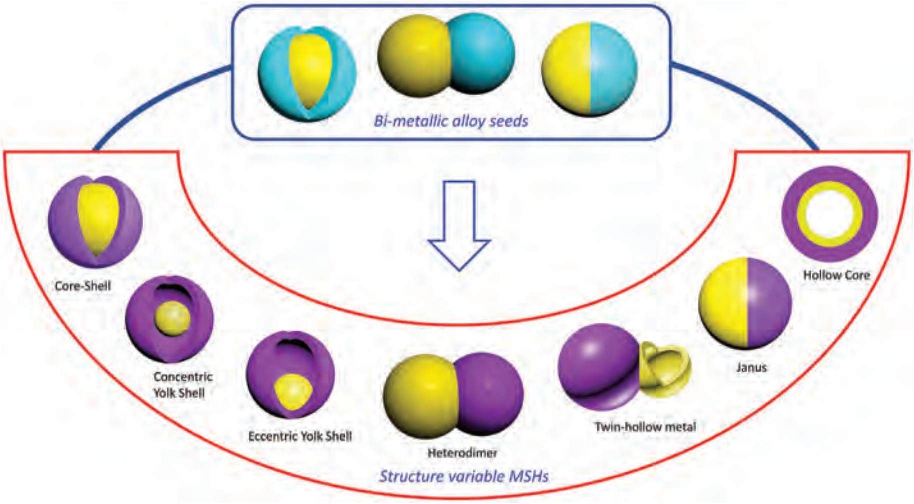

Figure 10. Possible chemicalization trajectories for the conversion of bimetallic NCs to MSHs. Schematic representation of MSHs that may be formed in different configurations through chemicalization of bimetallic NC seeds with either alloy structure, or a core-shell and Janus-type heteroarchitecture.

metal species can exhibit a certain degree of reactivity toward the chemicalization agent. However, by carefully adjusting the reaction conditions, the inertness of one of the active metal components can be secured, allowing the construction of MSHs similar to those obtained starting from mono-metallic NC seeds. In order to gain a proper understanding of the mechanisms underlying their formation, it is convenient to categorize the MSHs based on types of bimetallic NCs that may be exploited as the starting seeds, namely homogeneous alloy NCs, core-shell, and heterostructured Janus-type NCs. From bimetallic alloy seeds, either core-shell or Janus-type MSHs may be obtained. On the other side, from bimetallic core-shell seeds, symmetric or asymmetric yolk-shell, Janus and hollow metal-semiconductor MSHs can be fabricated; from Janus-type seeds, corresponding Janus MSHs can be derived. The architectural diversity with which MSHs can potentially be constructed is sketched in **Figure 10**. An overview of the structure-variable MSHs that have so far been synthesized by the chemicalization of bimetallic NC seeds is provided in **Table 2**.

One of the pioneer works on this topic was reported by Yin et al. in 2004, who selectively transformed the Co shell of the Pt@Co core-shell heterostructures to CoO. This route afforded Pt@CoO yolk-shell MSHs.[20] Later, following a similar approach, Shevchenko et al. developed a one-pot three-step synthesis of Au@Fe_3O_4 yolk-shell MSHs starting from Au@Fe core-shell seeds.[56] The reported procedure is still the most commonly exploited route to heterostructures with yolk-shell configurations.[55,99] Interestingly, in line with these achievements, Kim et al. fabricated long chains of interconnetced Au@Co_3O_4 core-shell MSHs.[57] In the documented case, by leveraging on magnetic dipolar interactions, Au@Co core-shell heterostructured NCs were first induced to “polymerize” into nano-chains of fused Au@Co domains; upon subsequent oxidation, the latter were converted to corresponding chain-like wires composed of Au@Co_3O_4 core-shell blocks. Gao et al. prepared FePt@CoS_2 yolk-shell MSHs starting from preformed FePt@Co core-shell heterostructured seeds and performing selective sulfidation of the Co shell with elemental S (it is remarkable that core-shell FePt@CoO MSHs were instead obtained by oxidizing the Co shell of analogous FePt@Co seeds).[100] A similar approach was also exploited to obtain magnetic-plasmonic nanodumbbell-like (a kind of Janus-type nanoheterostructure) Au-Fe_3O_4 MSHs.[101]

Other accounts demonstrated that MHSs with distinct configurations could be synthesized upon chemicalization of core-shell bimetallic seeds made of metal species exhibiting significantly different reactivities.[58] In general, when only the metal present in the shell of the seed is reactive towards the utilized chemicalization agent, a core-shell MSH with a semiconductor shell is obtained as the final product. On the other hand, when the metal present in the core of the seed is reactive toward the chemicalization agent, while the metal in the shell behaves as almost inert, chemical transformation leads to the formation of Janus MSHs composed of a hollow metal shell and a semiconductor core. Liu et al. prepared core-shell MSHs made of silver-chalcogenide-coated Au nanorods.[59] Taking into account the strong affinity of Ag to chalcogens, the authors manipulated the reaction of Ag@Au core-shell nanorods with thiourea/selenourea to achieve shape-conformal MSHs made of Ag@Ag_2S and Ag@Ag_2S core-shell nanorods. Later, starting from Au@Ag core-shell seeds with rod-like and cube-like morphologies, Au@Ag_2S core-shell MSHs with corresponding seed-conformal shapes were reported by Zhu et al. and Liu et al., respectively.[60,62] The shell of these MSHs could further be modified by partial cation exchange to generate Au@AgCdS MSHs.[60] Inspired by these strategies, Lambright et al. synthesized Au@CdS in two steps: first, Au@Ag core-shell seeds were treated with elemental S to obtain Au@Ag_2S core-shell MSHs; then, complete cation exchange of Ag^+ in the Ag_2S shell for Cd^{2+} enabled access to Au@CdS MSHs.[102]

The chemicalization of bimetallic alloy NCs to MSHs has been less explored than the transformation of bimetallic core-shell systems. For example, Guardia et al. performed partial selenisation of AuCd alloy NCs with a TOP-Se complex to generate Au_2Cd@CdSe core-shell MSHs where the alloy core featured a modified stoichiometry, relative to that of the starting seeds.[74]

Table 2. Summary of structure-variable MSHs obtained upon chemicalization of bimetallic seeds.

Type of bimetallic seeds	Chemicalization Agent	Structure of as-derived MSHs	Reference
Au@Fe core-shell	O_2	Au@γ-Fe_2O_3 core-shell Au@γ-Fe_2O_3 yolk-shell	[56]
Au@Co core-shell	O_2 bubbles	Au@Co_3O_4 yolk-shell	[57]
Au@Ag core-shell	S powder and dodecanethiol in toluene	symmetric and asymmetric Au@Ag_2S core-shell	[58]
Au@Ag core-shell	Na_2S	Au@Ag_2S core-shell	[59]
Au@Ag core-shell	NaHS	Au@Ag_2S core-shell	[60]
Au@Ag core-shell nanorod	Se powder and aqueous hydrazine Aqueous $Cd(NO_3)_2$ and TBP	Au/Ag_2Se core-shell nanorod and Ag_2Se-Au-Ag_2Se nanodumbbell Au-CdSe nanodumbbell	[61]
Au@Ag core-shell	Selenourea	Au@Ag_2Se core-shell	[59]
Au@Ag core-shell	Thiourea	Au@Ag_2S core-shell with voids	[62]
Au@Ag core-shell	Elemental S	$Au_{1-x}Ag_x$/AuAgS and $Au_{1-x}Ag_x$/Au_3AgS_2 core-shell and heterodimer	[63]
Au@Ag core-shell	Elemental S	Au@Ag_2S core-shell	[64]
Au@Ag core-shell	Elemental S and Se	Au@$Ag_2S_{1-x}Se_x$ core-shell	[64]
M/Ag heterodimer or core-shell	TOP-S or TOP-Se complex	Non-centrosymmetric M-Ag_2X or M-CdX (X = S, Se) hetero-oligomer	[65]
Au@Ag core-shell nanorod Ag@M (M = Ru, Rh, Pd, Pt, Ir) core-shell Au@Ag@Pt core-shell-shell	Elemental S and Se with aqueous hydrazine and EDA Aqueous $Cd(NO_3)_2$ and TBP Elemental S Elemental S	$CdSe_xS_y$-Au-$CdSe_xS_y$ nanodumbbell or Au@$CdSe_xS_y$ core-shell nanorod with Ag-doped $CdSe_xS_y$ Ag_2S-hollow M heterodimer Ag_2S-cage bell Au-Pt heterodimer	[66] [67a] [67a]
Ag@Pt core-shell	Se powder	Ag_2Se-hollow Pt heterodimer	[67b]
Ag@Pt core-shell	Elemental S $HAuCl_4$-dodecylamine complex	Au-Ag_2S-hollow Pt heterotrimer	[67c]
Au@Ag core-shell	Elemental S	Au@Ag_2S core-shell	[69]
Pt@Co core-shell	Elemental S	Pt@Co_xS_y yolk-shell	[20]
Au@In core-shell		Au-In_2O_3 heterodimer surrounded by a thin In_2O_3 shell	[70]
Ag@AgPd core-shell	Elemental S	Ag_2S-hollow Pd heterodimer	[71]
Cu@Ni core-shell	White Phosphorus (P_4)	Hollow (Ni, Cu)$_2$P	[72]
Au@Ag core-shell	Elemental S	Au@Ag_2S core-shell nanoribbon	[73]
AuCd alloy	TOP-Se complex	Au_2Cd-CdSe core-shell	[74]
Au-Cu alloy	S and O_2	Au-Cu_2S heterodimer	[75]
Au-Ag alloy	O_2	Au-Ag_2O yolk-shell	[76]

(*Continued*)

Table 2. (Continued).

Type of bimetallic seeds	Chemicalization Agent	Structure of as-derived MSHs	Reference
Au-Cu alloy	Dodecanethiol and bubbling O_2	Au-Cu_2S heterodimer	[77]
Au-Cu alloy	Thioacetamide	Au@CuS and Au@$Cu_{1.8}S$ core-shell	[78]
Au-Cu alloy	Selenourea	Au@CuSe and Au@$Cu_{1.8}Se$ core-shell	[78]
Cu-Pt alloy	Elemental S	Pt-CuS heterodimer	[79]
Co-Ni alloy	S powder	Yolk-shell CoNiS with single or multiple voids; hollow CoNiS	[80]
Au-Cd alloy	TOP-Se complex	Au@CdSe core-shell	[81]
Ni-Co alloy	O_2	$Ni_xCo_yO_z$ @$Ni_xCo_yO_z$ core-shell having multiple voids and Co-enriched shell	[82]
Au_y-Cu_{1-y} alloy	O_2	Au_xCu_{1-x}−Cu_2O heterodimer	[83]
Au-Cu alloy	Se in oleylamine	Au@$CuInS_2$ core-shell	[84]
Au-Ag alloy	S	nanowires with periodically arranged AuAg and Ag_2S segments	[16j]
Au-Ag alloy nanoframe	S	Au-Ag_2S nanoframe	[85]
Ni-Fe alloy	O_2	hollow, porous and dual-cavity Ni_xFe_yO	[86]
Pt-Ni alloy	O_2	Pt-NiO heterodimer	[87]
Au-Cu alloy	O_2	AuCu@CuO yolk-shell	[88]
Au-Cu alloy (face centered cubic)	Air	Au@CuO core-shell	[89]
Au-Cu alloy (face centered tetragonal)	Air	AuCu@CuO core-shell	[89]
Au-In alloy	O_2	AuIn@In_2O_3 core-shell	[90]
Pb-Bi alloy	O_2	Bi-PbO heterodimes with holes in PbO domain	[91]
Pb-Bi alloy	O_2	Bi@PbO core-shell with voids in the PbO segments	[91]
Ni-Co alloy	Thioacetamide	$NiCo_2S_4$ hollow frame	[92]
Pt–Ni rhombic dodecahedron NCs with segregated Pt frames	O_2	Pt@NiO yolk–shell	[87]
Pt-Ni Nanowire	O_2	Pt/NiO nanopeapods with voids	[93]
PtCo NCs	O_2	Pt-decorated hollow Co_3O_4	[94]
Multi-segmented Ni/Pt nanowires	O_2	NiO nanopods embedded with equally spaced Pt nanopeas	[93]
Au-Ni heterodimer	Triphenylphosphine	Au@$Ni_{12}P_5$ core-shell	[95a]
Au-Ni heterodimerAu-Ni heterodimer	$HAuCl_4$ and oleylamine	Au-Ni heterodimer with larger Au domain	[95b]
	$HAuCl_4$ and didodecyldimethylammonium bromide	Au-NiO heterodimer with hollow NiO domain; hollow NiO spheres	[95b]
Ag-Cu heterodimer	Phosphine	Ag-Cu_3P heterodimer	[96]
Au-Fe heterodimer	O_2	Au-Fe_3O_4 core-shell and heterodimer	[97]
Au-Ni heterodimer	Hexaethyltri-aminophosphine	Au-Ni_2P heterodimer	[98]
Cu-Co heterodimer	S powder	Heterodimer of CuS-CoS with a void in one or both domains	[80]

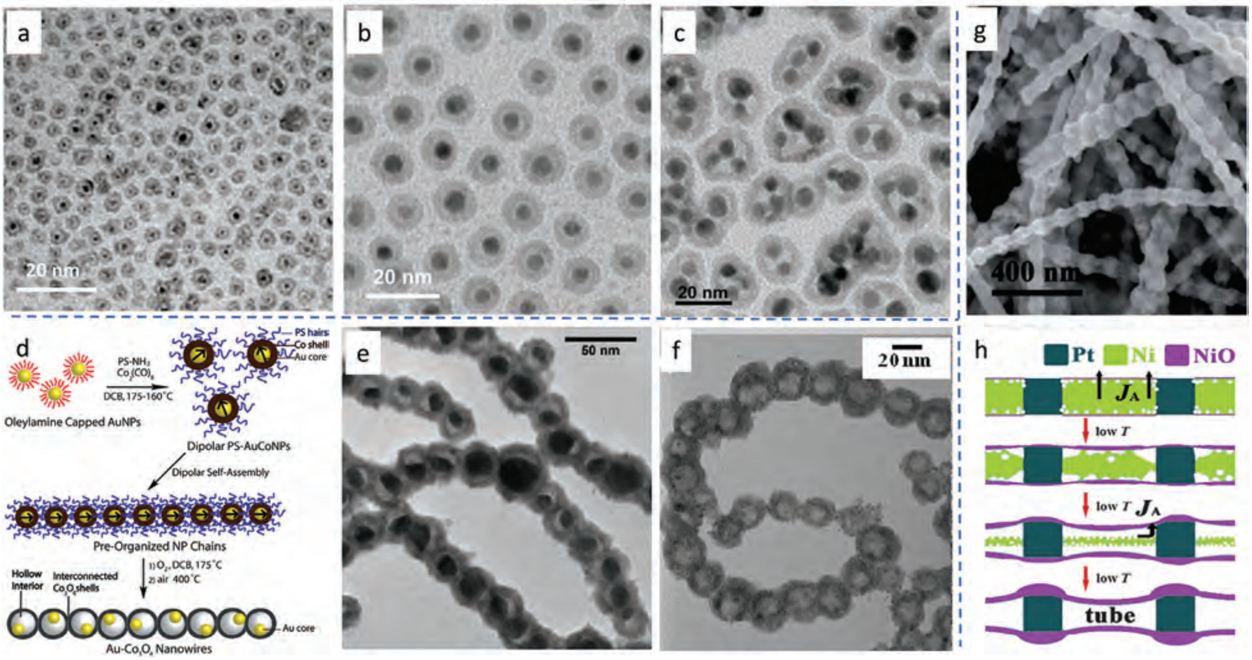

Figure 11. Examples of core-shell MSHs with hollow compartments, synthesized upon chemicalization of bimetallic core-shell seeds. a) TEM image of Pt@CoO yolk-shell MSHs. Reproduced with permission.[20] Copyright 2004, American Association for the Advancement of Science. b) TEM image of Au@iron-oxide yolk-shell MSHs. c) TEM image of Au@iron-oxide yolk-shell nanocapsule having multiple Au cores inside an iron oxide shell. Reproduced with permission.[56] Copyright 2008, Wiley-VCH. d) Schematics of the synthesis and e) TEM image of chain-like heterostructure composed of joint Au-Co_3O_4 yolk-shell MSHs. Reproduced with permission.[57] Copyright 2010, American Chemical Society. f) TEM image of nanowires made of connected Pt-Co_3O_4 yolk-shell MSHs. Reproduced with permission.[94] Copyright 2011, American Chemical Society. g) SEM image of electrodeposited multisegmented Ni/Pt nanowires and h) representation of their modification into hollow heterostructured Pt/NiO nanopeapods. Reproduced with permission.[93] Copyright 2011 Wiley-VCH.

The chemicalization of bimetallic alloys has frequently been shown to lead to the formation of Janus heterostructures. The process is primarily governed by a phase-segregation mechanism, following which the non-reactive metal component stays localized in a specific section of the final multiphase heterostructure, while the reactive metal component, which undergoes chemical conversion, is extruded to yield a separate semiconductor domain. In one of the pioneer works, Motl et al. have shown that the chemicalization of AuCu NCs with elemental S accompanied by bubbling O_2 yields phase-segregated Au−Cu_2S Janus MSHs.[75] O_2 was identified to play a vital role in the formation of heterostructures. Ding et al. confirmed the importance of O_2 in the synthesis of similar Janus MSHs by sulfidation of AuCu NCs with an alkylthiol.[77] However, as discussed in the next Section, the underlying mechanisms of MSH evolution were different in the aforementioned cases. In a later account, Ding et al. have studied the effect of temperature and sulfur source on the morphology of Pt-CuS heterodimer MSHs derived upon chemicalization of from PtCu alloy NCs.[79] However, knowledge of the transformation of bimetallic NCs to core-shell or Janus MSHs is still limited and needs further investigation to be expanded.

3.1. Mechanistic Aspects of the Transformations of Bimetallic Seeds to Metal-Semiconductor Nanoheterostructures

The mechanisms of chemicalization in bimetallic NC systems differ significantly from those involved in the transformation of monometallic systems. Unfortunately, to date, their understanding remains marginal. Complete chemicalization of monometallic NCs, in most circumstances, results in hollow nanostructures due to the Kirkendall phenomenon. On the other hand, MSHs can be generated from appropriate bimetallic seeds by using suitable chemicalization agents.

3.1.1. Chemicalization of Core-Shell Seeds

Representative case studies illustrating the outcome of the chemicalization of core-shell seeds to yield core-shell MSHs with void compartments are provided in **Figure 11**. To the best of our knowledge, Yin et al. were the first to elaborate a protocol to transform core-shell NCs.[20] They induced the conversion of colloidal bimetallic Pt@Co core-shell NCs to Pt@CoO yolk-shell MSHs by purging the reaction medium with O_2 at ~180°C (Figure 11a).[20] The process is initiated with the formation of a thin CoO layer at the expense of the Co shell on the Pt cores of the seeds. Subsequently, a vacant space in between the shell and the core section was created, most likely due to faster outward diffusion of Co atoms. Shevchenko et al. investigated the impact of the Kirkendall diffusion process on various core-shell systems.[56] Among these, Au@iron-oxide yolk-shell MSHs were synthesized by oxidation of preformed Au@Fe core-shell seeds, which had been obtained by the decomposition of $Fe(CO)_5$ on Au seeds. The iron shell was oxidized to iron oxide upon air exposure, but Au remained unaffected. The formation of the yolk-shell architecture was explained as arising from the large difference in diffusion rates of iron and oxygen atoms across the respective lattices (Figure 11b). The same authors had also succeeded in the synthesis of an unconventional prototype of yolk-shell MHSs, in which multiple Au NC cores were embedded within an iron-oxide capsule (Figure 11c).[56] This result was achieved by changing the capping ligands on the Au NCs from oleic acid to TOPO during the Au-seeded decomposition of $Fe(CO)_5$ in which the starting Au@Fe core-shell NC substrates were generated. Unlike oleic-acid-capped Au NCs, which are negatively charged, TOPO-capped Au NCs are neutral. Thus, due to the reduced electrostatic repulsion, the TOPO-capped Au NCs could experience a higher probability of sticking upon collision and catalyze the decomposition of $Fe(CO)_5$ at their surface. As a result of the favorable conglomeration conditions, clusters made of several Au@Fe core-shell NCs self-assembled in the initial synthesis stages. Subsequent oxidation led to the formation of Au@iron-oxide yolk-shell MSHs, in which several Au cores remained trapped within a single iron-oxide shell with intervening voids.

Using a similar metallorganic decomposition method, Kim et al. demonstrated the formation of Au-Co_3O_4 core-shell MSHs by oxidation of ferromagnetic Au@Co NCs.[57] During the thermolysis of $Co_2(CO)_8$ in amine-terminated polystyrene (PS) surfactants, hybrid PS-capped Au@Co core-shell NCs were first produced, which then self-assembled into chain-like structures driven by electrostatic dipolar interactions. Subsequent oxidation of Co and removal of the PS cores led to chain-like nanowire structures composed of interconnected Au-Co_3O_4 yolk-shell MSHs (Figure 11d,e). Similarly, Keng et al. synthesized nanowire structures made of Pt@Co_3O_4 core-shell units each containing a Pt NCencased within a hollow Co_3O_4 matrix (Figure 11f).[94] To fabricate these nanoarchitectures, PS-capped Co NCs, pre-organized into chains, were first decorated with Pt NCs upon decomposition of $Pt(acac)_2$, then subjected to oxidation, which resulted in the final Pt@Co_3O_4 yolk-shell nanowires. Further, Yang et al. reported a highly uniform wavy Pt-NiO hollow nanopeapods by controlling the oxidation of Ni in multisegmented Ni/Pt nanowires (Figure 11g).[93] These nanoheterostructures were formed by outward diffusion of Ni-based on the field-driven oxidation mechanism: the pristine Ni segments were converted into polycrystalline NiO tubular compartments with a uniform wall thickness, which alternated to the unreacted Pt domains (Figure 11h).

Bimetallic yolk-shell MSHs with an internal hollow compartment were also obtained using chemicalization agents other than molecular oxygen. Zhu et al. synthesized Au-Ag_2S nanorods that accommodated voids at the interface between the Au core and the Ag_2S shell by treating Au@Ag core-shell nanorod seeds with thiourea.[62] According to the proposed mechanistic picture, once the Ag_2S shell had formed over Au NRs, Ag atoms migrated outward, while diffusion of S atoms occurred inward toward the core. As the outward migration of Ag atoms was faster than the inward diffusion of S atoms, vacancies were generated at the Au/Ag_2S interface. As the reaction progressed, vacancies accumulated continually, condensing into a single void located on the side of the faster-diffusing species (core).

Bimetallic core-shell NCs with shells composed of coinage-metal elements have also been successfully exploited as starting substrates for the construction of centrosymmetric double-shell MSHs that accommodate a void and heterodimer MSHs that carry a hollow domain. Representative results are presented in **Figure 12**. Lewis et al. developed a prototype of a concentric double-shell Au@Ag_2O MSH (in other terms, a core-shell Au@Ag_2O MSH with a hollow Au core) by performing oxidation of Ag@Au core-shell NC seeds through sequential application of electron beam induced oxidation and in situ heating and quenching.[76] In situ aberration-corrected Scanning TEM (STEM) imaging, complemented with high-resolution chemical mapping by EDX spectroscopy of the structural-morphological transformation of the seeds provided insight into the mechanism of void formation and coalescence within the core along the course of the chemicalization process (Figure 12a,b). It was shown that in the early stage of oxidation, the nucleation of multiple Ag_2O clusters took place on Au shell of the Ag@Au seeds, as observed for other bimetallic systems. With the progress of oxidation, the Ag_2O nuclei grew in size and coalesced into a continuous shell of Ag_2O. Simultaneously, voids had evolved inside the Ag core and expanded until complete removal of Ag was achieved. Hence, the final MSHs consisted of contiguous concentric shells, the inner one made of Au and the other one made of Ag_2O. The observed evolution is in accordance with the Kirkendall diffusion mechanism that drives hollowing in nanostructures.

Heterodimer MSHs with a hollow metal domain can also be synthesized starting from core-shell seeds, of which the core material is more reactive towards the chemicalization agent than the shell material. By treating Ag@AgPd core–shell NCs with elemental S, Chen et al. produced Ag_2S-*h*Pd heterodimer MSHs in which a hollow Pd domain (*h*Pd) was attached to a Ag_2S domain (Figure 12c).[71] It could be assumed that during the incubation of the Ag@AgPd seeds with S, the Ag elements from the AgPd alloy shell were first etched away by dissolved O_2, after which the as-released Ag^+ ions reacted with S to form Ag_2S on the outer surface of the core-shell seeds. This led to the evolution of a Pd-enriched AgPd shell with a discontinuous structure, across which the establishment of ionic transport channels could facilitate the extraction of Ag^+ ions etched away from the Ag core. Continued reaction of the liberated Ag^+ ions with elemental S resulted in reiterated nucleation of Ag_2S on the outer surface of the modified seeds, including in proximity to the remaining Pd shell. While Ag^+ ion etching and the initial formation of multiple Ag_2S nuclei would likely occur uniformly over the AgPd shell surface, in the late reaction stages the as-deposited Ag_2S clusters could undergo ripening to form a single, thermodynamically stable, larger Ag_2S domain. This mechanistic picture would explain the observed transition to a well-defined Ag_2S–*h*Pd heterodimer architecture.

A general approach was developed by H. Liu et al. to synthesize a family of Ag_2S–*h*M (M = Pt, Pd, Rh or Rd) heterodimer MSHs, composed of one all-solid Ag_2S domain joint to one hollow metal portion (*h*M).[67a] The key strategy for the synthesis of these MSHs relied on the use of Ag@M core-shell NCs with a decahedral Ag core and a discontinuous, defective M shell as the starting seeds.[68] Due to their multiply twinned structure, the Ag cores of the seeds were inherently unstable towards dissolved O_2 and Cl^- ions (originating from the precursors used for their synthesis), so they could be slowly etched away, releasing Ag^+ ions that could diffuse through the permeable M shell into the solution, under the driving force of a favorable concentration

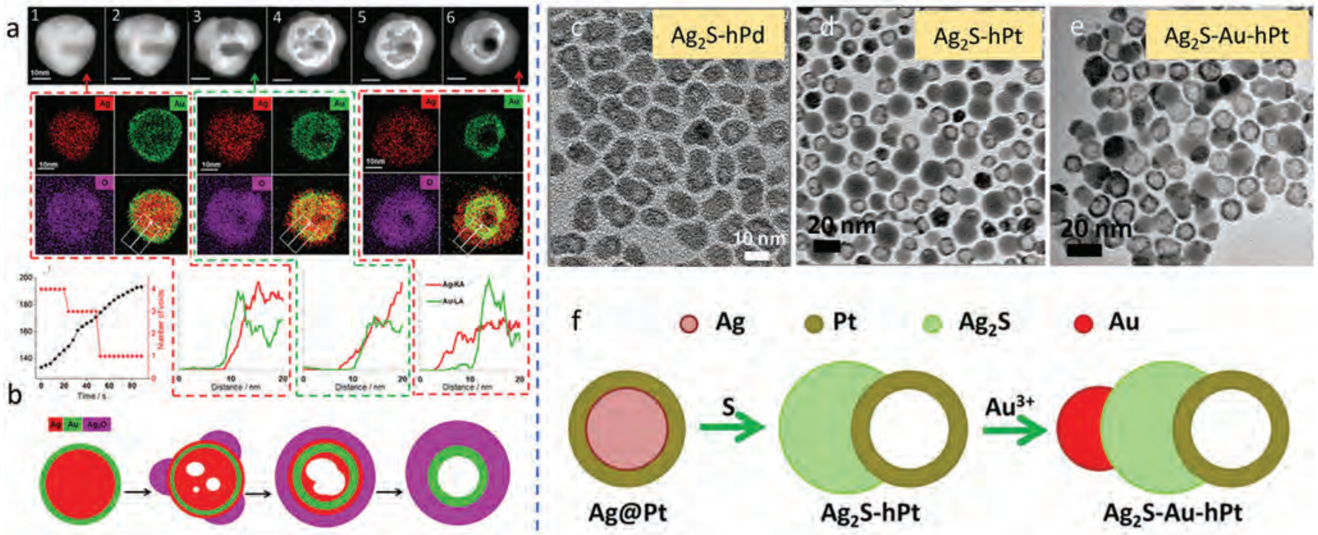

Figure 12. Examples of core-shell and heterodimer MSHs with hollow compartments, synthesized upon chemicalization of bimetallic core-shell seeds. a) HAADF-STEM image, and EDS elemental maps captured real-time during the morphological transformation of Ag@Au core–shell NCs into AgAu alloyed NCs, Au–Ag core–shell NCs, hollow Au–Ag_2O core–shell MSHs, and Au–Ag_2O yolk-shell MSHs through sequential application of electron beam induced oxidation and in situ heating and quenching. b) Schematics of the transformation of Ag@Au core-shell NCs to Au@Ag_2O core-shell MSHs with a hollow Ag core. Reproduced with permission.[76] Copyright 2014, Royal Society of Chemistry. c) TEM images of Ag_2S-*h*Pd (*h*Pd = hollow Pd domain) heterodimers. Reproduced with permission.[71] Copyright 2015, Royal Society of Chemistry. d) Ag_2S-*h*Pt (*h*Pt = hollow Pt domain) heterodimer MSHs. e) Ag_2S-Au-*h*Pt heterotrimer MSHs. f) Schematic of the formation of Ag_2S-*h*Pt heterodimer and Au-Ag_2S-*h*Pt heterotrimer MSHs starting from the Ag@Pt core-shell NCs. Reproduced with permission.[67c] Copyright 2014, Springer Nature.

gradient.[68] Subsequent reaction of the Ag^+ ions with elemental S fed into the environment led to heterogeneous nucleation and growth of a Ag_2S domain on one side of the surface of the Ag-depleted M shell, ultimately resulting in Ag_2S–*h*M heterodimer MSHs with tunable composition. With minor modification, this synthetic scheme was extended to the preparation of analogous Ag_2Se–*h*Pt heterodimers.[67b] A further leap forward towards increased architectural complexity was made by applying the same chemicalization approach to trimetallic Au@Ag@Pt core-shell-shell NCs as the starting seeding platforms: upon selective etching of the inner Ag shell and successive Ag_2S deposition on the external surface of the outer Pt shell, ternary Ag_2S–*h*(Au-Pt) heterodimer MSHs composed of a Ag_2S domain and of a bimetallic Au-Pt cage-bell section [*h*(Au-Pt)] were obtained.[67a] More recently, Feng et al. succeeded in the preparation of Au-Ag_2S-*h*Pt heterotrimer MSHs by performing site-specific overgrowth of a Au domain on the Ag_2S side of preformed Ag_2S–*h*Pt heterodimer MSHs (Figure 12d–f).[67c]

The chemicalization of core-shell seeds can be performed under conditions inhibiting possible hollowing processes to yield standard core-shell type MSHs with an all-solid interior. Examples of as-developed MSHs are provided in **Figure 13**. In an interesting account, Zhao et al. demonstrated the possibility of controlling the configurational symmetry of metal@semiconductor core-shell MSHs by altering the energetics of interface formation through manipulation of the chemicalization process (Figure 13a).[58] Au@Ag_2X@CdX MSHs with varying concentric (symmetric) to (asymmetric) eccentric arrangements of the core relative to the shell domains (Figure 13b) were synthesized by taking advantage of the misfit strain emerging under thermodynamically controlled growth conditions.[58] As shown earlier, chalcogenization of symmetric Au@Ag core-shell seeds is expected to result in corresponding symmetric Au@Ag_2X core-shell MSHs owing to the higher reactivity of Ag towards the chalcogen (X) source. However, by adjusting the synthesis conditions (such as temperature and reactant concentrations), the lattice structure of the Ag_2X shell could be tailored from amorphous to partially crystalline. The lattice mismatch between the original Au core and the newly formed Ag_2X shell caused the emergence of interfacial strain with an intensity that scaled with the degree of crystallinity of the Ag_2X material. The Ag_2X shell was consequently driven to phase segregate into a spatially separated domain as a means of decreasing the extension of the junction area shared with the Au core and of reducing the amount of volume strain energy accumulated. The process eventually resulted in Au@Ag_2X core-shell or heterodimer-type MSHs featuring tunable degrees of spatial asymmetry. Moreover, cation exchange with Cd(II) resulted in their respective Au/CdX nanostructures having similar morphology.

In another account, Weng et al. have demonstrated the generalized synthesis of non-centrosymmetric hetero-oligomer MSHs with a predesigned arrangement of M and CdX domains (M = Au, Pt and X = S, Se) regardless of the degree of misfit between the respective lattices.[65] The key concept underlying the developed synthetic scheme is the use of a purposely introduced Ag domain serving as a sacrificial reaction intermediate by which the desired heterostructure composition and configuration can be achieved. The synthesis of M-CdX heterodimers can be taken as an example to illustrate the fundamental steps involved in the proposed approach (Figure 13c). First, Ag is grown on a pre-existing M seed to form heterostructures with either M–Ag heterodimer or M@Ag core-shell arrangements;

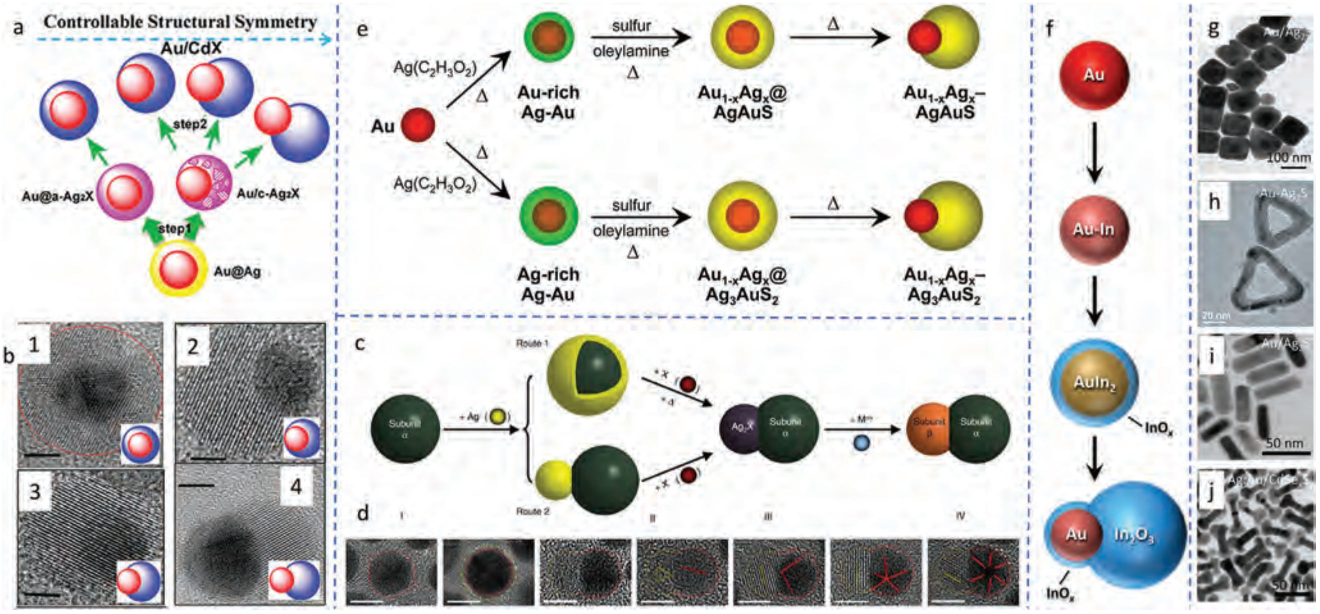

Figure 13. Examples of MSHs with the all-solid interior, synthesized upon chemicalization of bimetallic core-shell seeds. a) A scheme of the pathways leading to Au/CdX (X = S, Se, and Te) MSHs with large lattice mismatch in a synthesis based on two steps of in situ chemical conversion. b) HRTEM images of the as-prepared Au/CdX MSHs characterized by various degrees of symmetry. Reproduced with permission.[58] Copyright 2014, Wiley-VCH. c) Sketch of two synthetic routes to heterodimer MSHs that integrate dissimilar subunits (denoted as *α* and ß, respectively) by using Ag as a common sacrificial reaction intermediate. First, Ag is grown on a pre-existing NC, subunit *α* (stage I), leading to heterostructures with either core–shell (*route 1*) or heterodimeric (*route 2*) configurations (stage II). Subsequently, upon chalcogenization, the heterostructures derived from both *route 1* and *route 2* are converted to intermediate heterodimers carrying an amorphous Ag_2X domain (stage III). Finally, a domain of a desired material, subunit *ß*, can be formed upon the exchange of Ag^+ cations in Ag_2X for other metal ions, M^{n+} (stage IV). d) HR-TEM images of nanoheterostructure intermediates formed in the different stages of the synthesis of Au–CdSe heterodimer MSHs: Au seed subunits (stage I); Au@Ag core–shell NCs (stage II); Au–Ag_2Se heterodimers (stage III); Au–CdSe heterodimers (stage IV). Scale bar of HR-TEM images: 5 nm. In the HR-TEM images, dashed lines outline the boundary of different components. Four different HRTEM images of Au–CdSe heterodimers are presented, highlighting existence of various lattice orientations between Au and CdSe subunits without interfacial lattice match (orange and red solid lines depict the orientations of CdSe and Au lattices, respectively). Reproduced with permission.[65] Copyright 2014, Springer Nature. e) Schematic illustration of the sulfurization process of Ag- and Au-rich AgAu seeds leading to the formation of core-shell and $Au_{1\text{-}x}Ag_X$-AgAuS and $Au_{1\text{-}x}Ag_X$-Ag_3AuS_2 heterodimer MSHs. Reproduced with permission.[63] Copyright 2017, American Chemical Society. f) Schematic of the formation mechanism of Au–In_2O_3 heterodimer MSHs and capturing their evolution during the synthesis course. Reproduced with permission.[70] Copyright 2014, American Chemical Society. g) TEM image of cube-shaped Au@AgCdS core-shell MSHs. Reproduced with permission.[60] Copyright 2013, Optica Publishing group. h) TEM image of Au@Ag_2S core-shell nanoframe MSHs. Reproduced with permission.[85] Copyright 2014, Wiley-VCH]. i) TEM image of rod-shaped Au@Ag_2S core-shell MSHs. Reproduced with permission.[59] Copyright 2006, The Royal Society of Chemistry. j) TEM images of $CdSe_xS_y$-Au-$CdSe_xS_y$ nanodumbbell MSHs with Ag-doped $CdSe_xS_y$ caps. Reproduced with permission.[66] Copyright 2021, American Chemical Society.

subsequently, upon selective chalcogenization of Ag and strain-driven phase segregation, the heterostructures are converted to M–Ag_2X heterodimers carrying an amorphous Ag_2X unit. Finally, the exchange of the Ag^+ cations in Ag_2X for Cd^{2+} cations, which transforms the Ag_2X domain to a CdX domain, leads to M-CdX heterodimers with crystallographically mismatched heterointerfaces. The overall progression can be verified by TEM/HRTEM-based monitoring of the reaction products withdrawn along the synthesis course (see, for example, the evolution of Au-CdSe heterodimers shown in Figure 13d). The synthetic approach to heterodimer MSHs with programmed composition offers a basis to engineer increasingly complex hetero-oligomer MSHs that group multiple domains of diverse functional materials.

The chemicalization of bimetallic core-shell NCs can also be exploited as a route to MSHs with heterodimer configuration. Li et al. showed that sulfurization of Au@Ag NCs leads to the formation of $Au_{1\text{-}x}Ag_XS$@AgAuS or $Au_{1\text{-}x}Ag_XS$@Ag_3AuS_2 core-shell MSHs,[63] depending on the relative fractional amount of Ag in the seeds. Heat treatment of these core-shell MSHs led to the formation of $Au_{1\text{-}x}Ag_X$-AgAuS and $Au_{1\text{-}x}Ag_X$-Ag_3AuS_2 heterodimer MSHs (Figure 13e). Similarly, Gordon et al. fabricated Au-In_2O_3 heterodimer MSHs by slowly introducing In(III) acetate precursor into a solution of Au NC seeds using a syringe pump.[70] It was clarified that the formation of these MSHs proceeded via a multistep pathway: the Au seeds first combined with the In precursor to form alloy Au-In NCs; these were then transformed into $AuIn_2$@InO_x MSHs composed of an intermetallic $AuIn_2$ core surrounded by a shell of amorphous indium oxide, InO_x; finally, Au–In_2O_3 MSHs with heterodimer architecture were obtained upon complete strain-driven phase segregation and crystallization of the oxide shell (Figure 13f).

Several prototypes of structurally more complex core-shell MSHs with anisotropic shape profiles have also been constructed through conformal chemicalization of corresponding shaped bimetallic seeds. For example, Liu et al. prepared

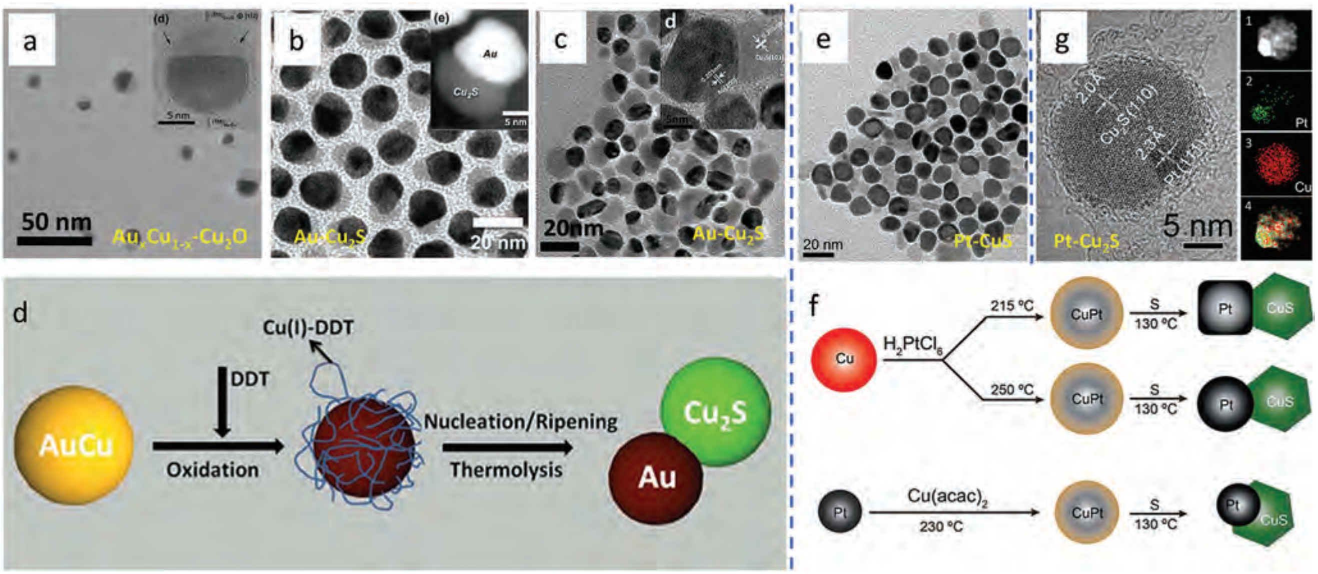

Figure 14. Examples of MSHs synthesized upon chemicalization of bimetallic alloy seeds. a) TEM image of $Au_{0.83}Cu_{0.17}$–Cu_2O Janus-type MSHs (inset is the HRTEM image of an individual heterostructure). Reproduced with permission.[83] Copyright 2008, American Chemical Society. b) TEM image of a Au–Cu_2S heterodimer MSH (inset is a representative dark-field TEM image). Reproduced with permission.[75] Copyright 2012, American Chemical Society. c) TEM image of Au–Cu_2S heterodimer MSHs (inset is a representative HRTEM image) synthesized starting from AuCu alloy NCs and d) sketch of the proposed mechanistic pathway for their formation. Reproduced with permission.[77] Copyright 2012, The Royal Society of Chemistry. e) Pt–CuS heterodimer MSHs derived from Pt-seeded CuPt alloy NC seeds synthesized at 250 °C and f) schematic representation of the reaction pathways underlying the evolution of heterodimers with different degrees of asymmetry. Reproduced with permission.[79] Copyright 2013, The Royal Society of Chemistry. g) HRTEM and corresponding HAADF-STEM and elemental mapping images of Pt-Cu_2S MSHs. Reproduced with permission.[103] Copyright 2014, American Chemical Society.

cube-shaped Ag_2S@Au core-shell MSHs by treating Au@Ag core-shell nanocube seeds with NaHS (Figure 13g).[60] Similarly, Au@Ag_2S nanoframe MSHs were developed by Xu et al. by an approach relying on the sulfurization of Ag-coated Au nanoframes (Figure 13h).[85] Further, Liu et al. synthesized rod-shaped Ag_2S@Au and Ag_2Se@Au core-shell MSHs by exposing Au@Ag core-shell nanorod seeds to Na_2S and selenourea, respectively (Figure 13i).[59] Wang et al. developed a multistep protocol for the preparation of CdSe-Au-CdSe nanodumbbell MSHs.[61] The selenization of Au@Ag core-shell nanorods using Se powder dissolved in an aqueous hydrazine solution led to Ag_2S-Au-Ag_2S nanodumbbell MSHs through a mechanism involving surface diffusion of Ag along the longitudinal sidewalls of the seeds and preferential overgrowth of amorphous Ag_2Se caps at the apexes; subsequent Cd^{2+} for Ag^+ exchange upon reaction with aqueous $Cd(NO_3)_2$ solution in the presence of tributylphosphine (TBP) as complexing agent allowed conversion of the Ag_2S-Au-Ag_2S nanoheterostructures to corresponding CdSe-Au-CdSe nanodumbbell MSHs.[61]

More recently, Wang et al. developed compositionally intricate nanodumbbell MSHs by a modified multistep synthesis sequence.[66] First, Au@Ag nanorod seeds were treated with an aqueous mixture of elemental Se and S with 1,2-ethylenediamine (EDA) to derive selective $AgSe_xS_y$-tipped Au nanorods. Here, the presence of EDA in the chalcogen precursor source was essential to guaranteeing the regioselective formation of a well-defined nanodumbbell architecture in place of the Au@$AgSe_xS_y$ core–shell configuration otherwise expected as the result of isotropic chemicalization of the Ag shell of the nanorod seeds. Then, partial Cd^{2+} for Ag^+ cation exchange at room temperature resulted in the formation of $CdSe_xS_y$-Au-$CdSe_xS_y$ nanodumbbell MSHs, where both the central Au section and the terminal $CdSe_xS_y$ domains contained controlled levels of Ag impurities (Figure 13j).

3.2. Chemicalization of Alloy Seeds

Chemicalization of alloy NCs, composed of one reactive and one inert metal, has been exploited to fabricate core-shell, yolk-shell or Janus-type MSHs. Representative results are displayed in **Figure 14**. Lu et al. have shown the conversion of AuCd alloy NCs into Au@CdSe core-shell MSHs upon treatment with a Se-TOP complex as Se source at elevated temperatures.[81] Similar core-shell Au_2Cd@CdSe MSHs were synthesized by Guardia et al.[74] Interestingly, Zhang et al prepared a tri-metallic core-shell MSH system, Au@$CuInSe_2$.[84] The developed synthetic approach relied on combining preformed Au NCs with a Cu(I) and In(III) salt solution in the presence of oleylamine at 130 °C, then heating the mixture up to 260 °C. It is plausible that, at such higher temperatures, the Cu(I) ions were reduced at a much faster rate than In(III) ions by oleylamine because of their lower electropositivity. This reaction would thus provide Cu atoms available to diffuse into the Au seeds and form a AuCu layer on their surface. Subsequent injection of a Se/oleylamine solution induced dealloying of the AuCu layer on the AuCu-covered Au seeds and selenidation in the presence of In(III) species to yield $CuInSe_2$ on Au domains, hence, core-shell Au@$CuInSe_2$ MSHs. The AuCu alloy was demonstrated to be a reaction intermediate essential to enabling the combination of Au and In; in fact, in the absence of the precursor CuCl salt, only separated Au and $InSe_2$ NCs could be obtained.

Phase-alternated heterodimer and Janus heterostructures have also been synthesized by the chemicalization of alloy NCs. For example, Hong et al. reported the formation of segmented AuAg-Ag_2S nanowires by treatment of AuAg alloy nanowires with elemental S at room temperature.[16j] The authors suggested that atomic diffusion and Ostwald ripening processes drove a morphological-structural change from the starting AuAg nanowire seeds to the final AuAg-Ag_2S heterostructured nanowires. It is known that, in the nanoscale regime, solid-state diffusion of metal atoms into semiconductors to form metal-semiconductor pairs may occur at room temperature if the semiconductor band-gap energy width is narrower than about 2.5 eV. Considering that the band gap is ~0.9 eV for bulk Ag_2S crystal at room temperature and that it could increase to 1.4–2.3 eV for Ag_2S NCs, the aforementioned empirical criterion to predict the onset of atomic diffusion was met under the conditions in which the aforementioned AuAg-Ag_2S segmented nanowires were synthesized. Thus, the formulated hypothesis, according to which the Ag_2S domains, initially nucleated upon chemicalization, diffused and coalesced into larger domains within the AuAg nanowire seed lattice, appears to be reasonable.

Koga et al. synthesized $Au_{0.83}Cu_{0.17}$-Cu_2O Janus-type MSHs with a prolate spheroid shape profile (Figure 14a) via gas-phase high-temperature melting/oxidation of a AuCu alloy.[83] HRTEM analysis of these nanoheterostructures showed that the cubic lattices of the $Au_{0.83}Cu_{0.17}$ and Cu_2O phases were connected via a (110) interface with no crystallographic rotation. The intense strain fields arising from the large lattice mismatch (6.5%) induced deformation in both joint lattices, yet without generating misfit dislocations. Motl et al. carried out the treatment of AuCu alloy NCs with elemental S to afford Au-Cu_2S heterodimer MSHs (Figure 14b), in which Au domain was epitaxially attached to a Cu_2S portion.[75] Though phase segregation was assumed to be the main mechanism underlying the formation of these heterostructures, it appeared also plausible that Cu could be stripped out of the AuCu seeds and form Cu_2S upon reaction with S species approaching the AuCu lattice. To validate this hypothesis, the outcome of the reaction between copper(II) acetate and Au NCs was independently examined under conditions identical to those set in the synthesis of the Au-Cu_2S heterodimers. As only separate Au and Cu_2S NCs were obtained as products, the possible involvement of sequential dissolution/re-precipitation pathways in the formation of the heterodimers should be ruled out. Hence, the Au-Cu_2S heterostructures could safely be regarded as resulting from a genuine phase-segregation process. Ding et al. synthesized a similar type of Au-Cu_2S MHSs (Figure 14c) by treating AuCu alloy with dodecanethiol (DDT) in the presence of oxygen.[77] In the latter case, the transformation process was suggested to follow different mechanistic pathways, namely the initial extrusion of Cu atoms to yield Cu(I)-DDT complexes, and their subsequent thermo-decomposition to Cu_2S over the remaining Cu-depleted Au seeds to form the Au-Cu_2S heterodimers (Figure 14d). As the reaction was carried out under air, Cu atoms in the AuCu alloy seeds could be oxidized and then released as Cu^{2+} ions diffusing outwards into the solution. The DDT present in the liquid environment would reduce the Cu^{2+} ions to form Cu(I)-DDT complexes. Owing to the strong affinity of DDT towards Au, Cu(I)–DDT would tend to be preferentially absorbed onto the Au-rich surface sites of the de-alloying AuCu seeds, decomposing and sustaining Cu_2S nucleation and growth thereon. In this process, the Au-rich AuCu metal seeds acted themselves as powerful heterogeneous catalysts for the pyrolysis of the Cu(I)-DDT complexes, as demonstrated by the fact that heterostructure formation yield decreased drastically if the synthesis was conducted by reacting preformed Cu(I)-DDT complexes and Au NC seeds. An anisotropic deposition of Cu_2S would eventually account for the formation of the Janus-type Au-Cu_2S heterostructures.

Several attempts have been made to understand the influence of various experimental factors, such as the presence of oxygen, the nature of the chemicalization agents, temperature, the composition of the alloy seeds, on the geometry and spatial distribution of the component sections in the final MSHs.

3.2.1. Role of Oxygen

Though atmospheric O_2 is widely used as a chemicalization agent, its role in the transformation of bimetallic alloy NCs to MSHs made of materials other than transition-metal oxides has been elucidated only marginally. Motl et al. have revealed the importance of O_2 in the formation of Au-Cu_2S heterodimer upon sulfidation of AuCu alloy.[75] Ding et al. have carefully investigated the sulfidation reaction of AuCu alloy NCs to produce Au–Cu_2S heterodimer MSHs in the presence and the absence of O_2.[77] Heterodimers formed only if O_2 was admitted to the reaction environment. It was speculated that Cu in the AuCu seeds had to be preliminarily oxidized to Cu^{2+} ions to allow the formation of Cu_2S. O_2 could play the role of the required oxidizing agent, thus accounting for the necessity of its presence in the growth environment to guarantee the high-yield evolution of Au–Cu_2S heterostructures.

3.2.2. Effect of Temperature and Chemicalization Agents

Temperature has been shown to have a significant influence on the chemicalization process. A minimum temperature is needed to trigger the chemicalization process; beyond this threshold, an increase in temperature accelerates the transformation. However, there exists a restricted temperature range in which high-quality MSHs may be obtained, depending on several factors, such as the nature and size of metallic alloy, chemicalization agents etc. For example, on investigating the sulfidation of CuPt alloy NCs to Pt-CuS heterodimer MSHs, Ding et al. verified that both the temperature at which CuPt alloy seeds were synthesized and the temperature at which the chemicalization was carried out played a crucial role in determining the final morphology and yield of heterostructures.[79] While sulfidation of CuPt alloy NCs synthesized at 215 °C resulted in Pt–CuS heterodimers with truncated cube-like Pt domains (Figure 14e), sulfidation of Cu-seeded CuPt alloy NCs synthesized at 250 °C led to Pt–CuS heterodimers with relatively smaller spherical Pt domains (Figure 14f). In both cases, the CuS domain of the MSHs exhibited a plate-like morphology (the evolution of the CuPt seeds to Pt–CuS MSHs in different synthesis conditions is summarized in Figure 14g). It is plausible that the observed evolution of the Pt–CuS heterodimers that exposed Pt domains with different morphologies was determined, in a rather complicated way, by the combined outcomes of atomic diffusion, lattice restructuring and Oswald ripening on the alloy seeds at the distinct temperatures at which their synthesis and post-synthesis transformation were carried out.

The effect of temperature at which chemicalization was accomplished was also investigated in a set of syntheses of Pt–CuS heterodimer MSHs, all of which were seeded with CuPt alloy NCs generated at 215 °C. If the injection temperature of S was kept 90 °C, MSHs with small CuS domains were obtained in low yield. An increase in injection temperature to 190 °C led to the formation of a polydisperse population of MHSs that possessed Pt domains with morphologies varying from cubic to spherical, and CuS domains with irregular sizes over a broad range. At the intermediate temperature of 130 °C, Pt–CuS heterodimer MHSs with uniform geometric features were formed in elevated yield. The optimal temperature at which the highest-quality heterostructures could be derived is likely to correlate, partially at least, with the reactivity of the particular chemicalization agent (S) used in these syntheses.

Not only temperature, but also the type of molecular precursors determines the composition and the morphology of MSHs. For example, Sang et al. reported a facile one-pot synthesis approach for obtaining CuPt–Cu_2S, Pt–Cu_2S heterodimer MSHs, and CuPt nanocubes.[103] Combined HRTEM and HAADF-STEM imaging, and elemental mapping clearly disclosed the heterodimer architecture of the as-developed Pt-Cu_2S MSHs (Figure 14g). While the use of K_2PtCl_4 as Pt-precursor resulted in CuPt nanocubes, under similar reaction conditions, the use of H_2PtCl_6 and $Pt(acac)_2$ led to CuPt–Cu_2S and Pt–Cu_2S MSHs, respectively. 1-Hexadecanethiol (HDT) was utilized in this system to mediate the reduction of metal precursors and to serve as a capping agent and sulfur source. They assumed that the formation of such heterodimer MSHs proceeded through the generation Cu_2S domain, which was most likely induced by the sulfurization of Cu with HDT.

Ding et al. synthesized Au-Cu_2S heterostructures by reacting AuCu NC seeds with different types of chemicalization agents, namely elemental S, 1-DDT (dodecanethiol with linear carbon chain), and t-DDT (a branched tertiary thiol).[77] When 1-DDT was used as a sulfur source, the formation of Au-Cu_2S heterodimers occurred at a higher temperature, 180 °C. When the more reactive t-DDT was used, the temperature required for the formation of Au-Cu_2S heterostructures was slightly lower, 160 °C. With elemental S, which was proven to act not only as a sulfur source, but also as a strong oxidant for the AuCu seeds, MSHs formed at a much lower temperature, 100 °C, even in an inert atmosphere, but their morphologies were irregular. These facts indicated that the metal oxidation was a critical step in the formation of MSHs and that either 1-DDT or t-DDT would represent an optimal sulfur source to generate Au-Cu_2S MSHs. These ligands played two important roles. Firstly, they coordinated with the Cu^{2+} ions, derived from the oxidation of the AuCu seeds, to yield Cu(II)–thiol complexes that facilitated their migration into the solution proximal to the seeds. Second, they acted as reducing agents, leading to the formation of Cu(I)–thiol complexes. The choice of the reducing agents depends on the composition of the alloy seeds. For example, 1-DDT is an ideal chemicalization agent for the synthesis of Au-Cu_2S MSHs starting from AuCu seeds, yet it is not useful for the fabrication of Pt-CuS MHSs from CuPt seeds. The different behavior can be explained, in part at least, on the basis of the higher stability of CuPt alloy NCs, compared to that of their AuCu counterparts.

An interesting study by Shen et al. has demonstrated the temperature dependence of structural change in CuNiS NCs obtained from the sulfurization of CuNi alloy.[80] Sulfurization of $Cu_{0.5}Ni_{0.5}$ NCs at 150, 200, and 250 °C for 30 min, leads to the formation of yolk-shell, double-shell heterostructures, and single-shell (hollow) nanostructures, respectively. It is known that Ni ions diffuse more quickly than Cu ions, which can explain the formation of the yolk-shell architecture with Cu in the core. As the temperature increases, the diffusion rate of Cu ions is enhanced, leading to the formation of double-shell, and single-shell hollow nanostructures. These results clearly indicate that the selection of a proper chemicalization agent and of a suitable temperature is essential to guarantee the production of high-quality heterostructures with programmed architecture.

3.2.3. Size, Shape, and Composition of the Alloy Seeds

Xia et al. have extensively investigated the dependence of the outcome of the oxidation reaction of FeNi alloy NCs on their size and composition. While oxidation of smaller seeds led to the formation of hollow NCs (a few of which had double cavities), larger NCs with inner porous structures were predominantly obtained upon oxidation of larger seeds.[86] With the help of in situ three-dimensional TEM imaging, the authors disclosed the formation of an initial oxide layer composed of both Fe and Ni. The structure of the oxidized product was affected by cracks/voids formed within the oxide shell, the occurrence of which in turn depended on the size and composition of the starting alloy seeds. In general, it was observed that, as the mean seed size decreased and/or the Fe to Ni relative proportions in the starting FeNi alloy seeds increased, the probability of creating a porous structure was reduced. It is useful to recall that, if the rate of outward diffusion of the metal atoms through an oxide layer is significantly slower than the rate of migration of vacancies, then a single void can be expected to form; otherwise, multiple cavities are more likely to be generated.[24] As the oxidation conditions were identical and the diffusion coefficients of the atomic constituents in the seeds depended only on the composition of the alloy, the observed structural change could be safely attributed to differences in diffusion distances. In larger FeNi seeds, before the metal atoms could cover the long distance needed for condensation of all the vacancies into one single void, the outward diffusion of atoms through the oxide layer led to increases in the concentration of vacancies in different locations. This promoted the formation of multiple voids and, hence, the evolution of an overall porous structure. Also, as Fe atoms diffuse faster than Ni atoms, the probability of the formation of porous NCs decreases with increases in the relative Fe to Ni content in the alloy. However, in contrast to the NiFe system, hollow NCs with a single cavity were not the predominant product for the Ni-Co system, where Ni atoms diffuse more slowly, compared to Co atoms.[82]

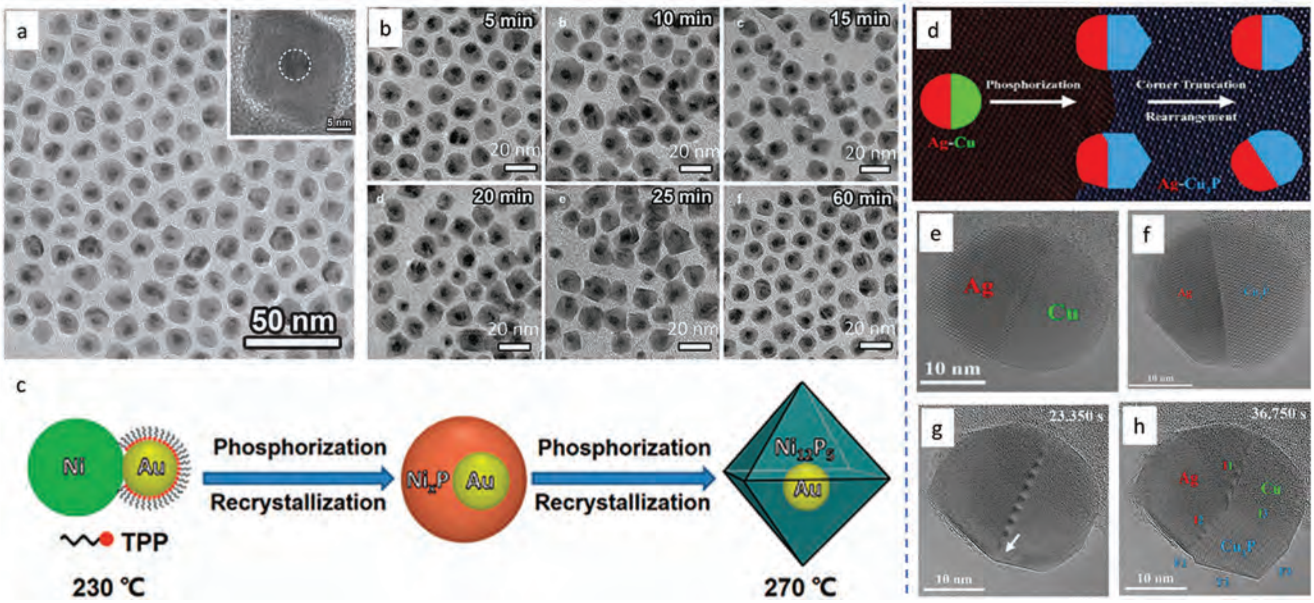

Figure 15. Examples of MSHs synthesized upon chemicalization of heterostructured seeds. a) TEM image of Au@$Ni_{12}P_5$ core-shell MSHs evolved from Au–Ni heterodimer seeds (in the inset: HRTEM image of a single MSH). b) TEM images of reaction products extracted at different reaction times, showing the conversion of the starting Au–Ni heterodimer NCs to the final Au@$Ni_{12}P_5$ core-shell MSHs in the presence of TPP as a chemicalization agent. c) Schematic representation of the formation mechanism of Au@$Ni_{12}P_5$ core-shell MSHs from Au–Ni heterodimers. Reproduced with permission.[95a] Copyright 2014, Nature Publishing Group. d) Schematic representation of the conversion of AgCu alloy NCs seeds to Ag-Cu_3P Janus-type MSHs. e,f) HRTEM images of a Janus Ag-Cu seed and of a Janus Ag-Cu_3P Janus MSHs, respectively. g-h) Selected averaged frames of a HRTEM movie recorded 23.350 s and 36.750 s, respectively, after the supply of PH_3 to the Ag–Cu heterostructure at 350°C: the pictures show nucleation of the Cu_3P phase at the triple-phase boundary, marked by a white arrow in panel g, and the progress of phase transformation, as indicated by the different phases, the heterointerfaces I1–3, and the Cu_3P facets F1–3 marked in panel (h). Reproduced with permission.[96] Copyright 2022, American Chemical Society.

Finally, the possible shape dependence of the oxidation process of alloy seeds, as revealed by Tan et al., deserves mentioning.[87] The authors observed that oxidation of rhombic-dodecahedron bimetallic Pt–Ni alloy NCs resulted in Pt@NiO yolk–shell MHSs, whereas alloyed Pt–Ni NCs tended to “split” into a two-sided Pt-NiO heterodimer-type structures.

3.3. Chemicalization of Bimetallic Heterodimer Seeds

The chemicalization of preformed heterostructured Janus-type NCs composed of distinct metal domains represents an interesting strategy with the potential of increasing further the structural complexity of colloidal MSHs. Yet, because of the inherent challenges posed by its implementation, this paradigm remains far less exploited, compared to transformative routes leveraging on bimetallic core-shell and alloyed seeds. Relevant case studies are illustrated in **Figure 15**. Duan et al. have reported the synthesis of Au@$Ni_{12}P_5$ core-shell MSHs (Figure 15a) by phosphidation of Au-Ni heterodimers with triphenylphosphine (TPP) in oleylamine at high temperature (270 °C).[95a] The evolution of heterostructures was monitored over time to understand the mechanism of the conversion process (Figure 15b). Along the course of the initial incubation with TPP in oleylamine at 230 °C, the seeds underwent a transformation to eccentric Au@Ni_xP core-shell MSHs; subsequently, upon heating up to 270 °C and further phosphidation, the latter converted to corresponding concentric Au@$Ni_{12}P_5$ core-shell MSHs with an octahedron-shaped $Ni_{12}P_5$ shell (Figure 15c). Through systematic investigations, the authors decoupled the roles of temperature and TPP in the formation of the Au@$Ni_{12}P_5$ core-shell MSHs. For a fixed amount of TPP, as long as the reaction was carried out at 230 °C, no significant changes in the morphology of the Janus seeds were appreciated. The fact that the P element was not detectable in the heterostructures suggested that phosphidation of Ni had not taken place to any significant extent. It was therefore concluded that the phosphidation of Ni in the seeds required a temperature higher than 230 °C in order to be induced. Finally, TPP was revealed to be as an essential ingredient for the formation of these MSHs.[95a] Upon replacement of TPP with a different P source, such as TOP, phosphidation of Ni could not be initiated, even at a temperature as high as 320 °C. However, eutectic Au–Ni Janus NCs were obtained. It should be noted that, unlike TPP, TOP lacks unshared electrons on the P atom, which makes it a weaker capping agent for Au compared to TPP. A TOP capping could thus allow the migration of Au atoms at high temperature, thereby enabling the formation of eutectic Au-Ni nanoparticles. Taken together, the observations above confirmed the role of TPP as both a capping agent and a phosphorous source.

Spindly Au-Ni heterodimers were shown to exhibit tunable anisotropic reactivity towards $HAuCl_4$ in toluene solutions containing different surfactants, oleylamine and didodecyldimethylammonium bromide, respectively.[95b] Depending on the type of ligand introduced in the reaction medium, anomalous sequences of selective etching, regeneration, and redissolution of either metal components were observed. These events ultimately resulted in the high-yield formation of unexpected nano(hetero)structures, such as highly asymmetric Au-Ni heterodimers with larger Au domains, Au-NiO heterodimers with hollow NiO domains, and hollow NiO NCs. These outcomes suggested that, in the presence of different ligands that could act as both complexants for metal ions and capping agents for metal NC surfaces, the ranking order of the galvanic potentials associated with the $AuCl_4^-{}_{(aq)}/Au_{(s)}$ and $Ni^{2+}{}_{(aq)}/Ni_{(s)}$ red-ox couples involved in the synthesis could be abnormally modified, leading to unexpectedly tunable reactivity behaviour.

Recently, Seifner et al. have investigated the interface dynamics involved in the formation Ag-Cu_3P heterodimer MSHs upon phosphorization of Ag-Cu Janus seeds with phosphine (PH_3) (Figure 15d). Their study was conducted using an environmental transmission electron microscope (ETEM) with an integrated metal–organic chemical vapor deposition (MOCVD) system.[96] Systematic HRTEM analyses were carried out (Figure 15e–g). While the Ag domain of the Ag-Cu seeds remained inert towards phosphine, selective phosphorization of Cu started at the Ag /Cu interface, leading to the formation of three-phase boundary regions after nucleation of Cu_3P (Figure 15g–h). The replacement of the original Cu section by a Cu_3P domain was accompanied by appreciable morphological changes (corner truncations), eventually leading to Ag-Cu_3P heterodimers with a relatively smoother shape profile.

4. Some Key Properties and Applications

Seeded-growth strategies have opened access to a library of MSHs with varying compositions and structures, each with its own set of unique physical-chemical properties and functionalities that can be applied to develop interesting applications. In the following, the results of representative case studies, all of which pertain to MHSs exclusively derived by chemicalization routes, are addressed through **Figures 16–19**.

4.1. Optoelectronic Properties

Semiconductor-based nanoheterostructures offer unique grounds for generating otherwise inaccessible optoelectronic properties that indeed reflect the as-obtained alignment of the bands of the component materials.[2h,6a,9c,f,104] Depending on the density of states and on the offsets between the band edges, different charge carrier localization regimes can be realized, which result in new and tunable electric and optical responses, with implications for broadening of the application scopes. In particular, the properties of MSHs are governed by a complex interplay between the enhancement of the local excitation field (affected by the presence of the metal component) and the changes in radiative and nonradiative decay rates for the excited electron-hole pairs. Modified spectral

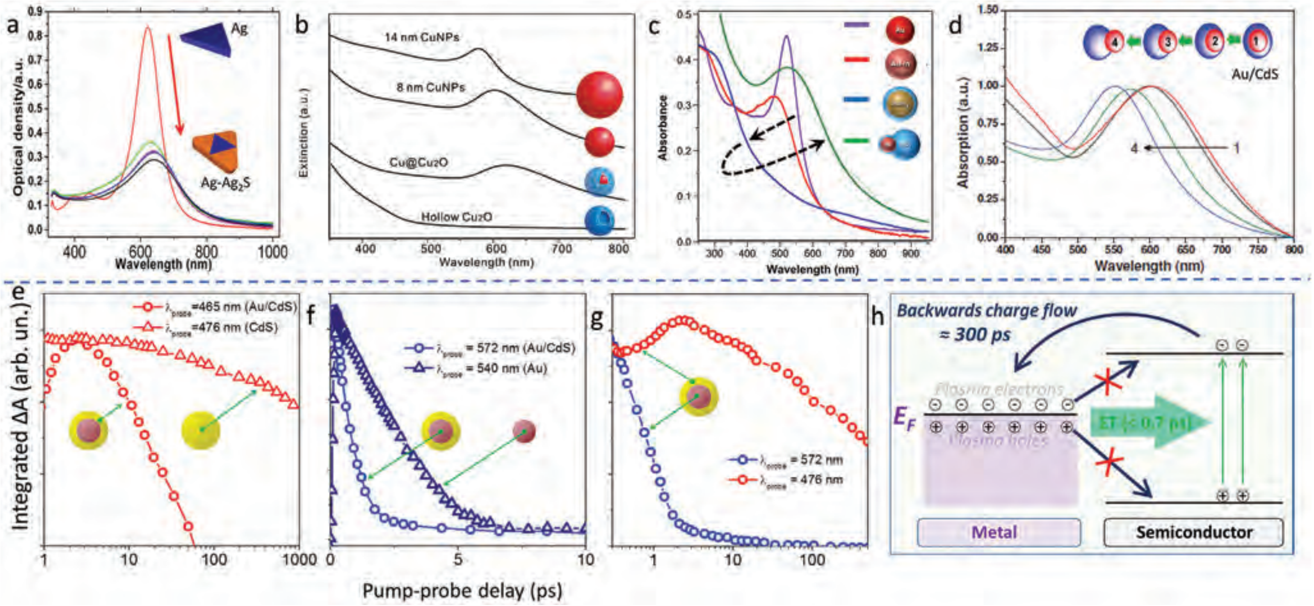

Figure 16. Some optoelectronic properties of chemicalization-derived MSHs. a) Changes in the UV–vis absorption spectra during the sulfidation process of Ag nanoprisms to prism-shaped Ag@Ag_2S core-shell MSHs. Reproduced with permission.[45] Copyright 2016, American Chemical Society. b) UV-vis absorbance spectra of Cu NCs, Cu@Cu_2O core-shell MSHs, and hollow Cu_2O NCs with different geometric parameters. Reproduced with permission.[23] Copyright 2010, Wiley-VCH. c) Evolution of the UV–vis absorption spectrum that occurs during the conversion of Au seed NCs to $AuIn_2$@InO_x core-shell MSHs or Au-In_2O_3 heterodimer MSHs via the formation of Au-In alloy NCs intermediates. The progress of the reaction is shown by a dashed line. Reproduced with permission.[70] Copyright 2014, American Chemical Society. d) Changes in the UV-Vis absorption spectra that accompany the structural evolution of Au/CdS MSHs from a core-shell to a heterodimer configuration. Reproduced with permission.[58] Copyright 2014, Wiley-VCH. Temporal evolution of the recovery of the transient-absorption bleach recorded for: e) the band-edge exciton absorption of CdS ($\lambda \approx 460$–480 nm) in Au@CdS core-shell MSHs (circles) and in CdS NCs (triangles); f) LSPR absorption of Au in Au@CdS MSHs (circles) and in isolated Au NCs (triangles); g) CdS band-edge exciton of CdS (red) and LSPR absorption of Au (blue) in Au@CdS MSHs. h) Proposed diagram of the energy redistribution processes in nonepitaxial Au@CdS MSHs. Reproduced with permission.[102] Copyright 2013, American Chemical Society.

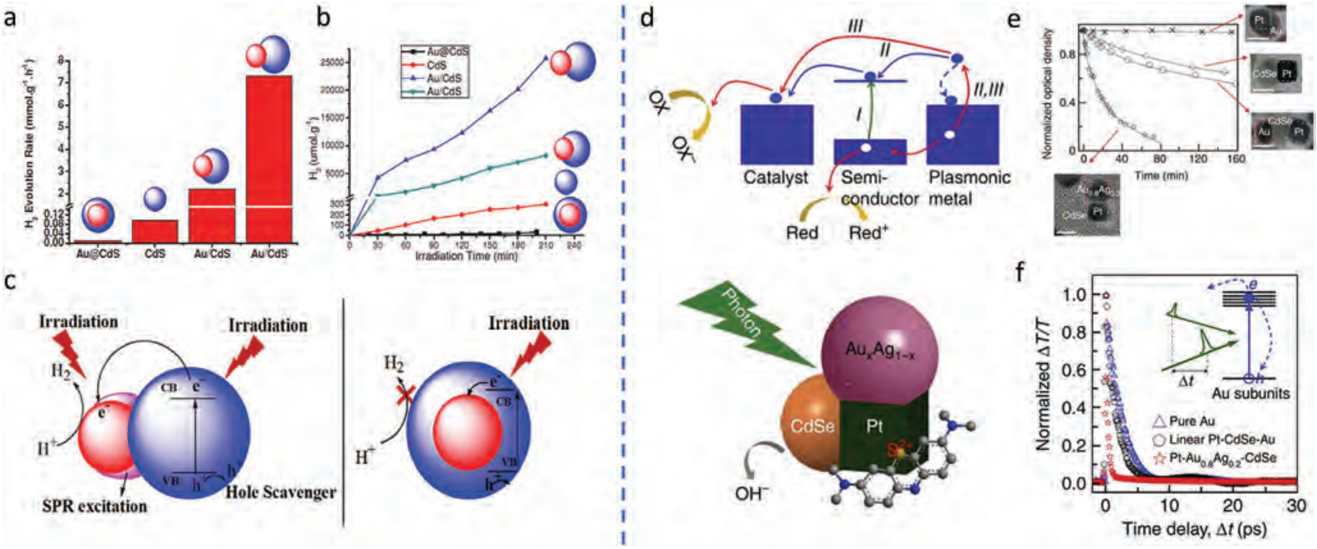

Figure 17. Examples of applications of chemicalization-derived MSHs in heterogeneous photocatalysis. a) Comparison of H_2 evolution activities of various Au-CdS MSHs as photocatalysts. b) Amount of H_2 evolved over different Au-CdS MSH photocatalysts as a function of the irradiation time. c) Schematic of the plasmon-assisted electron-hole separation and transfer process in Au/CdS MSHs with heterodimer and core-shell configuration under visible irradiation. Reproduced with permission.[58] Copyright 2014, Wiely-VCH. d) Band energy diagram showing the conceivable reaction pathways underlying plasmon-assisted photocatalytic reduction of MB molecules over Pt-Au_xAg_{1-x}-CdSe MSHs under visible light illumination. e) Time evolution of the optical density (measured at 677 nm, normalized to the initial value) of an MB solution undergoing photocatalytic reduction over different well-designed photocatalysts: Pt-Au heterodimer MSHs (crosses); Pt-CdSe heterodimer MSHs (diamonds); linear Pt-CdSe-Au MSHs (pentagons); Pt-$Au_{0.80}$Ag0.20-CdSe MSHs (stars). A representative HR-TEM image is provided for each photocatalysts (scale bar, 10 nm). f) Normalized optical transmission change (ΔT/T) as a function of time delay (Δt) in pump–probe measurements, showing occurrence of energy transfer with different scattering interactions inside the Au subunits. The sketch on the left side illustrates the principle of a pump–probe experiment, where the LSPR of Au is excited and the decay of the as-generated hot electrons is recorded. Reproduced with permission.[65] Copyright 2014, Springer Nature.

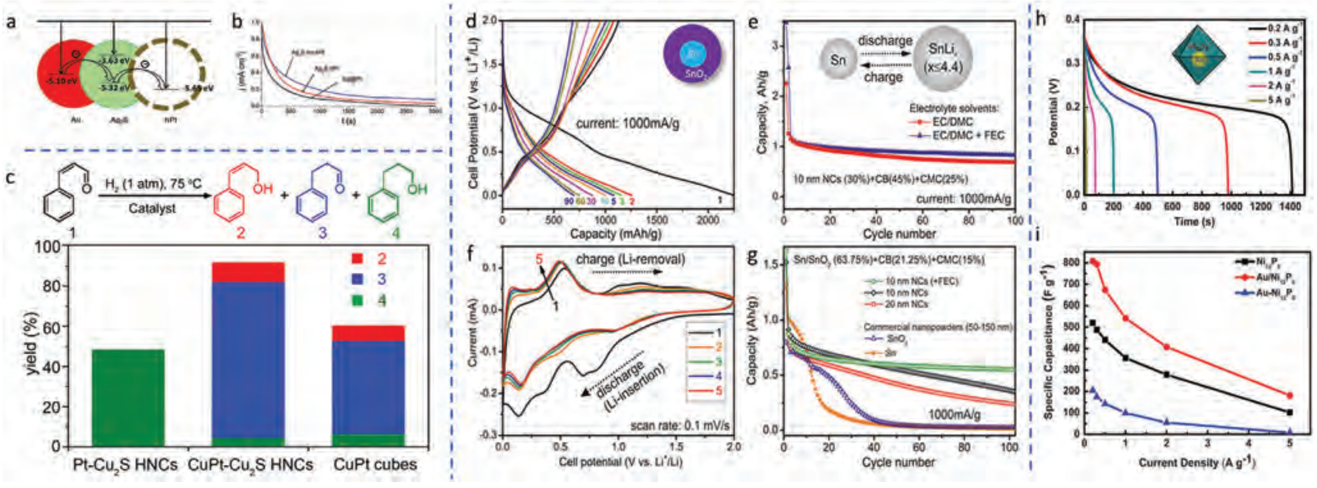

Figure 18. Examples of applications of MSHs in thermal catalysis and energy storage. a) Energy level diagram for the Au-decorated Ag_2S-*h*Pt MSHs illustrating the possible charge-transfer pathways across the nanoheterostructures. b) Chronoamperograms recorded for core-shell Ag@Pt NCs, Ag_2S-*h*Pt heterodimer, and Au-decorated Ag_2S-*h*Pt heterodimer MSHs at 0.45 V versus Ag/AgCl at room temperature in argon-purged $HClO_4$ (0.1 M) with 1 M methanol. Reproduced with permission.[67c] Copyright 2014, Nature Publishing Group]. c) Hystogram of product yields in the reduction of cinnamaldehyde with H_2 using CuPt alloy nanocubes, CuPt–Cu_2S MSHs, and Pt–Cu_2S MHSs as heterogeneous catalysts. Reproduced with permission.[103] Copyright 2014, American Chemical Society. d) Galvanostatic discharge profiles for anode electrodes containing 10 nm Sn@SnO_2 MSHs. e) Cyclic voltammograms (CVs) for the initial five charge–discharge cycles at a scan rate of 0.1 V/s for 10 nm Sn@SnO_2 MSHs. f-g) Reversible discharge capacities (normalized by the content of the active material) for anodes containing 30 wt % Sn@SnO_2 MSHs and a high mass content (63.75%) of an active Sn-based material (NCs or commercial powders), respectively. Reproduced with permission.[26] Copyright 2013, American Chemical Society. h) Discharge voltage profiles for $Ni_{12}P_5$ NCs, Au@$Ni_{12}P_5$ core-shell MSHs and Au–$Ni_{12}P_5$ heterodimer MSHs at different current densities. i) Comparison of specific capacitances for $Ni_{12}P_5$ NCs, Au@$Ni_{12}P_5$ core-shell MSHs and Au–$Ni_{12}P_5$ heterodimer MSHs. Reproduced with permission.[95a] Copyright 2014, Nature Publishing Group.

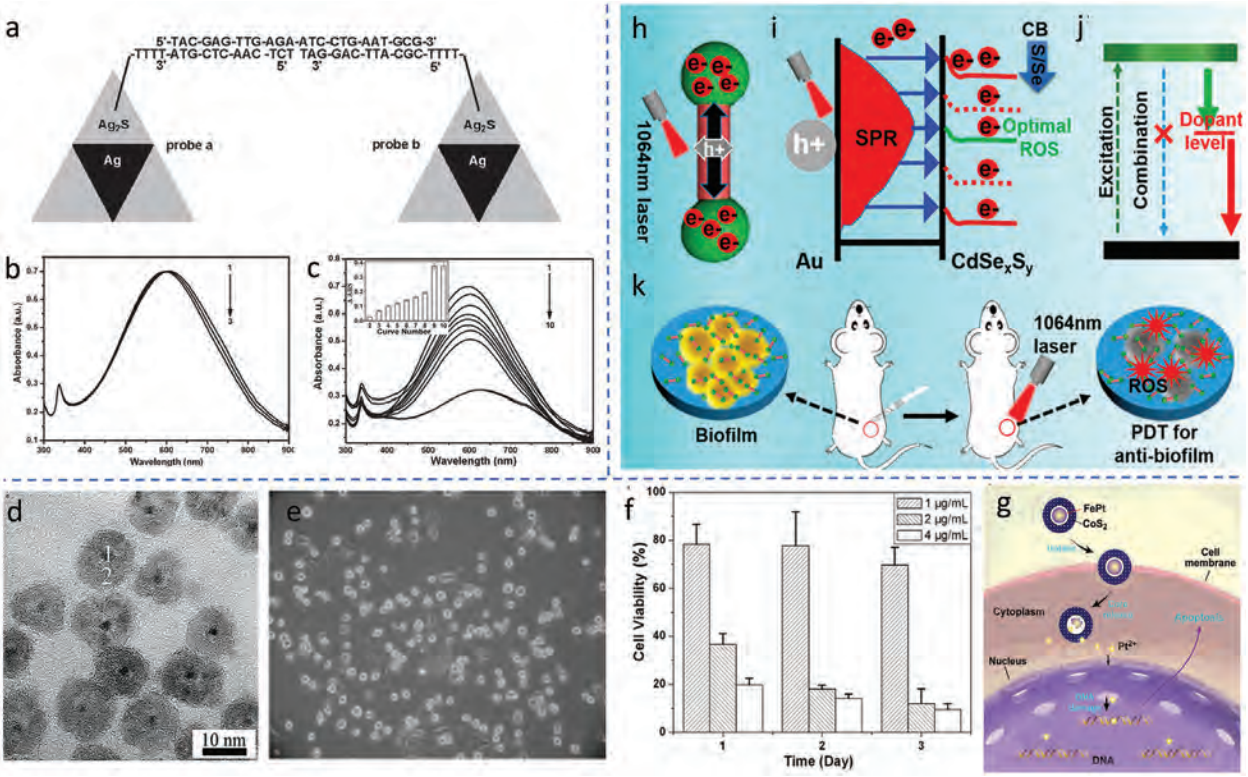

Figure 19. Examples of applications of MSHs for biomedicine. a) Scheme of hybridization reaction by which oligonucleotide-functionalized Ag_2S–Ag nanoprism MSHs may form aggregates in the presence of a complementary oligonucleotide strand. b) UV–Vis absorption spectra of Ag_2S–Ag MSHs in phosphate-buffered saline solution (curve 1), in the presence of probe DNA (curve 2), and in the presence of probe DNA and non-complementary DNA (curve 3). c) UV–vis absorption spectra of Ag_2S–Ag nanoprobe complexes: the mixture of Ag_2S–Ag MSHs/probe *a* and Ag_2S–Ag MSHs/probe *b* before (curve 1) and after the addition of a complementary target DNA strand at varying concentrations (curves 2–10): 1×10^{-4}, 1×10^{-3}, 0.01, 0.1, 0.5, 1.5, 4, 6, and 10 nM, respectively (the inset shows the plot of the absorption intensity change measured at 600 nm of curves 2–10 against curve 1. Reproduced with permission.[44] Copyright 2011, Wiley-VCH. d) HRTEM images of FePt@CoS_2 yolk-shell MSHs. e) Optical microscopy images of HeLa cells incubated for 72 h with 5 µg/mL of FePt@CoS_2 nanocrystals. f) Results of MTT assay of FePt@CoS_2 yolk-shell MSHs on HeLa cells at concentrations of 1.0, 2.0, and 4.0 µg/mL, respectively. g) Illustration of a possible mechanism accounting for FePt@CoS_2 yolk-shell MSHs killing HeLa cell. Reproduced with permission.[100] Copyright 2007, American Chemical Society. Schematic illustration of the mechanisms enabling enhanced PDT action by Ag-doped $CdSe_xS_y$-Au-$CdSe_xS_y$ nanodumbbell MSHs under NIR-II light by the following means: h) under NIR-II light-driven excitation of the LSPR of Au, phogenerated charge carriers are separated, as hot electrons transfer to the $CdSe_xS_y$ at both ends of the heterostructure, while the hot holes reside in the middle Au nanorod section; i) by tuning the ratio of Se and S in the $CdSe_xS_y$ domains, hence, the position of their conduction-band edges hot-electrons injection into $CdSe_xS_y$ can be made more efficient; j) the introduction of Ag dopant levels into the forbidden energy gap of $CdSe_xS_y$ allowed alternative decay pathways for the photoexcited electrons, thus depressing the probability of their nonradiative recombination with hot holes. k) Schematic illustration of the in vivo exploitation of the NIR-II light-driven PDT capabilities of the Ag-doped $CdSe_xS_y$-Au-$CdSe_xS_y$ for anti-biofilm inhibition. Reproduced with permission.[66] Copyright 2021, American Chemical Society.

signatures of excitons, either quenching or enhancement of the photoluminescence, and nonlinear optical responses may be achieved, depending on semiconductor-to-metal electron transfer and plasmon-exciton coupling mechanisms that are affected by a number of parameters. Relevant optoelectronic properties of chemicalization-derived MSHs are illustrated in the next paragraphs on the basis of the representative data collected in Figure 16.

The capability of supporting LSPRs, a unique property of colloidal NCs of many coinage metals and heavily doped semiconductors,[4c,5b,105] is safely retained and exploitable in MSHs that incorporate such materials. LSPRs can be shaped and/or tuned, or by adjusting the compositions, crystal structure, and geometric of the plasmonic components, on one side, and by adjusting the structure, orientation, and extension of the interface. For example, Shahjamali et al. investigated the plasmonic behavior of MSHs consisting of prismatic Ag@Ag_2S core-shell MSHs, in which an Ag_2S shell had developed non-conformal to the Ag core underneath upon sulfidation of Ag nanoprism seeds.[106] The formation of Ag_2S was accompanied by a decrease in optical density and by either a red-shift or a blue shift of the LSPR absorption of the original Ag seeds (Figure 16a). These spectral changes were consistent with the anisotropic evolution of the Ag_2S shell, which had grown thicker at the corners than along the (111) facets of the Ag seeds at the expense of their lattice.[45] Similar to Ag NCs, Cu NCs can also exhibit size- and shape-dependent LSPR absorptions in the visible range (Figure 16b).[23] The LSPR absorption of Cu was centered at 600 nm in 8 nm diameter NCs, but it was blue-shifted to 578 nm when NC size increased to 14 nm. Interestingly, LSPR absorption intensity decreased significantly in Cu@Cu_2O core-shell NCs and became exceedingly broadened in hollow Cu_2O NCs due to the oxidation of Cu.

The change in the plasmonic response of the Au-based seeds was also analyzed by Gordon et al. during the evolution of the Au-In_2O_3 heterodimer MSHs (Figure 16c).[70] Initially, the starting oleylamine-capped Au seeds exhibited a single LSPR at 520 nm, as expected for isotropic-shaped NCs. During the alloying of Au with In, a significant broadening of the LSPR and a blue-shift to 486 nm were observed due to increased electron density in the Au_xIn_y NCs upon changes in their composition (similar to what was observed for the AuCd case).[74] Upon further introduction of In and the formation of $AuIn_2$@InO_x core-shell intermediates, the Au plasmon resonance blue-shifted into the UV regions. Such behavior was consistent with the higher Drude plasma frequency of In (12.8 eV), compared with that of Au (8.9 eV). In the final isolated Au-In_2O_3 heterodimer MSHs, the LSPR of the Au was found to have red-shifted back to 528 nm, likely as result of the combined effects of i) the dealloying of In from the Au during the formation of the In_2O_3 domain (this would cause the LSPR band to shift back toward that of Au), and ii) the increased dielectric screening arising from the embedding In_2O_3 matrix.

Other interesting observations were reported by Zhu et al. who developed Au@Ag_2S core-shell nanorod MSHs with internal voids.[62] These heterostructures exhibited geometry and composition tunable optical properties due to integrated absorption by the Au core and the Ag_2S shell, further affected by the presence of voids. In the first synthesis step, when Ag was deposited on the surface of Au nanorod seeds, the LSPR absorption of Au blue-shifted. In the successive step, when Ag was converted to Ag_2S, the LSPR absorption shifted to higher wavenumbers. The LSPR absorption of the Au component of the MSHs could easily be adjusted the thickness of the semiconductor shell. Furthermore, the voids located between the Au core and the Ag_2S shell endowed the MSHs with further tunable LSPR properties.

Zhao et al. found that the LSPR absorption band of Au in core-shell and heterodimer Au/CdS MHSs was significantly broadened in the visible range (500–700 nm) because of the plasmon-exciton coupling.[58] A clear tendency towards a blue shift of the LSPR feature accompanied the structural transition of the Au/CdS MSHs from a symmetric core-shell, to an eccentric core-shell and, finally, to an asymmetric heterodimer configuration due to the modulating effects of dielectric environment provided by the differently shaped CdS section connected to the Au domain (Figure 16d).

The effect of plasmons on the energy transfer between metal and semiconductor components was further investigated by Lambright et al. in Au@CdS core-shell type MSHs synthesized by a multistep cation-exchange route.[102] The ability of metal nanoparticles to capture light through LSPR excitations provides an opportunity for enhancing the optical absorption of plasmon-coupled semiconductor materials via energy transfer. However, for this process to occur, the semiconductor component should be electrically insulated to prevent a "backward" charge flow into metal and interfacial states, which causes a premature dissociation of excitons. The authors demonstrated that such an energy exchange can be achieved on the nanoscale by using nonepitaxial Au@CdS core-shell MSHs featured by a low density of interfacial defects. From the ultrafast transient-absorption measurements (Figure 16e-g), it was confirmed that the lifetime of excitons in the CdS shell of the as-developed Au@CdS MSHs is much longer than the lifetimes of excitons in conventional, reduction-grown Au@CdS heteronanostructures. As a result, the LSPR energy of the photoexcited metal domains in the MSHs can be efficiently utilized by the semiconductor component without undergoing significant nonradiative energy losses, a desirable property for catalytic or photovoltaic applications. The reduced rate of exciton dissociation in the CdS domain of Au@CdS nanocomposites was attributed to the nonepitaxial nature of Au/CdS interfaces, affected by a limited occurrence of trap states and characterized by a high potential barrier of the interstitial phase. The direct transfer of excited electrons from the Au domains into the CdS shell was intrinsically inefficient due to the low-energy character of plasma oscillations in metals, a condition that also contributed to reducing the rate of the otherwise energetically allowed CdS-to-Au charge transfer (Figure 16h).

4.2. Applications in Heterogeneous Photocatalysis

Standard heterogeneous photocatalytic systems rely on nanostructures to harness light and utilize it for the generation of electron–hole pairs. If the photoexcited charge carriers escape recombination and are spatially separated, they may reach catalytically active sites at the surface where they can perform red-ox reactions with adsorbed or proximal molecules, or other nanostructures. Among nanomaterials, colloidal semiconductor NCs have successfully exploited as photocatalysts in a variety of reactions in the gas and liquid phases for diverse purposes, spanning from pollutant and bacteria degradation, H_2 generation by water splitting, to CO_2 reduction, and selective synthesis of industrially relevant chemicals and fuel molecules.[11e,106] NC-based photocatalysts yet suffer from relatively low conversion efficiencies due to several intrinsic limitations, including small absorption coefficients, rapid defect-induced carrier recombination, and short carrier diffusion lengths.

Several prototypes of rationally designed nanoheterostructures have been demonstrated to be exploitable as more powerful photocatalytic platforms than their single-material NC components or physical mixtures. In MSHs, in particular, the probability of separation of the photogenerated electron-hole pairs can be significantly enhanced at the interface between the metal and the semiconductor components, and the charge-carrier diffusion distances may generally be increased, ultimately allowing superior energy conversion efficiencies than those achievable by semiconductor NCs alone.[11a–d,f–h,107] More recently, further opportunities for boosting the efficiency of photocatalytic reactions have been considered to be offered by MSHs that incorporate plasmonic components on account of a number of potential plasmon-enhancement mechanisms.[5d,10s,108] Representative case studies are summarized in Figure 17.

Several Au-CdS MSHs have been investigated. MSHs with heterodimer-type architecture were found to exhibit higher efficiency as heterogeneous photocatalysts for the H_2 evolution due to LSPR-enhanced separation of the photogenerated electron-hole pairs and rapid electron transfer to the solution species (Figure 17a–c).[58] By contrast, almost no H_2 evolution was observed on the concentric Au@CdS core-shell MSHs, where the electrons are in fact stored on the Au core after photo-excitation and charge separation, and cannot participate in the photocatalytic reaction.

Weng et al. studied plasmon-mediated photocatalysis on ternary Pt-Au_xAg_{1-x}-CdSe heterotrimer MSHs, where CdSe and Au_xAg_{1-x} served as the semiconductor and plasmonic component, respectively, and Pt served as a co-catalyst for electron transfer into the solution.[65] Over these MSHs, in which all components were partially in contact with one another, the authors found significantly high (~14.8-fold) enhancement of photocatalytic efficiency at visible frequencies, with a dependence on the excitation light wavelength that correlated with the LSPR absorption profile of the MSHs. In order to elucidate the role of the plasmonic subunit in the photocatalytic process and the underlying enhancement mechanism of photocatalysis, the authors considered the possible operation of three different charge-transfer pathways in the visible-light-driven photocatalytic reduction of a model dye, Methylene Blue (MB), over the as-developed Pt-Au_xAg_{1-x}-CdSe nanoheterostructures in the presence of ethanol as sacrificial hole scavenger (Figure 17d).

One plausible mechanism (path I in Figure 17d) could involve direct exciton generation and dissociation in the semiconductor subunit, followed by transfer of the as-separated electrons and holes to the Pt co-catalyst and to the ethanol molecules in solution, respectively. In this context, photon absorption by the semiconductor could be expected to be enhanced by the proximal plasmonic domain via near-field electromagnetic coupling.[5d,10s,108] However, theoretical calculations suggested that such non-radiative energy transfer from the LSPRs excited in the plasmonic Au_xAg_{1-x} subunit to the semiconductor CdSe (path I in Figure 17d) could only account for a maximum ~1.25-fold enhancement (when compared with their Au_xAg_{1-x}-free Pt-CdSe heterodimer counterparts), which is quite far from the photocatalytic yield limit approached experimentally over the Pt-$Au_{0.8}Ag_{0.2}$-CdSe MSHs. Furthermore, such an enhancement mechanism disagreed with the observed frequency dependence of the photocatalytic rates.

In addition to the near-field electromagnetic enhancement effect, alternative photocatalytic reaction pathways could originate from the excitation of the LSPRs in the plasmonic metal subunits. The LSPRs can quickly decay into hot electron carriers capable of crossing high energy barriers before thermal equilibrium is approached. After hot carriers are generated, two transfer sequences could occur: either available conduction states of the semiconductor CdSe domain could bridge the transfer of the hot electrons from the plasmonic Au_xAg_{1-x} to the catalytic Pt subunit (path II in Figure 17d), or the hot electrons could directly translocate from $Au_xAg_{1-}$to Pt (path III in Figure 17d). In both cases, the semiconductor domain is required to mediate the migration of holes to their molecular scavengers in the solution. To discriminate between the two mechanisms highlighted above, the authors performed a series of control photocatalytic reactions over Pt-Au_xAg_{1-x}-CdSe MSHs that had been constructed with different geometric arrangements of their component sections (Figure 17e). The outcome of the experiments clarified that all functional subunits should be, at least partially, in intimate contact with each other in order to synergistically guarantee the high level of performance experimentally ascertained. In fact, linearly arranged Pt-CdSe-Au MSHs with separate plasmonic Au and the Pt co-catalyst domains exhibited rather low photocatalytic efficiency. At the same time, the lack of photocatalytic response from Pt-Au heterodimers indicated that the possibility that charge carriers could be produced and separated to a substantial extent in the absence of the semiconductor component should safely be ruled out. Taken together, these facts allowed drawing the conclusion that the main mechanism underlying the photocatalytic action of the Pt-Au_xAg_{1-x}-CdSe MSHs leveraged on plasmon-driven hot electron migration from the photoexcited plasmonic subunit to the Pt co-catalyst (path III in Figure 17d). The hot-electron transfer was further experimentally confirmed by ultrafast time-resolved optical spectroscopy measurements under photocatalytic conditions on three control samples with finely tailored structural configurations (Figure 17f). Interestingly, the significant reduction of the characteristic constant for hot-electron decay in the Pt-$Au_{0.8}Ag_{0.2}$-CdSe MSHs (where the metallic and co-catalyst subunits share direct interfaces), compared to pure Au NCs and linear Pt-CdSe-Au MSHs, suggested the hot electron transfer in the Pt-$Au_{0.8}Ag_{0.2}$-CdSe nanoheterostructures occurred mainly between Pt and Au subunits, facilitated by a low interfacial energy barrier.

In a more recent study, Wang et al. explored the photoelectrochemical (PEC) capabilities of anisotropic plasmonic-semiconductor CdSe-Au-CdSe MSHs for H_2 generation under irradiation at wavelengths beyond the visible region ($\lambda > 700$ nm).[61] The nanodumbbell architecture of the developed MSHs facilitated exploitation of hot charge carriers generated upon excitation of the LSPR of Au, promoting their spatial separation and re-destination to distinct regions of the nanoheterostructures where they could independently participate in red-ox reactions: the hot electrons, injected into the terminal CdSe domains, could perform reduction processes at their surfaces, whereas the hot holes, concentrated along the rod-like Au domain, could drive oxidative processes thereon. Owing to these properties, the CdSe-Au-CdSe nanodumbbells demonstrated PEC activity for H_2 generation which was ~ 4 times than that achievable with their Au-nanorod@CdSe core-shell counterparts.[61] In the latter nanoheterostructure, the Au surfaces were not directly accessible to solution species; consequently plasmon-driven hot holes could not be efficiently separated from hot electrons and transferred outwards to oxidize solution species.

4.3. Applications in Heterogeneous Thermal Catalysis

Inorganic nanostructures that feature controlled structural and geometric parameters and expose a rich fraction of their constituent atoms on tailored surface facets offer immense technological opportunities as heterogenous catalysts for a variety of thermally activated, industrially relevant chemical reactions. Suitably designed NC-based catalytic systems allow lowering the energy barriers that govern the kinetics of the transformation of reactants adsorbed on their surface.[4e,109] In this realm, MSHs represents refined prototypes of supported metal catalysts, where both components have nanometer-scale dimensions and the semiconductor serves as both stabilizing and activating substrate for the metal.[4e,110]

MSHs synthesized by chemicalization routes have been explored in thermal catalysis. Interesting case studies are highlighted in Figure 18a–c. For example, the ternary Au-decorated Ag_2S/*h*Pt (where *h*Pt = hollow Pt domain) heterodimer MSHs were found to exhibit higher catalytic activity towards methanol oxidation reaction (MOR), compared to their individual nanoscale constituents, binary Ag_2S-*h*Pt heterodimers and core-shell Ag@Pt NCs.[67c] From the analysis of the electrochemically active surface areas (ECSAs) by X-ray photoelectron spectroscopy (XPS) of core-shell Ag@Pt NCs, and the different MSHs, the authors observed that Pt in Ag@Pt core-shell NCs featured higher binding energy than in the Ag_2S-*h*Pt and the Au-decorated Ag_2S-*h*Pt heterodimers. This was interpreted as the signature of achieved electron transfer to the Pt domain from the other components of the MSHs under thermodynamic equilibrium. In particular, a comparative analysis of the Pt signal in the XPS spectra of the binary and ternary heterodimers revealed that the Au domain should be the promoter of the detected electron-donating effect. On the basis of the experimental analyses, a plausible energy diagram was drawn, where the band edges of the component materials in the MSHs are appropriately staggered relative to each other so as to account for intraparticle charge transfer (Figure 18a). According to the proposed energetics, allowed charge transfer from Ag_2S to Pt both in the binary Ag_2S-*h*Pt and in the ternary Au-decorated Ag_2S-*h*Pt heterodimers could be expected to lead to a substantial increase in the electron density around the Pt domain, where chemisorption of CO, a key intermediate species resulting from early methanol oxidation, would consequently be weakened. This condition could be considered to be favorable to the promotion of the MOR over the ternary Au-decorated Ag_2S-*h*Pt heterodimers with respect to binary Ag_2S-*h*Pt heterodimers and Ag@Pt core-shell NCs (Figure 18b). In line with these findings, *Ding* et al. found that the Pt–CuS heterodimer MSHs synthesized via sulfidation of CuPt alloy seeds behaved as efficient catalysts for the MOR at room temperature due to the beneficial effect of the strong electronic coupling between the component material domains in the heterodimers.[79]

MSHs have been explored also as thermal catalysts for various hydrogenation reactions. For example, Sang et al. investigated the hydrogenation of cinnamaldehyde over CuPt nanocubes, CuPt–Cu_2S, and Pt–Cu_2S MSHs synthesized by the same one-pot route using different Pt precursors.[103] Results showed that CuPt–Cu_2S MSHs enabled the highest conversion rate and the highest selectivity for the formation of hydrocinnamaldehyde, while 3-phenyl-1-propanol was the only product formed over Pt–Cu_2S MSHs (Figure 18c). The higher selectivity for the evolution of the hydrocinnamaldehyde product CuPt–Cu_2S HNCs was tentatively explained as a manifestation of enhanced chemoselectivity in the reduction of olefinic group over the CuPt domain, allowed by synergistic interaction between Cu and Pt elements, and by interfacial charge transfer induced by the adjacent Cu_2S domain.

4.4. Applications in Energy Storage

Materials possessing the ability to intercalate and store large quantities of foreign ions are potentially suitable for rechargeable electrochemical energy storage technologies; yet, high electronic or ionic conductivity, fast reaction kinetics, and tolerance to minor structural changes induced by intercalation are additional prerequisites for their exploitation in the construction of the device. The use of host materials, with nanoscale dimensions, such as NCs, offers several advantages, including a significant reduction of the path length for mass and charge transport, easier accommodation of the volumetric changes occurring during electrode operation, enhancement of surface-related phenomena (e.g., modified electrochemical potential), and efficient interfacing with other components or surface coating. On the other hand, possible drawbacks are represented by excessive consumption of electrolytes and possible enhancement of reactions of electrode materials.[111]

MSHs obtained by chemicalization were employed as active materials for Li-ion batteries and supercapacitors. Selected results are shown in Figure 18d–i. Kravchyk et al. showed that monodisperse Sn@SnO_2 core-shell MSHs performed better than both commercial Sn and SnO_2 nanopowders when used as active materials to fabricate anodes electrodes (using carbon black as matrix, sodium carboxymethylcellulose as binder, and fluoroethylenecarbonate as electrolyte additive) for Li-ion batteries.[26] Starting from Sn@SnO_2 cores-shell MSHs with mean sizes ranging from 9 to 23 nm and size variance of less than 10%, the authors exploited a simple ligand-exchange technique to equip the originally oleate-coated MSHs with small inorganic surface anions (HS^-, S^{2-}, SO_4^{2-}). The newly implanted capping agents allowed for enhanced interfacial charge transport and improved charging/discharge capacities when the MSHs were used as active charge-storage hosts in battery anodes. The SnO_2 shell in individual MSHs contributed to alleviate mechanical damages induced by phase and volume changes, as well as the tendency towards sintering, which led to electrode pulverization during the lithiation process. Electrochemical measurements (Figure 18d–g) demonstrated that Sn@SnO_2 MSHs exhibited reversible Li^+ insertion/removal cycling capabilities, with capacities close to the theoretically expected values. Furthermore, under a high mass load of the active material, the smallest tested MSHs exhibited much higher charge/discharge cycling stabilities than commercial nano-powders with large sizes (50–150 nm).

A comparative study of the charge-storage properties of the Au/$Ni_{12}P_5$ MSHs with different geometries, reported by Duan et al., deserves to be highlighted.[95a] Carbon-black electrodes containing Au@$Ni_{12}P_5$ core-shell MSHs behaved as far better supercapacitors than electrodes constructed with their Au-$Ni_{12}P_5$ heterodimer counterparts (Figure 18h–i). The higher specific capacitance and higher cycling stability of the core-shell MSHs correlated with an extremely low charge-transfer resistance. This property was safely regarded as originating from the enhanced electric conductivity and/or short diffusion lengths for the ions (electrolytes) synergistically allowed by the core and the shell domains, although beneficial effects of interfacial electronic coupling and/or of spin-orbit coupling at the nanoscale could not be excluded. In the MSHs with core-shell configuration, the thin monocrystalline $Ni_{12}P_5$ shell facilitated ion diffusion and electron transport, while the Au core contributed to alleviate the charge-transfer resistance to some extent. As opposed, in the MSHs with heterodimer arrangement, the Au domain could also foster charge transport from the $Ni_{12}P_5$ component to the electrolytes, inevitably leading to an undesired loss of charge density and stability. In addition, due to their larger surface area and high specific surface energy, the distribution of the heterodimers within the electrode matrix was quite inhomogeneous. As only a limited fraction of the nanoheterostructure population was allowed to fully interact with the carbon additive and store electrons, the specific capacitance ultimately achievable was quite low.

4.5. Biomedical Applications

Colloidal nanoheterostructures exhibit multiple nonhomologous properties and capabilities that are attractive to develop tools and processes of relevance to biomedicine, a field where multifunctionality is indeed highly needed. Nanoheterostructures with suitable architectures and compositions have successfully been used for diagnostic purposes (e.g., multimodal optical and/or magnetic resonance imaging), for therapeutic actions (e.g., by magnetic hyperthermia or photothermal therapies), and for theranostics in the fight against cancers.[6a,112]

There have been reports on the exploitation of chemicalization-derived MSHs for biomedical applications. Relevant achievements are illustrated in Figure 19. Liu et al. investigated the process of formation of pairs of Ag_2S-Ag nanoprism MSHs in a solution, driven by the spontaneous hybridization of DNA strands.[44] To promote coupling, the Ag_2S–Ag nanoprism MSHs were bio-conjugated at their Ag_2S domains with different S-terminated oligonucleotides by means of suitable coupling agents (Figure 19a). As demonstrated by the detection of no changes in the corresponding UV–vis absorption spectrum, nanoprobes consisting of different oligonucleotide-functionalized Ag_2S-Ag MSHs did not cluster in their solutions or upon mixing with noncomplementary DNA strands. Conversely, a systematic decrease in absorbance was detected after mixing oligonucleotide-functionalized Ag_2S-Ag MSHs with a target complementary DNA strand. Such optical change reflected the progressive complexation of the MSHs into large aggregates upon a specific DNA hybridization reaction (Figure 19b). The low detection limit with which the generation of the DNA-MSH clusters could be revealed (Figure 19c), suggested that the as-developed bioconjugated Ag_2S–Ag MSHs could serve as sensitive DNA hybridization probes exploitable for biosensing purposes.

In another account, the FePt@CoS_2 yolk-shell MSHs developed by Gao et al. (Figure 19d) were demonstrated to serve as a potential agent for killing model cancer cells, HeLa.[100] After prolonged incubation with the MSHs, all of the HeLa cells were found to have died (Figure 19e), indicating the significant cytotoxicity of FePt@CoS_2 MSHs, about seven times higher than that of the known cisplatin, taken as reference. Quantitative evaluation by the MTT assay over a range of doses of FePt@CoS_2 MSHs (Figure 19f) demonstrated values of their IC_{50} (the concentration of drug required to inhibit cell growth by 50%, compared to the control) much lower than that of cisplatin. This result was significant because almost none of the Pt-based complexes developed for clinical trials in the past decades had shown higher activity than that of the parent drug, that is, cisplatin. Finally, the authors proposed a mechanism accounting for the cytotoxicity of FePt@CoS_2 yolk-shell MSHs against the HeLa cells (Figure 19g). After cellular uptake, FePt was oxidized, releasing Fe^{3+} and Pt^{2+} ions which entered the nucleus (and mitochondria), bound to DNA, and led to apoptosis of the HeLa cells. Taken together, the results of this study may serve as a useful guide for realizing new and powerful anticancer tools based on suitably conceived MSHs.

Significant efforts have been devoted to the development of inorganic nanostructures that could serve as platforms for photodynamic therapy (PDT) against tumors and pathogen bacteria under near-infrared light in the second biological window (NIR-II), where photon absorption and scattering in tissues are low (ideal for optical imaging), but photon energy is difficult to be harvested and utilized efficiently for generation of reactive oxygen species (ROSs).[112] In this context, Wang et al. made an important contribution, demonstrating the exploitation of rationally designed semiconductor-plasmonic MSHs, consisting of Ag-doped $CdSe_xS_y$-Au-$CdSe_xS_y$ nanodumbbells, as antibacterial PDT agents under NIR-II light.[66] The MSHs were designed so as to allow NIR-II photons to be utilized for the excitation of the LSPR of Au, to promote injection of as-generated hot electrons into the conduction band of the $CdSe_xS_y$ components at the extremities, and migration of the hot holes towards the exposed surfaces of the middle rod-like Au section. Redistribution of the NIR-photogenerated hot carriers to distinct regions of the nanoheterostructures allowed them to escape nonradiative recombination and to drive reduction and oxidation reactions to yield ROSs at spatially separated locations. Superoxide radicals were generated upon reduction of O_2 by the hot electrons at the $CdSe_xS_y$ domains, while hydroxyl radicals were produced upon oxidation of H_2O by the hot holes over the Au section (Figure 19h). In addition to the inherent advantages offered by the nanodumbbell architecture, the possibility of mastering the composition of the MSHs in the synthesis stage provided further benefits. The efficiency of hot-electron injection from the excited LSPR of Au to $CdSe_xS_y$ could be independently optimized by tuning the position of the lower conduction-band level of $CdSe_xS_y$ through adjustment of the Se to S ratio in the semiconductor (Figure 19i). Moreover, the presence of Ag impurities in the $CdSe_xS_y$ lattice at controllably low concentrations introduced empty energy levels into the forbidden gap, which could be populated by decaying hot electrons. As a consequence, undesired recombination would be further inhibited, thus prolonging the lifetime of the photogenerated hot carriers (Figure 19j). The favorable optoelectronic and photocatalytic properties allowed by the association of the unique structural and compositional features illustrated above explain why the $CdSe_xS_y$-Au-$CdSe_xS_y$ nanodumbbell MSHs exhibited significantly enhanced PDT capabilities under NIR-II light, compared to their Au@$CdSe_xS_y$ core–shell counterparts, as proven by in vitro and in vivo assessment of their antibacterial activity[66] (Figure 19k).

5. Summary and Prospects

Colloidal MSHs exemplify the essence of the heterostructuring paradigm aimed at realizing sophisticated breeds of programmable multifunctional inorganic nanostructures with richly tunable and even new properties, otherwise inaccessible to single-material NCs. Herein, advances in the seeded-growth synthesis of colloidal MSHs that leverage chemically driven transformative routes of metal-based seeds have been reviewed and critically discussed. Depending on the type of the starting seeds, their conversions may be performed by a combination of selective red-ox reactions and thermally or chemically induced (de)alloying processes. The advantages and drawbacks of exploiting replacement reactions to achieve sacrificial nucleation and growth of new materials domains over a pre-existing NC seed have been presented and discussed in a comparison with conventional seeding approaches. Thermodynamic and kinetic factors that play key roles in dictating the evolution of MSHs with a broad diversity of programmable architectures from their respective monometallic/bimetallic seeds have been identified and elaborated on the basis of the reported outcomes.

Overall, our survey of the achievements so far documented indicates that there is still much scope for the development of chemicalization-driven heterostructure formation routes to refined MSHs, for which a higher degree of architectural accuracy and structural perfection could be met by rational exploitation of mechanistic knowledge. From the practical viewpoint, the reproducibility with which these nanoheterostructures, hence their properties, can be synthesized beyond the laboratory mass production level is still quite limited, which motivates dedicated research efforts toward setting truly robust and easily scalable protocols. There are several unanswered questions, poorly addressed issues, and unmet challenges, as outlined below. Filling these gaps would lead to considerable improvements and advancement in the field.

Careful analysis of the literature accounts quoted here reveals that, in the vast majority of cases, the choice of given red-ox reactions for metal nanocrystal conversion to MSHs has been made with reference to the standard galvanic potential scale, where the considered solid phases are bulk monometals and alloys. Similarly, the possibility of exploiting (de)alloying pathways has preliminarily been evaluated on the basis of the relative stability order and allowed ranges of compositional variations known for the corresponding bulk phases under thermodynamic equilibrium. In the absence of such information, chemicalization protocols have likely been developed and optimized in a mere empirical manner. However, there have been experimental indications and theoretical confirmations that, in the nanoscale regime, the actual electropositivity of metal NCs may broadly deviate from that of their bulk counterparts, depending on their size, shape, the density, and distribution of excess electrostatic charge, and the presence of surface-bound ligands.[113–114] Experimental and calculated phase diagrams for nanoscale phases have revealed modified stability windows and anomalous miscibility behavior arising from the large surface/interface energy contribution to the overall energy of the system.[115] Internal lattice defects may also affect the propensity of the seeds to undergo structural and/or compositional transformations.[29,37,48,67–68,114] As a matter of fact, the ultimate behavior of metal seeds in oxidation and/or dealloying processes remains difficult to predict without some preliminary experimental hints. Because of these knowledge gaps, it is believed that the chemicalization approach to the construction of functional MSHs has so far been exploited far below its potential. In this respect, progress toward the achievement of higher synthetic versatility and accuracy would definitely require an understanding of the impact of a multitude of factors on the reactivity and evolution of the starting seeds on a deeper rational basis.

A systematic assessment of the dependence of the reactivity of the seeds on their compositional-geometric features and crystallographic structure is currently missing. Therefore, the first natural development direction of research on metal chemicalization routes to MSHs would be an investigation into the reactivity of NC seeds made of multimetallic and intermetallic alloys.[116] Although a significantly large number of MSHs have already been produced through the partial chemicalization of monometallic and bimetallic seed NCs, the exploitation of multimetallic and intermetallic alloy nanostructures remains largely unexplored.[67a] There exists a rich library of NCs of such materials with a broad range of structural diversity,[116] which could, in principle, be transformed to intriguing MSHs. In light of the unique crystallographic structures and compositional complexity of multimetallic and intermetallic alloys, knowledge of the possible conversion mechanisms would obviously be of extreme significance for advancing synthetic capabilities. It would be challenging to identify the thermodynamic and kinetic conditions under which each metal element could be selectively induced to participate in a transformative pathway to yield a desired semiconductor material. Dealloying processes are likely to proceed via the formation of alloy intermediates with distinct physical-chemical properties, thus making the study of their evolution intrinsically complicated. Controlled chemicalization of multimetallic and intermetallic NC seeds would hold great potential for the elaboration of elegant and concise synthesis routes to multimaterial MSHs.

Another mandatory development direction of research on metal chemicalization routes to MSHs would be to extend their application to a broader selection of shape-controlled metal NCs as seeds. A library of metal NCs with precisely controlled polyhedral-, rod-, polypod-, disk-, platelet-, and cage-like geometries has been constructed in the past decades.[114] Techniques are also available for transferring these nanocrystals into liquid media with different polarity and density, needed to meet requirements for specific chemicalization protocols. Shaped metal seeds with controlled geometric profiles represent ideal platforms for understanding the mechanisms that may underlie spatially anisotropic structural and chemical conversions across lattices characterized by preferred extension directions. Mastering the capability to manipulate the pathways through which the chemicalization front(s) may proceed in a transforming NC would allow for enriching the structural diversity and complexity of the accessible MSHs. The exotic constructs, which could be realized, would expose an asymmetric distribution of multiple semiconductor and metal modules with mixed dimensionalities, not otherwise achievable by the chemicalization of nearly spherical or regular polyhedral seeds.

A major issue in chemicalization routes, closely related to the aspects discussed above, concerns the poorly understood influence that lattice defects may have on the outcomes of partial chemicalization routes. Extended defects (such as twin planes, grain boundaries) certainly play some roles in governing the chemical accessibility of metal seeds,[29,37,48,67,68,114,166] but it is likely that also point defects play some roles. Thus, it remains unclear to what extent chemicalization approaches may be considered as convenient alternatives to classical seeded-growth approaches if transformations may be plagued by defects, especially if undetectable or irregularly distributed, as in the most frequent cases. However, partial chemicalization of accurately sorted seeds, characterized by refined crystallographic habit and ordered defects,[115] may be envisioned as a possible avenue to

MSHs with programmable architectural and compositional profiles.

The roles played by organic ligands during the chemicalization of metal NCs in a colloidal medium are known only marginally. During synthesis, the ligands obviously attach and detach dynamically to the solution-exposed surfaces of all components of growing nano(hetero)structures. It would thus be relevant to learn to what extent ligands and static charges accumulated on the solid surfaces allow or hinder the outflow of leaving cations and/or inflow of replacing or adding atomic species, or affect electron transfer reactions. In the presence of distinct ligands serving as both complexants for metal ions and capping agents for metal NCs, the galvanic potentials that feature metal-ion/ metal-NC red-ox couples involved in the synthesis could be unexpectedly modified, leading to seemingly anomalous reactivity behavior, as observed in some cases.[23,33,95b] Thus, further elaboration of the transformative approach to MSHs would require a more rational exploitation of ligand chemistry based on the ample library of molecules already available. For example, it would be extremely useful to identify ligands able to modulate or inhibit the redox attack of the chemicalization agent on specific site/regions of a seed. To this purpose, light shined on photodegradable or photopolymerizable ligands binding to the surface could be used to open or block chemical access to selected locations of the seeds. If viable, these mechanisms could pave the way to the synthesis of complex segmented or striped heterostructures, especially starting from anisotropic-shaped seeds. Also, there is a large family of ligands that could be introduced in chemicalization processes in order to controllably differentiate the reactivity of distinct metal species (for example, in an alloy seed) and/or the solvation of exiting metal ions, and/or to modulate the red-ox potentials of the reactants in the colloidal environment.[95b] Elaboration on this aspect could not only enable expanding the range of accessible materials, but also optimize the actual synthetic conditions, allowing for better control over the quality features of resulting MSHs.

The potential of chemicalization routes for delivering MSHs with semiconductor domains trapped in metastable phases, which can hardly be obtained otherwise, has already been disclosed to a certain extent. Such synthetic capabilities would be worthy to be investigated with due attention. Since new metastable materials are continuously being discovered, it may not be excluded that some poorly or fully unexplored semiconductor materials, possibly with novel and/or exotic properties, will be accessible via partial transformation of pre-existing metal NCs under selected reaction conditions.

An exciting research direction could involve the design of new chemicalization schemes relying on the application of additional means of triggering the partial transformation of metal seeds, alternative or complementary to conventional thermal activation. In the solution phase, chemicalization could be initiated or promoted by light irradiation. For example, photochemically activated or photodegradable reactants, which could release monomers upon light absorption, could be exploited for this purpose. Interestingly, red-ox reactions carried out under excitation of the LSPRs supported by plasmonic metal seeds, could be expected to benefit from some plasmon-driven enhancement effects.[5d,10s,108] Further, synthetic protocols could be modified by considering alternative means of delivering the necessary reactants into the liquid solution. For example, gaseous phase precursors and chemicalization agents (other than O_2) could be utilized. In addition, foreign "sacrificial" NCs could be exploited as a controllable source of the atomic elements necessary for implanting the desired semiconductor materials over preformed metal seeds. Finally, it would be worthy to explore chemicalization in nanoscale confined environments, such as those offered by micelles or the interface regions between immiscible liquids stabilized by surfactants, where the kinetics and thermodynamics of nucleation and growth of NCs may significantly deviate from those in bulk liquid media.[117]

The compositional and structural purity of the domains that nominally compose an MSH derived by a chemicalization route is also a matter of concern. Knowledge of all such subtle details appears to be a prerequisite to assessing their possible detrimental impact on the quality of the as-manifested physical-chemical properties, guaranteeing the correctness of their interpretation. Among issues that have yet to be addressed adequately, the chemical and crystallographic structures of the heterointerfaces between different adjoining lattices across MSHs remain undeciphered in the vast majority of cases due to inherent difficulties in their characterization by standard investigative techniques available to the majority of research groups. With the progress on experimental techniques, such as high-resolution TEM microscopy, X-ray photoelectron spectroscopy, X-ray and neutron scattering experiments, and their recent application to the investigation of *in-situ* grown nano(heterostructure), more in-depth atomic-level investigation of MSHs can be foreseen in the near future.

The rich physical-chemical properties and functional capabilities of chemicalization-derived MSHs, analogous to those of nanoheterostructures synthesized by other seeded-growth routes, depend sensitively not only on the structural, geometric, and compositional parameters of the individual component units, but also on proximity or electronic communication effects across the existing heterojunction with largely unknown structure. In many instances the search for multifunctionality conflicts with partial (often, inevitable) degradation of the expected properties of the otherwise isolated components due to changes in electronic structure uncontrollably introduced by impurities and/or defective heterointerfaces. As a further complication, it remains difficult to discriminate between mere proximity effects and the emergence of definitely unprecedented properties arising from electronic contact and exchange-coupling mechanisms. In this respect, theoretical studies, simulations, and modeling, which are still rather sparse, could lend support to current hypotheses on the verified structure-property relationships and/or contribute to formulate innovative models for interpreting experimental results. This feedback would indirectly inspire rational guiding criteria for advancing synthetic design. The preliminary demonstrations of the technological potential of MSHs in (photo)catalysis, energy storage, and biomedicine, which have been documented, promise to stimulate further conceptualization and practical developments in diverse fields of nanoscience.

Acknowledgements

SERB-India (CRG/2021/001783) is acknowledged for funding. S.B. acknowledges CSIR for fellowship.

Conflict of Interest

The authors declare no conflict of interest.

Keywords

colloidal metal-semiconductor heterostructures, energy conversion/storage, Kirkendall diffusion, metal seeds, partial chemicalization

Received: June 20, 2023
Revised: September 9, 2023
Published online:

[1] a) A. P. Alivisatos, *Science* **1996**, *271*, 933; b) C.-C. Chen, A. B. Herhold, C. S. Johnson, A. P. Alivisatos, *Science* **1997**, *276*, 398; c) U. Banin, *Nat. Mater.* **2007**, *6*, 625.

[2] a) T. Hisatomi, J. Kubota, K. Domen, *Chem. Soc. Rev.* **2014**, *43*, 7520; b) J. Q. Grim, L. Manna, I. Moreels, *Chem. Soc. Rev.* **2015**, *44*, 5897; c) Y. Chen, J. Vela, H. Htoon, J. L. Casson, D. J. Werder, D. A. Bussian, V. I. Klimov, J. A. Hollingsworth, *J. Am. Chem. Soc.* **2008**, *130*, 5026; d) X. Chen, S. Shen, L. Guo, S. S. Mao, *Chem. Rev.* **2010**, *110*, 6503; e) J. Kim, Y. Piao, T. Hyeon, *Chem. Soc. Rev.* **2009**, *38*, 372; f) K. E. Knowles, K. H. Hartstein, T. B. Kilburn, A. Marchioro, H. D. Nelson, P. J. Whitham, D. R. Gamelin, *Chem. Rev.* **2016**, *116*, 10820; g) X. Liu, M. T. Swihart, *Chem. Soc. Rev.* **2014**, *43*, 3908; h) D. V. Talapin, J.-S. Lee, M. V. Kovalenko, E. V. Shevchenko, *Chem. Rev.* **2009**, *110*, 389.

[3] C. Burda, X. Chen, R. Narayanan, M. A. El-Sayed, *Chem. Rev.* **2005**, *105*, 1025.

[4] a) C. Coughlan, M. Ibáñez, O. Dobrozhan, A. Singh, A. Cabot, K. M. Ryan, *Chem. Rev.* **2017**, *117*, 5865; b) D. Kang, T. W. Kim, S. R. Kubota, A. C. Cardiel, H. G. Cha, K.-S. Choi, *Chem. Rev.* **2015**, *115*, 12839; c) A. Comin, L. Manna, *Chem. Soc. Rev.* **2014**, *43*, 3957; d) J. Ran, J. Zhang, J. Yu, M. Jaroniec, S. Z. Qiao, *Chem. Soc. Rev.* **2014**, *43*, 7787; e) P. Losch, W. Huang, E. D. Goodman, C. J. Wrasman, A. Holm, A. R. Riscoe, J. A. Schwalbe, M. Cargnello, *Nano Today* **2019**, *24*, 15.

[5] a) R. W. Murray, *Chem. Rev.* **2008**, *108*, 2688; b) S. Eustis, M. A. El-Sayed, *Chem. Soc. Rev.* **2006**, *35*, 209; c) J. Fang, B. Ding, H. Gleiter, *Chem. Soc. Rev.* **2011**, *40*, 5347; d) C. Wang, D. Astruc, *Chem. Soc. Rev.* **2014**, *43*, 7188; e) M.-C. Daniel, D. Astruc, *Chem. Rev.* **2004**, *104*, 293; f) P. V. Kamat, *J. Phys. Chem. B* **2002**, *106*, 7729; g) J. D. Hoefelmeyer, K. Niesz, G. A. Somorjai, T. D. Tilley, *Nano Lett.* **2005**, *5*, 435; h) N. R. Jana, T. Pal, *Adv. Wet-Chem. Synth. Approaches Inorg. Nanostruct.* **2008**, 185.

[6] a) P. D. Cozzoli, T. Pellegrino, L. Manna, *Chem. Soc. Rev.* **2006**, *35*, 1195; b) S. K. Dutta, S. K. Mehetor, N. Pradhan, *J. Phys. Chem. Lett.* **2015**, *6*, 936.

[7] a) A. P. Alivisatos, *NATO Sci. Ser., Ser. C* **1999**, *519*, 405; b) J. R. Chelikowsky, *Phys. Novel Mater., Proc. Phys. Summer Sch.* **1999**, 1; c) J. R. Chelikowsky, *Appl. Phys.* **2005**, *307*.

[8] K. L. Kelly, E. Coronado, L. L. Zhao, G. C. Schatz, *J. Phys. Chem. B* **2003**, *107*, 668.

[9] a) U. Banin, Y. Ben-Shahar, K. Vinokurov, *Chem. Mater.* **2014**, *26*, 97; b) J. Liu, J. Zhang, *Chem. Rev.* **2020**, *120*, 2123; c) Y. Ben-Shahar, D. Stone, U. Banin, *Chem. Rev.* **2023**, *123*, 3790; d) L. Carbone, P. D. Cozzoli, *Nano Today* **2010**, *5*, 449; e) C. Nobile, P. D. Cozzoli, *Nanomater* **2022**, *12*, 1729; f) D. de Mello, *Chem. Soc. Rev.* **2011**, *40*, 1512.

[10] a) A. Dutta, S. K. Dutta, S. K. Mehetor, I. Mondal, U. Pal, N. Pradhan, *Chem. Mater.* **2016**, 1872; b) A. Dutta, K. Samantara Aneeya, D. Adhikari Samrat, K. Jena Bikash, N. Pradhan, *J. Phys. Chem. Lett.* **2016**; c) S. Chakrabortty, G. Xing, Y. Xu, S. W. Ngiam, N. Mishra, T. C. Sum, Y. Chan, *Small* **2011**, *7*, 2847; d) K. K. Haldar, N. Pradhan, A. Patra, *Small* **2013**, *9*, 3424; e) T. Mokari, C. G. Sztrum, A. Salant, E. Rabani, U. Banin, *Nat. Mater.* **2005**, *4*, 855; f) B. K. Patra, S. Khilari, D. Pradhan, N. Pradhan, *Chem. Mater.* **2016**, *28*, 4358; g) A. Figuerola, M. V. Huis, M. Zanella, A. Genovese, S. Marras, A. Falqui, H. W. Zandbergen, R. Cingolani, L. Manna, *Nano Lett.* **2010**, *10*, 3028; h) I. R. Franchini, G. Bertoni, A. Falqui, C. Giannini, L. W. Wang, L. Manna, *J. Mater. Chem.* **2010**, *20*, 1357; i) C.-H. Kuo, T.-E. Hua, M. H. Huang, *J. Am. Chem. Soc.* **2009**, *131*, 17871; j) B. K. Patra, S. Khilari, A. Bera, S. K. Mehetor, D. Pradhan, N. Pradhan, *Chem. Mater.* **2017**, *29*, 1116; k) X. Yu, X. An, A. Genç, M. Ibáñez, J. Arbiol, Y. Zhang, A. Cabot, *J. Phys. Chem. C* **2015**, 21882; l) R. Costi, G. Cohen, A. Salant, E. Rabani, U. Banin, *Nano Lett.* **2009**, *9*, 2031; m) S. L. Cumberland, M. G. Berrettini, A. Javier, G. F. Strouse, *Chem. Mater.* **2003**, *15*, 1047; n) B. K. Patra, A. K. Guria, A. Dutta, A. Shit, N. Pradhan, *Chem. Mater.* **2014**, *26*, 7194; o) A. Dutta, S. Mutyala, A. K. Samantara, S. Bera, B. K. Jena, N. Pradhan, *ACS Energy Lett.* **2018**, *3*, 141; p) L. Amirav, F. Oba, S. Aloni, A. P. Alivisatos, *Angew. Chem., Int. Ed.* **2015**, *54*, 7007; q) P. D. Cozzoli, L. Manna, *Nat. Mater.* **2005**, *4*, 801; r) G. Manna, R. Bose, N. Pradhan, *Angew. Chem., Int. Ed.* **2014**, *53*, 6743; s) R. Jiang, B. Li, C. Fang, J. Wang, *Adv. Mater.* **2014**, *26*, 5274; t) X. Yu, A. Shavel, X. An, Z. Luo, M. Ibáñez, A. Cabot, *J. Am. Chem. Soc.* **2014**, *136*, 9236.

[11] a) R. Costi, A. E. Saunders, E. Elmalem, A. Salant, U. Banin, *Nano Lett.* **2008**, *8*, 637; b) Y. Ben-Shahar, F. Scotognella, I. Kriegel, L. Moretti, G. Cerullo, E. Rabani, U. Banin, *Nat. Commun.* **2016**, *7*, 10413; c) Y. Ben-Shahar, U. Banin, *Top. Curr. Chem.* **2016**, *374*, 54; d) T. O'connor, M. S. Panov, A. Mereshchenko, A. N. Tarnovsky, R. Lorek, D. Perera, G. Diederich, S. Lambright, P. Moroz, M. Zamkov, *ACS Nano* **2012**, *6*, 8156; e) P. Moroz, A. Boddy, M. Zamkov, *Front. Chem.* **2018**, *6*; f) N. Razgoniaeva, P. Moroz, S. Lambright, M. Zamkov, *J. Phys. Chem. Lett.* **2015**, *6*, 4352; g) S. Rawalekar, T. Mokari, *Adv. Energy Mater.* **2013**, 3, 12; h) M. R. Kim, Z. Xu, G. Chen, D. Ma, *Chem. Euro. J.* **2014**, *20*, 11256.

[12] a) R. Lavieville, Y. Zhang, A. Casu, A. Genovese, L. Manna, E. Di Fabrizio, R. Krahne, *ACS Nano* **2012**, *6*, 2940; b) M. Zanella, G. Bertoni, I. R. Franchini, R. Brescia, D. Baranov, L. Manna, *Chem. Commun.* **2011**, *47*, 203; c) K.-Y. Jiang, Y.-L. Weng, S.-Y. Guo, Y. Yu, F.-X. Xiao, *Nanoscale* **2017**, *9*, 16922.

[13] a) M. Casavola, V. Grillo, E. Carlino, C. Giannini, F. Gozzo, E. Fernandez Pinel, M. A. Garcia, L. Manna, R. Cingolani, P. D. Cozzoli, *Nano Lett.* **2007**, *7*, 1386; b) J. W. Ha, T. P. A. Ruberu, R. Han, B. Dong, J. Vela, N. Fang, *J. Am. Chem. Soc.* **2014**, *136*, 1398.

[14] a) A. Figuerola, A. Fiore, R. Di Corato, A. Falqui, C. Giannini, E. Micotti, A. Lascialfari, M. Corti, R. Cingolani, T. Pellegrino, P. D. Cozzoli, L. Manna, *J. Am. Chem. Soc.* **2008**, *130*, 1477; b) S. E. Habas, H. Lee, V. Radmilovic, G. A. Somorjai, P. Yang, *Nat. Mater.* **2007**, *6*, 692; c) R. Scarfiello, C. Nobile, P. D. Cozzoli, *Front. Mater.* **2016**, *3*; d) R. Bose, A. H. M. A. Wasey, G. P. Das, N. Pradhan, *J. Phys. Chem. Lett.* **2014**, *5*, 1892; e) B. K. Patra, A. Shit, A. K. Guria, S. Sarkar, G. Prusty, N. Pradhan, *Chem. Mater.* **2015**, *27*, 2650; f) Y. Xia, K. D. Gilroy, H.-C. Peng, X. Xia, *Angew. Chem., Int. Ed.* **2017**, *56*, 60; g) S. Bera, N. Pradhan, *ACS Energy Lett.* **2020**, *5*, 2858.

[15] M. Casavola, R. Buonsanti, G. Caputo, P. D. Cozzoli, *Euro. J. Inorg. Chem.* **2008**, *2008*, 837.

[16] a) S. Sen, S. Bera, N. Pradhan, *Chem. Mater.* **2022**, *34*, 9329; b) S. Sen, R. Jana, S. Bera, S. Shyamal, P. Sahu, A. Datta, N. Pradhan, *J. Phys. Chem. Lett.* **2022**, *13*, 3804; c) S. Bera, A. Roy, A. K. Guria, S. Mitra, N. Pradhan, *J. Phys. Chem. Lett.* **2019**, *10*, 1024; d) S. Sen, S. Bera, A. K. Guria, N. Pradhan, *J. Phys. Chem. C* **2021**, *125*, 1923; e) R. Buonsanti, V. Grillo, E. Carlino, C. Giannini, F. Gozzo, M. Garcia-Hernandez, M. A. Garcia, R. Cingolani, P. D. Cozzoli, *J. Am. Chem. Soc.* **2010**, *132*, 2437; f) C. George, D. Dorfs, G. Bertoni, A. Falqui, A. Genovese, T. Pellegrino, A. Roig, A. Quarta, R. Comparelli, M. L. Curri, R. Cingolani, L. Manna, *J. Am. Chem. Soc.* **2011**, *133*, 2205;

g) X. Liu, C. Lee, W.-C. Law, D. Zhu, M. Liu, M. Jeon, J. Kim, P. N. Prasad, C. Kim, M. T. Swihart, *Nano Lett.* **2013**, *13*, 4333; h) X. Tang, K. Yu, Q. Xu, E. S. G. Choo, G. K. L. Goh, J. Xue, *J. Mater. Chem.* **2011**, *21*, 11239; i) P. S. Dilsaver, M. D. Reichert, B. L. Hallmark, M. J. Thompson, J. Vela, *J. Phys. Chem. C* **2014**, *118*, 21226; j) X. Hong, Z. Yin, Z. Fan, Y.-Y. Tay, J. Chen, Y. Du, C. Xue, H. Chen, H. Zhang, *Small* **2014**, *10*, 479; k) D. Lin, H. Wu, R. Zhang, W. Pan, *Chem. Mater.* **2009**, *21*, 3479; l) P. Sahu, G. Prusty, A. K. Guria, N. Pradhan, *Small* **2018**, *14*, 1801598.

[17] a) R. S. Geonmonond, A. G. M. D. Silva, P. H. C. Camargo, *Anais da Academia Brasileira de Ciências* **2018**, *90*; b) A. Gole, C. J. Murphy, *Chem. Mater.* **2004**, *16*, 3633; c) N. R. Jana, L. Gearheart, C. J. Murphy, *Adv. Mater.* **2001**, *13*, 1389; d) M. V. Kovalenko, D. V. Talapin, M. A. Loi, F. Cordella, G. Hesser, M. I. Bodnarchuk, W. Heiss, *Angew. Chem., Int. Ed.* **2008**, *47*, 3029; e) N. Pradhan, N. R. Jana, K. Mallick, T. Pal, *J. Surf. Sci. Technol.* **2000**, *16*, 188; f) R. Xie, M. Zhou, *Chem. Mater.* **2015**, *27*, 3055.

[18] L. Carbone, S. Kudera, C. Giannini, G. Ciccarella, R. Cingolani, P. D. Cozzoli, L. Manna, *J. Mater. Chem.* **2006**, *16*, 3952.

[19] a) W. Wang, M. Dahl, Y. Yin, *Chem. Mater.* **2013**, *25*, 1179; b) B. D. Anderson, J. B. Tracy, *Nanoscale* **2014**, *6*, 12195.

[20] Y. Yin, R. M. Rioux, C. K. Erdonmez, S. Hughes, G. A. Somorjai, A. P. Alivisatos, *Science* **2004**, *304*, 711.

[21] a) Y. Yin, C. K. Erdonmez, A. Cabot, S. Hughes, A. P. Alivisatos, *Adv. Funct. Mater.* **2006**, *16*, 1389; b) T.-J. Yoon, H. Shao, R. Weissleder, H. Lee, *Part. Part. Syst. Charact.* **2013**, *30*, 667; c) L. Mu, F. Wang, B. Sadtler, R. A. Loomis, W. E. Buhro, *ACS Nano* **2015**, *9*, 7419; d) J. G. Railsback, A. C. Johnston-Peck, J. Wang, J. B. Tracy, *ACS Nano* **2010**, *4*, 1913; e) M. Saha, S. Ghosh, S. K. De, *Catal. Today* **2020**, *340*, 253; f) M. Li, H. Shang, H. Li, Y. Hong, C. Ling, K. Wei, B. Zhou, C. Mao, Z. Ai, L. Zhang, *Angew. Chem., Int. Ed.* **2021**, *60*, 17115; g) D. Ji, L. Fan, L. Tao, Y. Sun, M. Li, G. Yang, T. Q. Tran, S. Ramakrishna, S. Guo, *Angew. Chem., Int. Ed.* **2019**, *58*, 13840; h) A. Shapiro, Y. Jang, F. Horani, Y. Kauffmann, E. Lifshitz, *Chem. Mater.* **2018**, *30*, 3141.

[22] A. Cabot, V. F. Puntes, E. Shevchenko, Y. Yin, L. Balcells, M. A. Marcus, S. M. Hughes, A. P. Alivisatos, *J. Am. Chem. Soc.* **2007**, *129*, 10358.

[23] L.-I. Hung, C.-K. Tsung, W. Huang, P. Yang, *Adv. Mater.* **2010**, *22*, 1910.

[24] R. Nakamura, J.-G. Lee, H. Mori, H. Nakajima, *Philos. Mag.* **2008**, *88*, 257.

[25] J. S. Cho, H. S. Ju, Y. C. Kang, *Sci. Rep.* **2016**, *6*, 23915.

[26] K. Kravchyk, L. Protesescu, M. I. Bodnarchuk, F. Krumeich, M. Yarema, M. Walter, C. Guntlin, M. V. Kovalenko, *J. Am. Chem. Soc.* **2013**, *135*, 4199.

[27] Y. Son, Y. Son, M. Choi, M. Ko, S. Chae, N. Park, J. Cho, *Nano Lett.* **2015**, *15*, 6914.

[28] R. Nakamura, D. Tokozakura, H. Nakajima, J.-G. Lee, H. Mori, *J. Appl. Phys.* **2007**, *101*, 074303.

[29] K.-Y. Niu, J. Park, H. Zheng, A. P. Alivisatos, *Nano Lett.* **2013**, *13*, 5715.

[30] L. Yu, Z. Yan, Z. Cai, D. Zhang, P. Han, X. Cheng, Y. Sun, *Nano Lett.* **2016**, *16*, 6555.

[31] Y. Ren, W. K. Chim, S. Y. Chiam, J. Q. Huang, C. Pi, J. S. Pan, *Adv. Funct. Mater.* **2010**, *20*, 3336.

[32] A.-A. E. Mel, P.-Y. Tessier, M. Buffiere, E. Gautron, J. Ding, K. Du, C.-H. Choi, S. Konstantinidis, R. Snyders, C. Bittencourt, L. Molina-Luna, *Small* **2016**, *12*, 2885.

[33] N. Doan, K. Kontturi, C. Johans, *J. Colloid Interface Sci.* **2010**, *350*, 126.

[34] R. Nakamura, J.-G. Lee, D. Tokozakura, H. Mori, H. Nakajima, *Mater. Lett.* **2007**, *61*, 1060.

[35] C. M. Wang, D. R. Baer, L. E. Thomas, J. E. Amonette, J. Antony, Y. Qiang, G. Duscher, *J. Appl. Phys.* **2005**, *98*, 094308.

[36] R. Sainju, D. Rathnayake, H. Tan, G. Bollas, A. M. Dongare, S. L. Suib, Y. Zhu, *ACS Nano* **2022**, *16*, 6468.

[37] Z. Yang, N. Yang, J. Yang, J. Bergström, M.-P. Pileni, *Adv. Funct. Mater.* **2015**, *25*, 891.

[38] Z. Yang, I. Lisiecki, M. Walls, M.-P. Pileni, *ACS Nano* **2013**, *7*, 1342.

[39] A.-A. El Mel, N. Stephant, L. Molina-Luna, E. Gautron, Y. Haik, N. Tabet, P.-Y. Tessier, R. Gautier, *J. Phys. Chem. C* **2017**, *121*, 19497.

[40] A.-A. El Mel, M. Buffière, P.-Y. Tessier, S. Konstantinidis, W. Xu, K. Du, I. Wathuthanthri, C.-H. Choi, C. Bittencourt, R. Snyders, *Small* **2013**, *9*, 2838.

[41] A. Cabot, R. K. Smith, Y. Yin, H. Zheng, B. M. Reinhard, H. Liu, A. P. Alivisatos, *ACS Nano* **2008**, *2*, 1452.

[42] A. Cabot, M. Ibáñez, P. Guardia, A. P. Alivisatos, *J. Am. Chem. Soc.* **2009**, *131*, 11326.

[43] M. Ibáñez, J. Fan, W. Li, D. Cadavid, R. Nafria, A. Carrete, A. Cabot, *Chem. Mater.* **2011**, *23*, 3095.

[44] B. Liu, Z. Ma, *Small* **2011**, *7*, 1587.

[45] M. M. Shahjamali, Y. Zhou, N. Zaraee, C. Xue, J. Wu, N. Large, C. M. Mcguirk, F. Boey, V. Dravid, Z. Cui, G. C. Schatz, C. A. Mirkin, *ACS Nano* **2016**, *10*, 5362.

[46] Y. Liu, A. R. Hight Walker, *J. Phys. Chem. C* **2010**, *114*, 4264.

[47] J. Gao, B. Zhang, X. Zhang, B. Xu, *Angew. Chem., Int. Ed.* **2006**, *45*, 1220.

[48] Y. Tang, M. Ouyang, *Nat. Mater.* **2007**, *6*, 754.

[49] A. K. Guria, G. Prusty, B. K. Patra, N. Pradhan, *J. Am. Chem. Soc.* **2015**, *137*, 5123.

[50] L. De Trizio, A. Figuerola, L. Manna, A. Genovese, C. George, R. Brescia, Z. Saghi, R. Simonutti, M. Van Huis, A. Falqui, *ACS Nano* **2012**, *6*, 32.

[51] S. Peng, S. Sun, *Angew. Chem., Int. Ed.* **2007**, *46*, 4155.

[52] D. Albinsson, S. Nilsson, T. J. Antosiewicz, V. P. Zhdanov, C. Langhammer, *J. Phys. Chem. C* **2019**, *123*, 6284.

[53] N. Cabrera, N. F. Mott, *Rep. Prog. Phys.* **1949**, *12*, 163.

[54] G. Xiao, Y. Zeng, Y. Jiang, J. Ning, W. Zheng, B. Liu, X. Chen, G. Zou, B. Zou, *Small* **2013**, *9*, 793.

[55] X. Wang, J. Feng, Y. Bai, Q. Zhang, Y. Yin, *Chem. Rev.* **2016**, *116*, 10983.

[56] E. V. Shevchenko, M. I. Bodnarchuk, M. V. Kovalenko, D. V. Talapin, R. K. Smith, S. Aloni, W. Heiss, A. P. Alivisatos, *Adv. Mater.* **2008**, *20*, 4323.

[57] B. Y. Kim, I.-B. Shim, Z. O. Araci, S. S. Saavedra, O. L. A. Monti, N. R. Armstrong, R. Sahoo, D. N. Srivastava, J. Pyun, *J. Am. Chem. Soc.* **2010**, *132*, 3234.

[58] Q. Zhao, M. Ji, H. Qian, B. Dai, L. Weng, J. Gui, J. Zhang, M. Ouyang, H. Zhu, *Adv. Mater.* **2014**, *26*, 1387.

[59] M. Liu, P. Guyot-Sionnest, *J. Mater. Chem.* **2006**, *16*, 3942.

[60] X.-L. Liu, S. Liang, F. Nan, Y.-Y. Pan, J.-J. Shi, L. Zhou, S.-F. Jia, J.-B. Wang, X.-F. Yu, Q.-Q. Wang, *Opt. Express* **2013**, *21*, 24793.

[61] H. Wang, Y. Gao, J. Liu, X. Li, M. Ji, E. Zhang, X. Cheng, M. Xu, J. Liu, H. Rong, W. Chen, F. Fan, C. Li, J. Zhang, *Adv. Energy Mater.* **2019**, *9*, 1803889.

[62] J. Zhu, Y. Shen, A. Xie, L. Zhu, *J. Mater. Chem.* **2009**, *19*, 8871.

[63] X. Li, R. E. Schaak, *Chem. Mater.* **2017**, *29*, 4153.

[64] J. Zhang, Y. Tang, K. Lee, M. Ouyang, *Science* **2010**, *327*, 1634.

[65] L. Weng, H. Zhang, A. O. Govorov, M. Ouyang, *Nat. Commun.* **2014**, *5*, 4792.

[66] D. Wang, H. Wang, L. Ji, M. Xu, B. Bai, X. Wan, D. Hou, Z.-Y. Qiao, H. Wang, J. Zhang, *ACS Nano* **2021**, *15*, 8694.

[67] a) H. Liu, F. Ye, H. Cao, J. Ji, J. Y. Lee, J. Yang, *Nanoscale* **2013**, *5*, 6901; b) P. Cui, H. He, H. Liu, S. Zhang, J. Yang, *J. Power Sources* **2016**, *327*, 432; c) Y. Feng, H. Liu, P. Wang, F. Ye, Q. Tan, J. Yang, *Sci. Rep.* **2014**, *4*, 6204.

[68] H. Liu, J. Qu, Y. Chen, J. Li, F. Ye, J. Y. Lee, J. Yang, *J. Am. Chem. Soc.* **2012**, *134*, 11602.

[69] M. Li, X.-F. Yu, S. Liang, X.-N. Peng, Z.-J. Yang, Y.-L. Wang, Q.-Q. Wang, *Adv. Funct. Mater.* **2011**, *21*, 1788.
[70] T. R. Gordon, R. E. Schaak, *Chem. Mater.* **2014**, *26*, 5900.
[71] D. Chen, H. Liu, P. Cui, C. Li, F. Ye, J. Yang, *CrystEngComm* **2015**, *17*, 6155.
[72] A.-M. Nguyen, M. Bahri, S. Dreyfuss, S. Moldovan, A. Miche, C. Méthivier, O. Ersen, N. Mézailles, S. Carenco, *Chem. Mater.* **2019**, *31*, 6124.
[73] Z. Fan, X. Zhang, J. Yang, X.-J. Wu, Z. Liu, W. Huang, H. Zhang, *J. Am. Chem. Soc.* **2015**, *137*, 10910.
[74] P. Guardia, K. Korobchevskaya, A. Casu, A. Genovese, L. Manna, A. Comin, *ACS Nano* **2013**, *7*, 1045.
[75] N. E. Motl, J. F. Bondi, R. E. Schaak, *Chem. Mater.* **2012**, *24*, 1552.
[76] E. A. Lewis, T. J. A. Slater, E. Prestat, A. Macedo, P. O'brien, P. H. C. Camargo, S. J. Haigh, *Nanoscale* **2014**, *6*, 13598.
[77] X. Ding, Y. Zou, J. Jiang, *J. Mater. Chem.* **2012**, *22*, 23169.
[78] M. Sun, Z. Wang, H. Wang, *Chem. Mater.* **2022**, *34*, 1965.
[79] X. Ding, Y. Zou, F. Ye, J. Yang, J. Jiang, *J. Mater. Chem. A* **2013**, *1*, 11880.
[80] B. Shen, L. Huang, J. Shen, X. Hu, P. Zhong, C. Y. Zheng, C. Wolverton, C. A. Mirkin, *ACS Nano* **2023**, *17*, 4642.
[81] W. Lu, B. Wang, J. Zeng, X. Wang, S. Zhang, J. G. Hou, *Langmuir* **2005**, *21*, 3684.
[82] L. Han, Q. Meng, D. Wang, Y. Zhu, J. Wang, X. Du, E. A. Stach, H. L. Xin, *Nat. Commun.* **2016**, *7*, 13335.
[83] K. Koga, D. Zubia, *J. Phys. Chem. C* **2008**, *112*, 2079.
[84] Q. Zhang, J.-J. Wang, Z. Jiang, Y.-G. Guo, L.-J. Wan, Z. Xie, L. Zheng, *J. Mater. Chem.* **2012**, *22*, 1765.
[85] L. Xu, Z. Yin, S.-W. Cao, Z. Fan, X. Zhang, H. Zhang, C. Xue, *Chem. Euro. J.* **2014**, *20*, 2742.
[86] W. Xia, Y. Yang, Q. Meng, Z. Deng, M. Gong, J. Wang, D. Wang, Y. Zhu, L. Sun, F. Xu, J. Li, H. L. Xin, *ACS Nano* **2018**, *12*, 7866.
[87] S. F. Tan, S. W. Chee, Z. Baraissov, H. Jin, T. L. Tan, U. Mirsaidov, *Adv. Funct. Mater.* **2019**, *29*, 1903242.
[88] D. Thiry, L. Molina-Luna, E. Gautron, N. Stephant, A. Chauvin, K. Du, J. Ding, C.-H. Choi, P.-Y. Tessier, A.-A. El Mel, *Chem. Mater.* **2015**, *27*, 6374.
[89] W. Zhan, J. Wang, H. Wang, J. Zhang, X. Liu, P. Zhang, M. Chi, Y. Guo, Y. Guo, G. Lu, S. Sun, S. Dai, H. Zhu, *J. Am. Chem. Soc.* **2017**, *139*, 8846.
[90] E. A. Sutter, X. Tong, K. Jungjohann, P. W. Sutter, *Proc. Natl. Acad. Sci.* **2013**, *110*, 10519.
[91] L. Shi, L. Shangguan, S. Yang, Y. Zhou, B. Wang, J. Xie, Y. Yang, L. He, X. Liao, L. Sun, *ACS Appl. Nano Mater.* **2022**, *5*, 14400.
[92] H. Zhang, G. Liu, J. Li, H. Cui, Y. Liu, M. Wang, *J. Mater. Sci.* **2021**, *56*, 4328.
[93] Y. Yang, L. Liu, F. Güder, A. Berger, R. Scholz, O. Albrecht, M. Zacharias, *Angew. Chem., Int. Ed.* **2011**, *50*, 10855.
[94] P. Y. Keng, M. M. Bull, I.-B. Shim, K. G. Nebesny, N. R. Armstrong, Y. Sung, K. Char, J. Pyun, *Chem. Mater.* **2011**, *23*, 1120.
[95] a) S. Duan, R. Wang, *NPG Asia Mater* **2014**, *6*, e122. b) L. Bai, Y. Kuang, J. Luo, D. G. Evans, X. Sun, *Chem. Commun.* **2012**, *48*, 6983.
[96] M. S. Seifner, M. Snellman, O. A. Makgae, K. Kumar, D. Jacobsson, M. Ek, K. Deppert, M. E. Messing, K. A. Dick, *J. Am. Chem. Soc.* **2022**, *144*, 248.
[97] G. Jiang, Y. Huang, S. Zhang, H. Zhu, Z. Wu, S. Sun, *Nanoscale* **2016**, *8*, 17947.
[98] E. A. Hernández-Pagán, R. W. Lord, J. M. Veglak, R. E. Schaak, *Inorg. Chem.* **2021**, *60*, 4278.
[99] A. Li, W. Zhu, C. Li, T. Wang, J. Gong, *Chem. Soc. Rev.* **2019**, *48*, 1874.
[100] J. Gao, G. Liang, B. Zhang, Y. Kuang, X. Zhang, B. Xu, *J. Am. Chem. Soc.* **2007**, *129*, 1428.
[101] H. Yu, M. Chen, P. M. Rice, S. X. Wang, R. L. White, S. Sun, *Nano Lett.* **2005**, *5*, 379.
[102] S. Lambright, E. Butaeva, N. Razgoniaeva, T. Hopkins, B. Smith, D. Perera, J. Corbin, E. Khon, R. Thomas, P. Moroz, A. Mereshchenko, A. Tarnovsky, M. Zamkov, *ACS Nano* **2013**, *8*, 352.
[103] W. Sang, T. Zheng, Y. Wang, X. Li, X. Zhao, J. Zeng, J. G. Hou, *Nano Lett.* **2014**, *14*, 6666.
[104] a) A. Sitt, I. Hadar, U. Banin, *Nano Today* **2013**, *8*, 494; b) R. Costi, A. E. Saunders, U. Banin, *Angew. Chem., Int. Ed.* **2010**, *49*, 4878.
[105] a) N. E. Motl, A. F. Smith, C. J. Desantis, S. E. Skrabalak, *Chem. Soc. Rev.* **2014**, *43*, 3823; b) G. Baffou, R. Quidant, *Phys. Rep.* **2017**, *674*, 1.
[106] a) H. Tong, S. Ouyang, Y. Bi, N. Umezawa, M. Oshikiri, J. Ye, *Adv. Mater.* **2012**, *24*, 229; b) L. Buzzetti, G. E. M. Crisenza, P. Melchiorre, *Angew. Chem., Int. Ed.* **2019**, *58*, 3730; c) G. Palmisano, E. García-López, G. Marcì, V. Loddo, S. Yurdakal, V. Augugliaro, L. Palmisano, *Chem. Commun.* **2010**, *46*, 7074; d) M. Marszewski, S. Cao, J. Yu, M. Jaroniec, *Mater. Horiz* **2015**, *2*, 261.
[107] a) N. M. Dimitrijevic, T. Rajh, S. P. Ahrenkiel, J. M. Nedeljkovic, O. I. Micic, A. J. Nozik, *J. Phys. Chem. B* **2005**, *109*, 18243; b) S. G. Louie, J. R. Chelikowsky, M. L. Cohen, *Phys. Rev. B* **1977**, *15*, 2154.
[108] a) W. Hou, S. B. Cronin, *Adv. Funct. Mater.* **2013**, *23*, 1612; b) X. Zhang, Y. L. Chen, R.-S. Liu, D. P. Tsai, *Rep. Prog. Phys.* **2013**, *76*, 046401; c) X. Meng, L. Liu, S. Ouyang, H. Xu, D. Wang, N. Zhao, J. Ye, *Adv. Mater.* **2016**, *28*, 6781; d) A. O. Govorov, H. Zhang, H. V. Demir, Y. K. Gun'ko, *Nano Today* **2014**, *9*, 85.
[109] a) F. Zaera, *ChemSusChem* **2013**, *6*, 1797; b) M. Muzzio, J. Li, Z. Yin, I. M. Delahunty, J. Xie, S. Sun, *Nanoscale* **2019**, *11*, 18946; c) P. Sonström, M. Bäumer, *Phys. Chem. Chem. Phys.* **2011**, *13*, 19270.
[110] a) F. Liao, B. T. W. Lo, E. Tsang, *Euro. J. Inorg. Chem.* **2016**, *2016*, 1924; b) L. L. Chng, N. Erathodiyil, J. Y. Ying, *Acc. Chem. Res.* **2013**, *46*, 1825; c) M. Si, F. Lin, H. Ni, S. Wang, Y. Lu, X. Meng, *RSC Adv.* **2023**, *13*, 2140; d) C. Xie, Z. Niu, D. Kim, M. Li, P. Yang, *Chem. Rev.* **2020**, *120*, 1184.
[111] a) M. F. Oszajca, M. I. Bodnarchuk, M. V. Kovalenko, *Chem. Mater.* **2014**, *26*, 5422; b) Y.-X. Yin, S. Xin, Y.-G. Guo, L.-J. Wan, *Angew. Chem., Int. Ed.* **2013**, *52*, 13186; c) Q. Wang, C. Zhao, Y. Lu, Y. Li, Y. Zheng, Y. Qi, X. Rong, L. Jiang, X. Qi, Y. Shao, D. Pan, B. Li, Y.-S. Hu, L. Chen, *Small* **2017**, *13*, 1701835; d) D. H. S. Tan, A. Banerjee, Z. Chen, Y. S. Meng, *Nat. Nanotechnol.* **2020**, *15*, 170; e) X. Liu, J.-Q. Huang, Q. Zhang, L. Mai, *Adv. Mater.* **2017**, *29*, 1601759; f) L. P. Wang, L. Yu, X. Wang, M. Srinivasan, Z. J. Xu, *J. Mater. Chem. A* **2015**, *3*, 9353.
[112] a) W. J. Parak, D. Gerion, T. Pellegrino, D. Zanchet, C. Micheel, S. C. Williams, R. Boudreau, M. A. L. Gros, C. A. Larabell, A. P. Alivisatos, *Nanotechnol* **2003**, *14*, R15; b) A. Quarta, R. Di Corato, L. Manna, A. Ragusa, T. Pellegrino, *IEEE Trans. NanoBiosci.* **2007**, *6*, 298; c) N. C. Bigall, W. J. Parak, D. Dorfs, *Nano Today* **2012**, *7*, 282; d) A. Quarta, C. Piccirillo, G. Mandriota, R. Di Corato, *Mater* **2019**, *12*, 139.
[113] a) M. D. Scanlon, P. Peljo, M. A. Méndez, E. Smirnov, H. H. Girault, *Chem. Sci.* **2015**, *6*, 2705; b) A. M. Schimpf, K. E. Knowles, G. M. Carroll, D. R. Gamelin, *Acc. Chem. Res.* **2015**, *48*, 1929.
[114] a) Y. Xia, Y. Xiong, B. Lim, S. E. Skrabalak, *Angew. Chem., Int. Ed.* **2009**, *48*, 60; b) B. Lim, Y. Xia, *Angew. Chem., Int. Ed.* **2011**, *50*, 76; c) H. Zhang, M. Jin, Y. Xia, *Angew. Chem., Int. Ed.* **2012**, *51*, 7656; d) W. Niu, G. Xu, *Nano Today* **2012**, *7*, 586; e) Q. Zhang, S. Cao, J. Wang, *Nano Today* **2011**, *6*, 265;
[115] a) T. L. Hill, *Nano Lett.* **2001**, *1*, 273; b) S. Carenco, D. Portehault, C. Boissière, N. Mézailles, C. Sanchez, *Adv. Mater.* **2014**, *26*, 371.
[116] a) J. W. M. Crawley, I. E. Gow, N. Lawes, I. Kowalec, L. Kabalan, C. R. A. Catlow, A. J. Logsdail, S. H. Taylor, N. F. Dummer, G. J. Hutchings, *Chem. Rev.* **2022**, *122*, 6795; b) Y. Yan, J. S. Du, K. D. Gilroy, D. Yang, Y. Xia, H. Zhang, *Adv. Mater.* **2017**, *29*, 1605997; c) M. Zhou, C. Li, J. Fang, *Chem. Rev.* **2021**, *121*, 736.
[117] a) X. Wang, Q. Peng, Y. Li, *Acc. Chem. Res.* **2007**, *40*, 635; b) Q. Jiang, M. D. Ward, *Chem. Soc. Rev.* **2014**, *43*, 2066; c) R. Tong, D. Zhang, X. Feng, *Chem. Rev.* **2018**, *118*, 6189.

Suman Bera earned his MSc degree in chemistry from the Indian Institute of Technology, Madras, India, in 2014, and his BSc from University of Kolkata, India, in 2012. He obtained his PhD from the Indian Association for the Cultivation of Sciences (IACS), Kolkata, India, in 2020. He is currently working as a postdoctoral fellow (CSIR-RA) in the School of Materials Sciences at IACS, India, in the research group led by Prof. Narayan Pradhan. His research interests are the synthesis of colloidal semiconducting nanocrystals, investigations of their optical and photophysical properties, and their exploration in various applications.

Puspanjali Sahu received her MSc degree from Utkal University, India, and her PhD from CSIR-National Chemical Laboratory, Pune, India. Then, she worked as a post-doctoral researcher at the Indian Association for the Cultivation of Sciences, India; at the Korea Advanced Institute of Science and Technology, Korea; and at the CSIR-Institute of Minerals and Materials Technology, India. Currently, she works as an assistant professor in the Department of Chemistry & Teacher Education at Bhadrak Autonomous College, Odisha, India. Her research interests concern the size and shape tunable synthesis of nanomaterials, their assembly into different architectures, and their photo- and electrochemical applications, with a focus on the development of flexible transparent materials.

Anirban Dutta is currently working as a Scientist at Indian Oil R&D, Indian Oil Corporation Limited. He received his Bachelor's degree in chemistry from Suri Vidyasagar College, The University of Burdwan, and Master's from the Indian Institute of Technology, Delhi. He has completed his Ph.D. from the Indian Association for the Cultivation of Science under the supervision of Prof. Narayan Pradhan on metal phosphide nanomaterial for photo and electrocatalysis. Later, Dr. Dutta worked on the growth mechanism and optoelectronic properties of lead halide perovskite nanocrystals. His current research focuses on perovskite solar cells, self-cleaning anti-soiling coating for solar panels, and electrolyzer development for alkaline and anion exchange membrane electrolysis.

Concetta Nobile received her M.Sc. degree in physics in 2003 from the University of Bari, Italy, and her Ph.D. in 2008 from the University of Salento, Lecce, Italy. Her Ph.D. research activities focused on the self-assembly of colloidal nanostructures for applications in optoelectronic devices. In 2009–2011, she was a post-doctoral fellow at the National Nanotechnology Laboratory, National Research Council (CNR), Italy. In 2011–2015, she worked at CNR Institute Nanoscience, Lecce, Italy. She currently holds a position as a senior researcher at the CNR Institute of Nanotechnology, Lecce, Italy. Her research activity is devoted to the structural characterization of functional inorganic nanomaterials of relevance for photovoltaics and biomedicine, by means of advanced electron microscopy techniques.

Narayan Pradhan obtained his Ph.D. from the Indian Institute of Technology, Kharagpur, India, in 2001. He carried out his postdoctoral research activities at Ben-Gurion University, Israel and at the University of Arkansas, USA. Currently, he works as Professor in the School of Materials Sciences, Indian Association for the Cultivation of Sciences (IACS), Kolkata, India. His major research interests encompass the synthesis, study of their photophysical properties, and application of colloidal semiconductor nanocrystals.

P. Davide Cozzoli received his M.Sc. degree in chemistry in 1999 and his Ph.D. in 2004 from the University of Bari, Italy. His Ph.D. activities were partially carried out at the University of Hamburg, Germany. In 2004–2005, he continued his research as a post-doctoral fellow at the University of Bari. In 2005–2007, he joined as a junior researcher at the National Nanotechnology Laboratory, National Research Council (CNR), Lecce, Italy. In 2007–2015, he worked as a permanent staff researcher at the University of Salento, Lecce, Italy. In 2007–2019, he served as a research associate at the CNR Institute Nanoscience and at the CNR Institute of Nanotechnology, Lecce, Italy. Since 2015, he has been an associate professor of experimental matter physics at the University of Salento, Lecce, Italy. His research interests include the design, synthesis, and physical-chemical characterization of colloidal inorganic nano(hetero)structures for innovative processes and applications.